OAK RIDGE
NATIONAL LABORATORY
MANAGED BY UT-BATTELLE
FOR THE DEPARTMENT OF ENERGY

ORNL/TM-2007/14

Development of PIMAL: Mathematical Phantom with Moving Arms and Legs

May 2007

Prepared by
Hatice Akkurt
Keith F. Eckerman

UT-BATTELLE
ORNL-27 (4-00)

DOCUMENT AVAILABILITY

Reports produced after January 1, 1996, are generally available free via the U.S. Department of Energy (DOE) Information Bridge.

Web site http://www.osti.gov/bridge

Reports produced before January 1, 1996, may be purchased by members of the public from the following source.

National Technical Information Service
5285 Port Royal Road
Springfield, VA 22161
Telephone 703-605-6000 (1-800-553-6847)
TDD 703-487-4639
Fax 703-605-6900
E-mail info@ntis.gov
Web site http://www.ntis.gov/support/ordernowabout.htm

Reports are available to DOE employees, DOE contractors, Energy Technology Data Exchange (ETDE) representatives, and International Nuclear Information System (INIS) representatives from the following source.

Office of Scientific and Technical Information
P.O. Box 62
Oak Ridge, TN 37831
Telephone 865-576-8401
Fax 865-576-5728
E-mail reports@osti.gov
Web site http://www.osti.gov/contact.html

This report was prepared as an account of work sponsored by an agency of the United States Government. Neither the United States Government nor any agency thereof, nor any of their employees, makes any warranty, express or implied, or assumes any legal liability or responsibility for the accuracy, completeness, or usefulness of any information, apparatus, product, or process disclosed, or represents that its use would not infringe privately owned rights. Reference herein to any specific commercial product, process, or service by trade name, trademark, manufacturer, or otherwise, does not necessarily constitute or imply its endorsement, recommendation, or favoring by the United States Government or any agency thereof. The views and opinions of authors expressed herein do not necessarily state or reflect those of the United States Government or any agency thereof.

ORNL/TM-2007/14

Nuclear Science and Technology Division (094)
and
Environmental Sciences Division (042)

DEVELOPMENT OF PIMAL: MATHEMATICAL PHANTOM WITH MOVING ARMS AND LEGS

Hatice Akkurt
Keith F. Eckerman

Date Published: May 2007

Prepared by
OAK RIDGE NATIONAL LABORATORY
Oak Ridge, Tennessee 37831-6283
managed by
UT-BATTELLE, LLC
for the
U.S. DEPARTMENT OF ENERGY
under contract DE-AC05-00OR22725

CONTENTS

Page

LIST OF FIGURES v

LIST OF TABLES xi

ACKNOWLEDGMENTS xiii

ABSTRACT xv

1. INTRODUCTION 1

2. COMPARISON OF THE MIRD-5 AND ORNL-UF PHANTOM MODELS 3
   2.1 COMPOSITION OF THE MAJOR ORGANS 7

3. BENCHMARK COMPUTATIONS 9
   3.1 SOURCE GEOMETRIES 9
   3.2 BACKGROUND ON CONVERSION COEFFICIENTS REPORTED IN ICRP-74 11
   3.3 MCNP COMPUTATIONS 13
      3.3.1 Benchmark Calculation Results for Photon Source 13
      3.3.2 Benchmark Calculation Results for Neutron Source 23
      3.3.3 Comparison of the Computed Organ Dose Values Using the ORNL-UF and MIRD-5 Phantom Models for Photon Source 29
      3.3.4 Comparison of the Computed Organ Dose Values Using the ORNL-UF and MIRD-5 Phantom Models for Neutron Source 31
   3.4 SUMMARY OF THE BENCHMARK CALCULATIONS 33

4. SENSITIVITY ANALYSIS 35
   4.1 SENSITIVITY TO COMPOSITION 35
      4.1.1 Sensitivity to Composition for Photon Source 35
      4.1.2 Sensitivity to Composition for Neutron Source 38
   4.2 SENSITIVITY TO CROSS SECTIONS 41
   4.3 SUMMARY OF THE SENSITIVITY CALCULATIONS 44

5. PIMAL: PHANTOM WITH MOVING ARMS AND LEGS 45
   5.1 DESCRIPTION OF PIMAL 45
   5.2 BENCHMARK COMPUTATIONS 49

6. GRAPHICAL USER INTERFACE FOR PIMAL 51
   6.1 DESCRIPTION OF THE GUI 51
      6.1.1 GUI Layout and Moving Arms and Legs 51
      6.1.2 Snap Image 52
      6.1.3 Generate MCNP Input 53
      6.1.4 Load Custom Input and Substitute Energy 54
      6.1.5 MCNP Outputs and Executable Name 55
      6.1.6 Organ Dose Values 56

CONTENTS (CONTINUED)

Page

7. SUMMARY AND FUTURE WORK 59

8. REFERENCES 63

LIST OF FIGURES

Figure **Page**

1. The exterior shape of the MIRD-5 and ORNL-UF phantom models. 4

2. The exterior shape of the MIRD-5 and ORNL-UF phantom models. 4

3. Interior shape of the MIRD-5 and the ORNL-UF phantom models 5

4. The shape of the internal organs, front and back after removing the ribs. 6

5. Antero-posterior (AP) irradiation geometry. 10

6. Postero-anterior (PA) irradiation geometry. 10

7. Right lateral (RLAT) irradiation geometry. 10

8. Left lateral (LLAT) irradiation geometry. 10

9. Isotropic (ISO) irradiation geometry. 11

10. Evaluated and original data for the mean absorbed dose to the liver in PA geometry. 12

11. Evaluated and original data for the mean absorbed dose to the thyroid in PA geometry. 12

12. Evaluated and original data for the mean absorbed dose to the colon in LLAT geometry. 12

13. Evaluated and original data for the mean absorbed dose to the colon in RLAT geometry. 12

14. The absorbed dose per air kerma for the ORNL-UF model and ICRP-74 values to the gonads 14

15. The absorbed dose per air kerma for the ORNL-UF model and ICRP-74 values to the breast 14

16. The absorbed dose per air kerma for MIRD-5 phantom model and ICRP-74 values to the breast 15

17. The ratios of the computed organ dose values for the ORNL-UF model using 23 compositions vs. 3 compositions for the description of tissues for breast 15

18. The absorbed dose per air kerma for the ORNL-UF model and ICRP-74 values to the esophagus 16

19. The absorbed dose per air kerma for the ORNL-UF model and ICRP-74 values to the thyroid. 17

LIST OF FIGURES (CONTINUED)

Figure **Page**

20. The absorbed dose per air kerma for the MIRD-5 phantom model and ICRP-74 values to the thyroid 17

21. The ratio of the computed absorbed dose values to the thyroid using the MIRD-5 and ORNL-UF phantom models. 18

22. The ratio of the thyroid dose for the ORNL-UF phantom model with 23 compositions vs. 3 compositions. 18

23. The front, side, and top view of the location of the thyroid in the ORNL-UF phantom model. 19

24. The front, side, and top view of the location of the thyroid in the MIRD-5 phantom model. 19

25. The absorbed dose per air kerma for the ORNL-UF model and ICRP-74 values to the colon 20

26. The absorbed dose per kerma for the ORNL-UF model and ICRP-74 values to the liver 20

27. The absorbed dose per air kerma for the ORNL-UF model and ICRP-74 values to the lungs. 21

28. The absorbed dose per air kerma for the ORNL-UF model and ICRP-74 values to the stomach. 21

29. The absorbed dose per air kerma for the ORNL-UF model and ICRP-74 values to the bladder 22

30. Gonad absorbed dose per unit neutron fluence for the ORNL-UF model and ICRP-74 values. 23

31. Breast absorbed dose per unit neutron fluence for the ORNL-UF model and ICRP-74 values 24

32. Esophagus absorbed dose per unit neutron fluence for the ORNL-UF model and ICRP-74 values. 25

33. Thyroid absorbed dose per unit neutron fluence for the ORNL-UF model and ICRP-74 values. 25

34. Colon absorbed dose per unit neutron fluence for the ORNL-UF model and ICRP-74 values. 26

LIST OF FIGURES (CONTINUED)

Figure **Page**

35. Liver absorbed dose per unit neutron fluence for the ORNL-UF model and ICRP-74 values. 26

36. Lung absorbed dose per unit neutron fluence for the ORNL-UF model and ICRP-74 values. 27

37. Stomach absorbed dose per unit neutron fluence for the ORNL-UF model and ICRP-74 values 27

38. Bladder absorbed dose per unit neutron fluence for the ORNL-UF model and ICRP-74 values. 28

39. The ratio of the computed organ dose values to the gonads and bone surface using the ORNL-UF and MIRD-5 phantom models. 29

40. The ratio of the computed organ dose values to the liver and lungs using the ORNL-UF and MIRD-5 phantom models. 30

41. The ratio of the computed organ dose values to the stomach and colon using the ORNL-UF and MIRD-5 phantom models. 30

42. The ratio of the computed organ dose values to the gonads and breast using the ORNL-UF and MIRD-5 phantom models. 31

43. The ratio of the computed organ dose values to the bone surface and colon using the ORNL-UF and MIRD-5 phantom models. 31

44. The ratio of the computed organ dose values to the liver and lungs using the ORNL-UF and MIRD-5 phantom models. 32

45. The ratio of the computed organ dose values to the thyroid and stomach using the ORNL-UF and MIRD-5 phantom models. 32

46. The ratio of the computed organ doses using 23 and 3 compositions for gonads and bladder . 35

47. The ratio of the computed organ doses using 23 and 3 compositions for liver and colon . 36

48. The ratio of the computed organ doses using 23 and 3 compositions for stomach and bone surface . 36

49. The ratio of the computed organ doses using 23 and 3 compositions for esophagus and thyroid . 37

LIST OF FIGURES (CONTINUED)

Figure **Page**

50. The ratio of the computed organ doses using 23 and 3 compositions for lungs and skin 37

51. The ratio of the computed organ doses using 23 and 3 compositions for breast. 38

52. The ratio of the total, neutron, and photon computed organ doses using 23 and 3 compositions for gonads. 39

53. The ratio of the neutron and photon dose to the total (neutron and photon) dose for gonads. 39

54. The ratio of the total, neutron, and photon computed organ doses using 23 and 3 compositions for breast. 40

55. The ratio of the neutron and photon dose to the total (neutron and photon) dose for breast. 40

56. The ratio of the computed organ dose values using ENDF/B-V, ENDF/B-VI.0, and ENDF/B-VI.6 nuclear data sets for gonads and colon 41

57. The ratio of the computed organ dose values using ENDF/B-V, ENDF/B-VI.0, and ENDF/B-VI.6 nuclear data sets for thyroid and esophagus 42

58. The ratio of the computed organ dose values using ENDF/B-V, ENDF/B-VI.0, and ENDF/B-VI.6 nuclear data sets for liver and stomach 43

59. The ratio of the computed organ dose values using ENDF/B-V, ENDF/B-VI.0, and ENDF/B-VI.6 nuclear data sets for bladder and bone surface 43

60. The ORNL-UF phantom model in the vertical-upright position with arms attached to torso and rigid legs and PIMAL-phantom with moving arms and legs 46

61. Interior shape, after skin and soft tissue are removed, of the ORNL-UF and PIMAL models. 47

62. The phantom is walking with one of the arms in the front and sitting on a chair with the arms on armrest. 48

63. The ratio of the computed organ doses using ORNL-UF and PIMAL models for gonads and breast 49

64. The ratio of the computed organ doses using the ORNL-UF and PIMAL models for lungs and thyroid 50

65. The layout of the GUI for PIMAL. 52

LIST OF FIGURES (CONTINUED)

Figure **Page**

66. The image of the phantom generated with "Snap Image" button of the GUI and the generated figure for this configuration using MORITZ 53

67. The MCNP Input file window. 54

68. The layout of the GUI when a custom input file is used. The option for entering source parameters using the GUI will be inactive when the "Substitute Energy" box is not checked. 55

69. The "View Screen MCNP Output" and "View MCNP Output" buttons will display the screen messages while running the code and the full MCNP output, respectively..... 56

70. The layout of the organ dose display. 57

LIST OF TABLES

Table **Page**

1. The elemental composition and density for the MIRD-5 phantom model 7

2. Elemental composition of the major organs for the ORNL-UF phantom model..... 8

ACKNOWLEDGMENTS

This work was supported by the Office of Nuclear Regulatory Research, U.S. Nuclear Regulatory Commission (NRC), under Project Y6460, Task 7 of Development of Radiation Protection Databases.

The authors would like to thank Eun Young Han and Wesley Bolch, University of Florida, for sharing the product of their work, an MCNP input file for the adult phantom model, which was used as a starting point in this work.

Special thanks go to Dorothea Wiarda (Nuclear Science and Technology Division, Oak Ridge National Laboratory) for diligently developing and improving the GUI for PIMAL. Dorothea not only carried out this task but also made many suggestions leading to a much-improved tool.

The authors would also like to thank Aaron Fleckenstein for developing the initial version of the GUI and Bradley Rearden for pointing out the simple model upon which the 3D visualization was developed.

The technical reviews and comments provided by John Wagner and Thomas Miller are very much appreciated. The authors would also like to thank Deborah Weaver and Missy Sherrod for the careful editing of this report.

ABSTRACT

The computational model of the human anatomy (phantom) has gone through many revisions since its initial development in the 1970s. The computational phantom model currently used by the Nuclear Regulatory Commission (NRC) is based on a model published in 1974. Hence, the phantom model used by the NRC staff was missing some organs (e.g., neck, esophagus) and tissues. Further, locations of some organs were inappropriate (e.g., thyroid). Moreover, all the computational phantoms were assumed to be in the vertical-upright position. However, many occupational radiation exposures occur with the worker in other positions. In the first phase of this work, updates on the computational phantom models were reviewed and a revised phantom model, which includes the updates for the relevant organs and compositions, was identified. This revised model was adopted as the starting point for this development work, and hence a series of radiation transport computations, using the Monte Carlo code MCNP5, was performed. The computational results were compared against values reported by the International Commission on Radiation Protection (ICRP) in Publication 74. For some of the organs (e.g., thyroid), there were discrepancies between the computed values and the results reported in ICRP-74. The reasons behind these discrepancies have been investigated and are discussed in this report. Additionally, sensitivity computations were performed to determine the sensitivity of the organ doses for certain parameters, including composition and cross sections used in the simulations. To assess the dose for more realistic exposure configurations, the phantom model was revised to enable flexible positioning of the arms and legs. Furthermore, to reduce the user time for analyses, a graphical user interface (GUI) was developed. The GUI can be used to visualize the positioning of the arms and legs as desired posture is achieved to generate the input file, invoke the computations, and extract the organ dose values from the MCNP5 output file. In this report, the main features of the phantom model with moving arms and legs and user interface are described.

1. INTRODUCTION

In the early computational models, the human anatomy was represented with cylinders and spheres of homogeneous composition. The depth-dose relationships obtained from these simple models were used extensively to derive the operational quantities for radiation protection for external radiation fields.

The first heterogeneous model was developed[1] at Oak Ridge National Laboratory (ORNL) for Medical Internal Radiation Dose (MIRD) in the 1970s using the anatomical data of the "Reference Man" publication of the International Commission on Radiological Protection (ICRP)—a European or North American adult male of 1.7 m tall, weighing 70 kg, and 20 to 30 years of age.[2] In order to reduce the computational time in Monte Carlo simulations of the radiation transport, the organs were modeled using simple mathematical equations. The body was defined with elliptical cylinders (i.e., head, torso, and arms) and legs as truncated elliptical cones. The model, often referred to as the MIRD, ORNL, mathematical, or stylized phantom, was initially developed for calculating doses from internal radiation. Later it was widely used to assess the organ doses for exposure to external radiation fields as well. In this model, three material compositions were specified in describing the organs: lung, bone, and soft tissue. Although the original phantom was an adult hermaphrodite model, with both male and female gender-specific organs for both genders, later developments[3] at ORNL led to a series of age-specific models and pregnant female models at different stages of pregnancy. Other institutes developed gender-specific adult models, known as ADAM and EVA,[4] largely based on the original ORNL model.

Over the past two decades, these mathematical (or stylized) computational phantoms have been the "standard" for dose assessment for internal and external exposures to radiation. In addition to many other organizations, the Nuclear Regulatory Commission (NRC) has used the phantom for dose assessment purposes as well. The phantom model currently used by the NRC is the MIRD-5 phantom, published in 1974. Therefore, from this point forward, the phantom model currently used by the NRC staff will be referred to as the MIRD-5 phantom. This phantom has a rigid structure and does not include some of the organs and tissues now considered important in the assessment of radiation exposures. Furthermore, all computational phantoms, with few exceptions, assume that the phantom is in the vertical-upright position, which is often not the case for occupational exposures. Therefore, one of the objectives of this work was to update the MIRD-5 mathematical phantom model, currently used by the NRC staff to improve the assessment of dose for realistic exposure configurations.

The study started with a review phase, where the developments in the phantom models over the past two decades were reviewed to determine the necessary modifications to the MIRD-5 phantom. For this purpose, documents related to the subject, including several existing Monte Carlo N-Particle (MCNP) input data files and models generated by BodyBuilder,[5] were collected and reviewed. For all the models, except one, three compositions (lung, soft tissue, and skeleton) are used. The exterior shapes of the models were rigid, the arms were part of the torso, and the legs were rigid. As the University of Florida (UF), under the direction of Wesley Bolch and in conjunction with Keith Eckerman, recently updated the ORNL phantom model,[6] an MCNP input file representing that effort was made available. This update included detailed representation of the tissues of the head and other organs of interest in the dosimetry of radiopharmaceuticals.[7] Many tissues, which were not separately represented in the earlier ORNL/MIRD phantoms, are included in this updated model. In addition, the tissue compositions (23 different compositions) based on the data of ICRP Publication 89 (Ref. 8) have been updated in the model. The adult phantom is a hermaphrodite; i.e., includes both male and female gender-specific organs. Although the internal organs are presented in greater detail, the exterior shape of the body is still rigid (i.e., arms included within the torso and legs remained rigid and joined). The recently revised phantom by UF in conjunction with ORNL is referred to herein as the ORNL-UF phantom model.

Differences between the MIRD-5 and the ORNL-UF phantom models were analyzed. A series of Monte Carlo computations, using both the MIRD-5 and ORNL-UF models, for the standard ICRP exposure geometries in neutron and photon radiation fields were performed. The results were benchmarked against the values reported in ICRP Publication 74 (Ref. 9). Calculations with the MIRD-5 phantom were also performed to determine the impact of any changes. When discrepancies were found between the computed values and the values reported in ICRP-74 for some of the organs (e.g., thyroid), the reasons behind these discrepancies were investigated. Additional calculations were performed to determine the sensitivity of the computed organ dose values to the material composition, cross sections, and organ locations.

With a few exceptions, all the previous computational models assumed the phantom to be in the standard vertical-upright position. For example, the model was revised for evaluating the organ doses for the A-bomb survivors where a sitting position was considered.[10] Similarly, in evaluating the doses for a worker sitting in a chair, the leg model was revised; however, the arms were still part of the torso.[11] In simulations of the Japan Nuclear Fuel Conversion Co. (JCO) criticality accident, the arms and legs of the two workers were separated and located in an appropriate position.[12] To our knowledge, in these works, the phantom was revised specifically for the case in hand—that is, no model was formulated with the capability to freely position the arms and legs.

To develop a computational phantom with freely moving arms and legs, the MCNP input file for the ORNL-UF phantom model was modified to separate the arms from the torso and to define the upper and lower arm regions, which are joined at the elbow. Similarly, the legs were divided and reshaped into lower and upper regions that are joined at the knee. The upper arm and upper leg regions are connected to the torso at the shoulder and hip, respectively. The arms can bend at the shoulder and elbow; legs at the hip and knee. A series of benchmark calculations, for a subset of the previous computations, was performed to ensure the modifications did not result in statistically significant changes in the computed organ dose values when the arms and legs are in the upright rigid position.

The second objective of this study was to develop an interface to assist the user (or analyst) in using the updated phantom model in dose assessment activities. This interface was especially needed to facilitate positioning of the arms and legs and then to generate the MCNP input file for the desired posture. For this purpose, a graphical user interface (GUI) has been developed. The GUI is operating system independent, since the coding was done in Java. A phantom model was included in the GUI, thus enabling visualization of the arms and legs as positioned using slider bars. Once the user decides on the posture, an MCNP input file can be generated and the radiation transport simulations using MCNP can be performed through the GUI. Furthermore, the computed organ dose values can be extracted (from the MCNP output file), displayed, and exported as an ASCII file.

Hence, the culmination of this work is a detailed mathematical phantom model with freely moving arms and legs to enable the analyses of realistic exposure configurations and an accompanying GUI to facilitate phantom postures and dose assessment analyses.

The organization of this report is as follows: Section 2 highlights the differences between the MIRD-5 and ORNL-UF phantom models. Section 3 presents the results for the benchmark calculations. Section 4 discusses the sensitivity computations. Section 5 discusses the modifications to the phantom for adding moving abilities and computational results for the modified phantom. Section 6 describes the main features of the graphical user interface. Section 7 presents the summary and recommendations for future work.

2. COMPARISON OF THE MIRD-5 AND ORNL-UF PHANTOM MODELS

As discussed in the previous section, one of the main objectives of this project is to update the mathematical phantom currently used by the NRC to improve dose assessment capabilities. The NRC staff currently uses the MIRD-5 phantom model, published in 1974 (Ref. 1). This model has a rigid structure and does not include some organs and tissues now considered important to the assessment of radiation exposures.

The updates and the revisions to the mathematical phantom models were reviewed to determine the necessary changes to be addressed in updating the current phantom. Several phantom models, including models the phantom model currently used by the NRC staff, MIRD-5, and models within the Body Builder software were collected and examined. A recently revised mathematical phantom model was identified and obtained from the UF. The ORNL-UF model includes detailed representation of the tissues of the head and other organs of interest for internal dosimetry of radiopharmaceuticals.[6,7] Many tissues, which were not separately represented in the previous ORNL/MIRD models, are included in the ORNL-UF model. In addition, 23 different tissue compositions based on the data of ICRP Publication 89 (Ref. 8) have been incorporated in the model. The model is a hermaphrodite. Although the internal organs have been revised in detail, the exterior shape of the body is rigid (i.e., the arms are attached to the torso and the legs are rigid).

In this section, the differences between the MIRD-5 and ORNL-UF phantom models are presented. The front and side view for the exterior shapes of the MIRD-5 and the ORNL-UF phantom models are shown in Fig. 1 and Fig. 2, respectively. As seen from these figures, the main difference in the exterior shape of these two models is the addition of the neck in the ORNL-UF phantom model. Furthermore, as shown in the side view, the head shape has been revised and a nose has been added. Both phantom models are hermaphrodite. The phantom is 176 cm tall and weighs 73 kg corresponding to the reference values of ICRP Publication 89 (Ref. 8). For both models, the arms are attached to the torso and the leg shapes are the same.

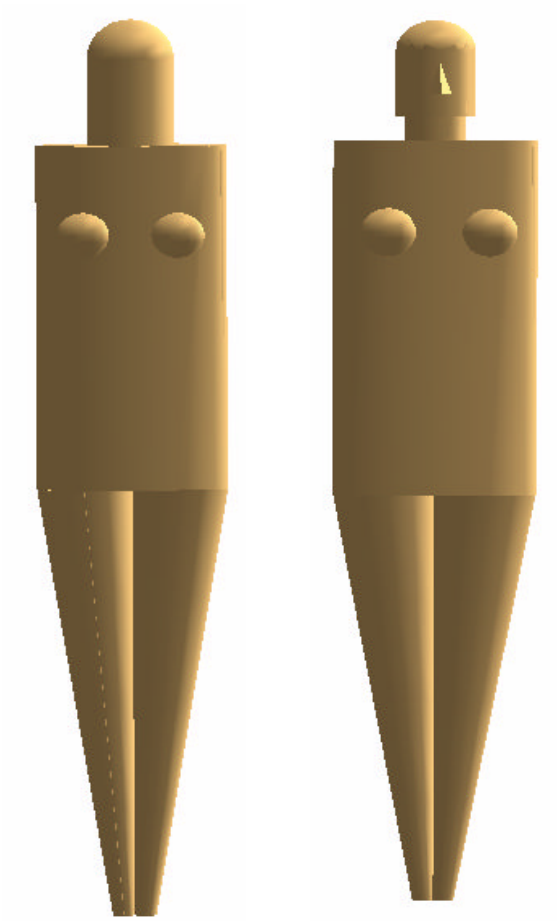

Fig. 1. The exterior (front) shape of the MIRD-5 (left) and ORNL-UF (right) phantom models.

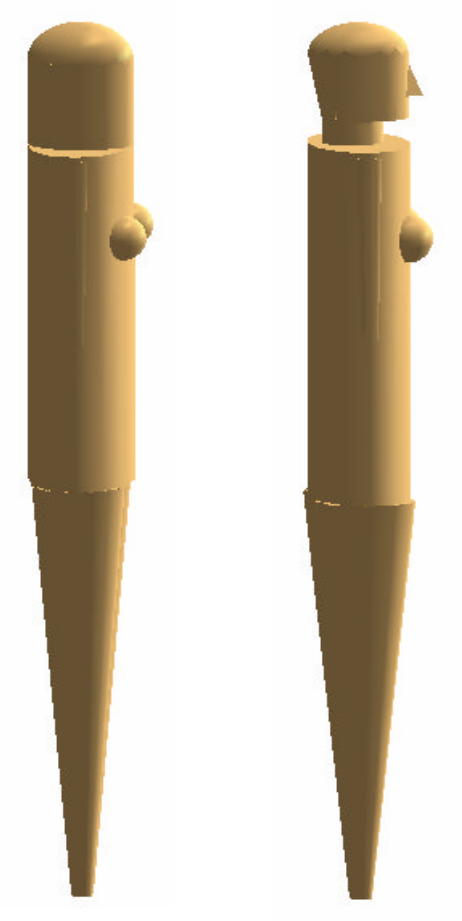

Fig. 2. The exterior (side) shape of the MIRD-5 (left) and ORNL-UF (right) phantom models.

The skeleton and internal organs of the MIRD-5 (left) and ORNL-UF (right) phantoms without skin and surrounding soft tissue are shown in Fig. 3. In this figure, the coloring for internal organs is done according to the material numbers. For the MIRD-5 phantom, there are three materials: lung, bone, and soft tissue. Soft tissue was used to describe the elemental composition for all the internal organs except the lung. For the ORNL-UF phantom model, there are 23 compositions, corresponding to each internal organ. As can be seen from the figure, in addition to the number of materials, the differences in the head and airway are evident. For the MIRD-5 phantom model, the head was modeled as a simple elliptical cylinder. In the ORNL-UF model the head is divided into parts (ellipse and cylinders), the eye models have been revised, and sinuses and esophagus have been added. Although the internal organs have been revised in detail, the rib shape remains the same in the ORNL-UF model.

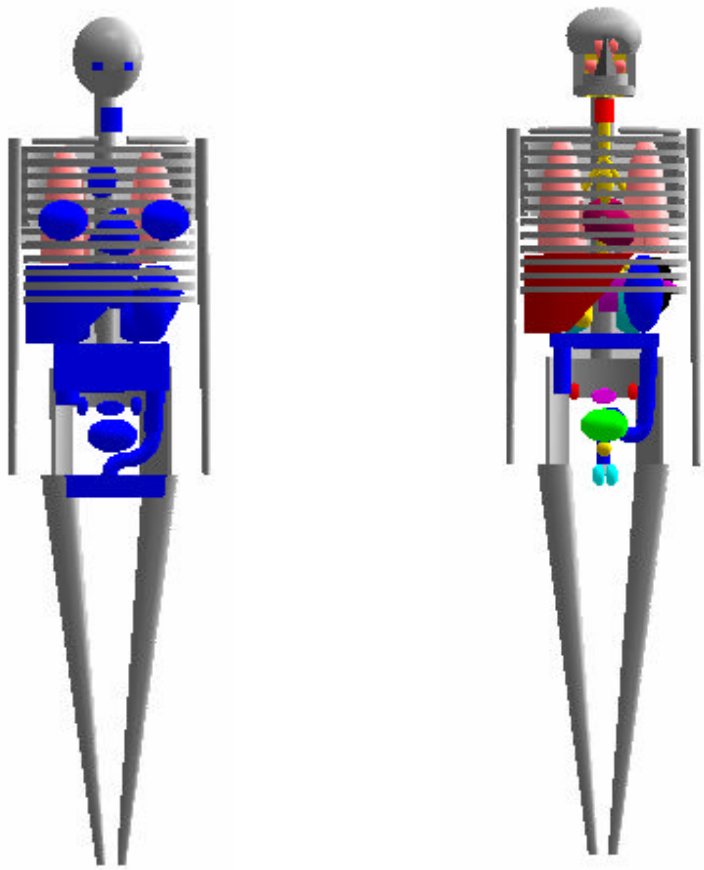

Fig. 3. Interior shape of the MIRD-5 (left) and the ORNL-UF phantom models (right).

The front and back views of the ORNL-UF phantom's internal organs are shown in Fig. 4. In this figure, the organs are shown in more detail with the ribs removed. In the ORNL-UF phantom model, left and right organs (e.g., lungs) were treated differently although they were considered identical in the MIRD-5 phantom model.

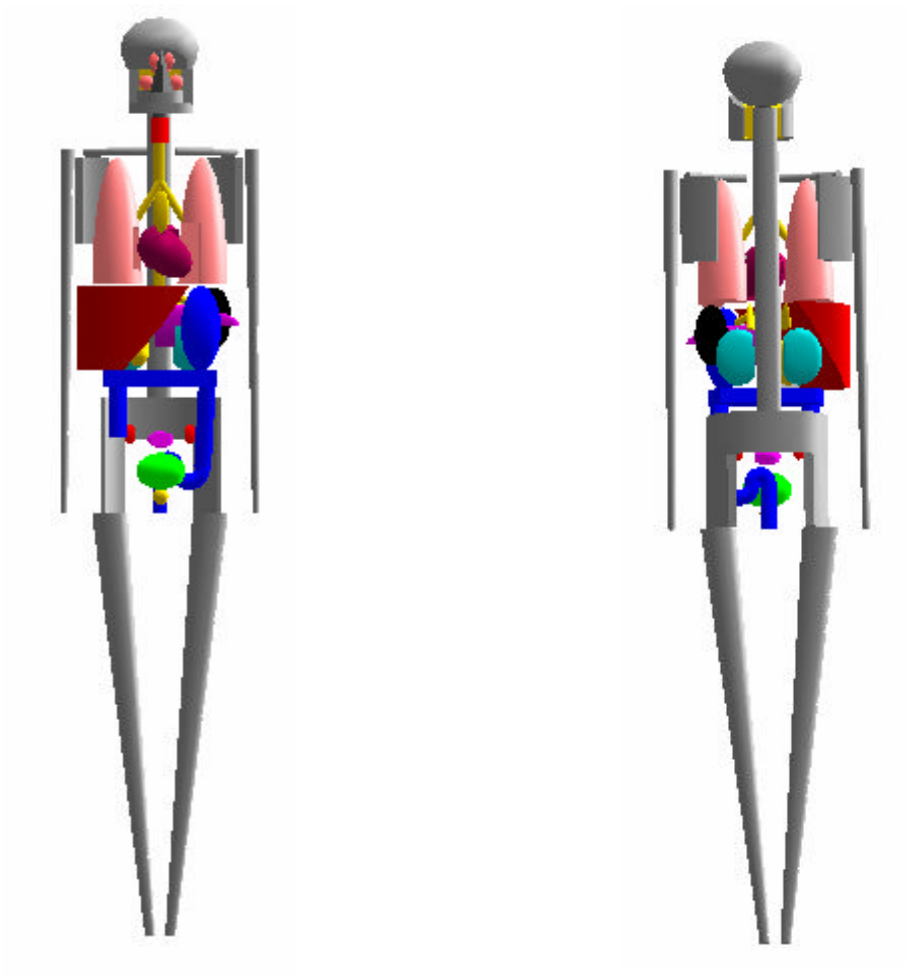

Fig. 4. The shape of the internal organs, front (left) and back (right) after removing the ribs.

2.1 COMPOSITION OF THE MAJOR ORGANS

Traditionally, in the stylized phantoms, three tissue compositions were used: lung, bone, and soft tissue.

Table 1 presents the elemental compositions and densities for the MIRD-5 phantom model. In this model, the elemental composition of the soft tissue was used to describe all the remaining organs.

Table 1. The elemental compositions and densities for the MIRD-5 phantom model

Organ	Density (g/cm^3)	H	C	N	O	Ca	Na	P	S	Cl	K
Lung	0.296	10.1	10.2	2.9	75.8	—	0.2	0.1	0.2	0.3	0.2
Bone	1.4	7.3	25.5	3.1	47.9	10.2	0.3	5.1	0.2	0.1	0.1
Soft tissue	1.04	10.5	22.6	2.5	63.5	—	0.1	0.1	0.2	0.1	0.2

In the ORNL-UF phantom model, the elemental compositions and densities of the major organs were updated according to ICRP Publication 89 (Ref. 8) reference values. Table 2 presents the elemental compositions and densities of all the major organs for the ORNL-UF phantom model. As can be seen from Table 1 and Table 2, there is no significant change in the elemental composition of the lung, bone, and soft tissue between the MIRD-5 and ORNL-UF phantom models. However, in the ORNL-UF phantom model instead of using the soft tissue composition to describe the elemental composition for all the other organs, the corresponding compositions were updated, as shown in Table 2.

Compared to soft tissue composition, the main differences in the updated organ compositions can be summarized as:

- The primary difference is the carbon and oxygen content. The carbon content decreased 5–15 percent for all organs except the uterus and breast. The decrease in the carbon content was added to the oxygen content.

- For the eyes and skin, the nitrogen content also increased. There is less increase in nitrogen content for the heart, spleen, and muscle. For the breast, there is no nitrogen.

- For the uterus and breast, the carbon content increased. Especially for the breast, the carbon content is doubled.

- There is a slight change in density for all organs. This change in density is more evident for the breast.

- The change in hydrogen content is within ±1 percent for all organs. The maximum change is for the larynx, eyes (-1 percent), and breast (+1 percent).

The impact of the composition on the organ doses is investigated in Section 4 of this report.

Table 2. Elemental composition of the major organs for the ORNL-UF phantom model

Organ	Density (g/cm^3)	H	C	N	O	Ca	Na	P	S	Cl	K
Lung	0.26	10.3	10.5	3.1	74.9	—	0.2	0.2	0.3	0.3	0.2
Bone	1.4	7.3	25.5	3.1	47.9	10.2	0.3	5.1	0.2	0.1	0.1
Soft tissue	1.03	10.5	25.6	2.7	60.2	—	0.1	0.2	0.3	0.2	0.2
Muscle	1.05	10.2	14.3	3.4	71.0	—	0.1	0.2	0.3	0.1	0.4
Skin	1.09	10.0	20.4	4.2	64.5	—	0.2	0.1	0.2	0.3	0.1
Brain	1.04	10.7	14.5	2.2	71.2	—	0.2	0.4	0.2	0.3	0.3
Eyes	1.07	9.6	19.5	5.7	64.6	—	0.1	0.1	0.3	0.1	—
Thyroid	1.05	10.4	11.9	2.4	74.5	—	0.2	0.1	0.1	0.2	0.1
Upper face	1.22	8.9	24.1	2.8	55.7	5.1	0.2	2.6	0.2	0.1	0.2
Larynx	1.10	9.6	9.9	2.2	74.4	—	0.5	2.2	0.9	0.3	—
Trachea	1.03	10.5	25.6	2.7	60.2	—	0.1	0.2	0.3	0.2	0.2
GI Tract	1.03	10.6	11.5	2.2	75.1	—	0.1	0.1	0.1	0.2	0.1
Testes	1.04	10.6	9.9	2.0	76.6	—	0.2	0.1	0.2	0.2	0.2
Ovaries	1.05	10.5	9.3	2.4	76.8	—	0.2	0.2	0.2	0.2	0.2
Uterus	1.02	10.6	31.5	2.4	54.7	—	0.1	0.2	0.2	0.1	0.2
Urinary bladder	1.04	10.5	9.6	2.6	76.1	—	0.2	0.2	0.2	0.3	0.3
Spleen	1.06	10.3	11.3	3.2	74.1	—	0.1	0.3	0.2	0.2	0.3
Heart	1.05	10.4	13.9	2.9	71.8	—	0.1	0.2	0.2	0.2	0.3
Pancreas	1.04	10.6	16.9	2.2	69.4	—	0.2	0.3	0.1	0.2	0.2
Liver	1.05	10.3	18.6	2.8	67.1	—	0.2	0.2	0.3	0.2	0.3
Kidneys	1.05	10.3	13.2	3.0	72.4	0.1	0.2	0.2	0.2	0.2	0.2
Breast	0.94	11.6	51.9	—	36.5	—	—	—	—	—	—

3. BENCHMARK COMPUTATIONS

A joint task group of the ICRP and International Commission on Radiation Units (ICRU) compiled fluence-to-dose conversion coefficients for external exposure to neutron and photon sources using the previously published data. The work of the joint committee of the ICRP and ICRU[13] was published as ICRP Publication 74 and ICRU Report 57.[‡]

The organ dose coefficients were computed by various researchers using adult mathematical phantom models implemented in different Monte Carlo codes using different radiation cross-section data sets. The report recommends neutron and photon coefficients for 13 organs and tissues (12 anatomical regions plus the remainder group of tissues in the definition of the ICRP's tissue-weighting factors). The organ coefficients were calculated for six different irradiation (exposure) geometries to monoenergetic radiation fields.

In the following sections, the exposure geometries and some background information on the values reported in ICRP and ICRU reports are presented. Furthermore, benchmark results with a discussion on the reasons behind the discrepancies or differences in the coefficients for some of the organs are investigated.

3.1 SOURCE GEOMETRIES

Computations were performed for the standard ICRP exposure geometries, in which it is assumed that the whole body is irradiated by broad monoenergetic unidirectional or parallel plane beams.

The irradiation geometries are illustrated in Fig. 5 through Fig. 9 and are described below.

- **Antero-posterior** (AP) source geometry—the direction of the beam is from the front of the body to the back, as shown in Fig. 5.

- **Postero-anterior** (PA) source geometry—the beam irradiates the body from back to front, as shown in Fig. 6.

- **Right lateral** (RLAT) and **left lateral** (LLAT) source geometry—the beam irradiates the body from the right (RLAT) and left (LLAT) side of the body, as shown in Fig. 7 and Fig. 8, respectively.

In these geometries, the beam is monodirectional.

- **Isotropic** source (ISO) geometry—the radiation field has no preference of direction; the particle flux per unit solid angle is constant. This source geometry was modeled by putting the phantom in a sphere and having the particles incident from all directions, as shown in Fig. 9.

[‡] The numerical values reported in both reports are the same since this was a joint study between the two groups.

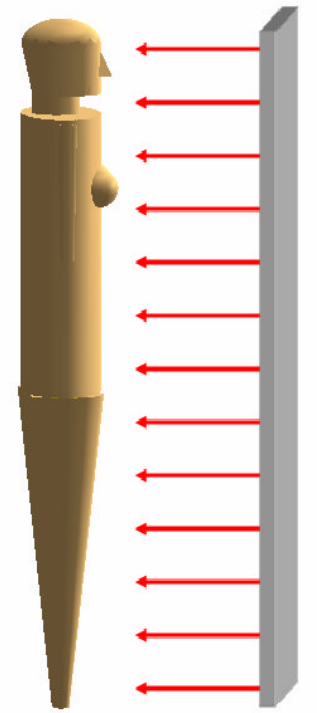

Fig. 5. Antero-posterior (AP) irradiation geometry.

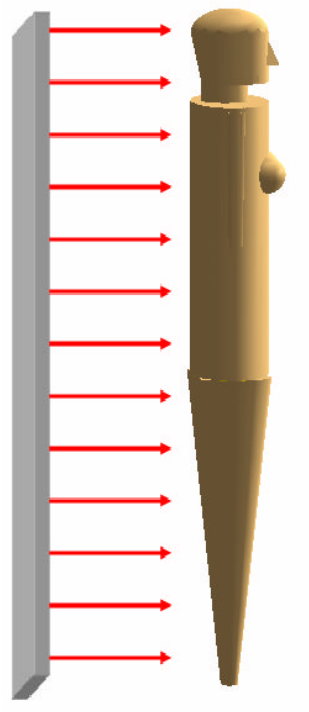

Fig. 6. Postero-anterior (PA) irradiation geometry.

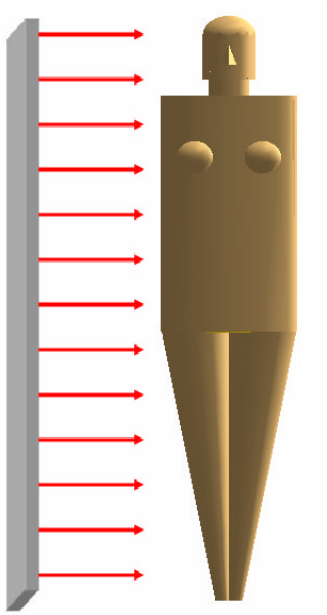

Fig. 7. Right lateral (RLAT) irradiation geometry.

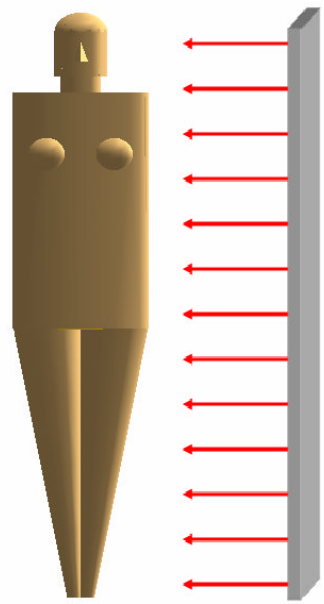

Fig. 8. Left lateral (LLAT) irradiation geometry.

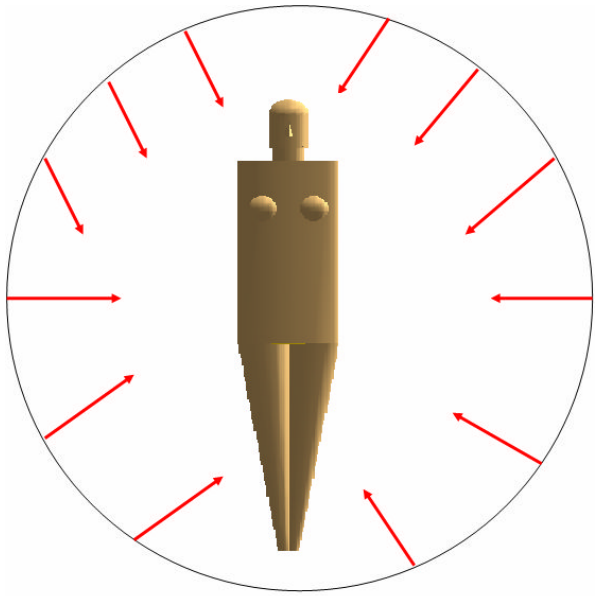

Fig. 9. Isotropic (ISO) irradiation geometry.

3.2 BACKGROUND ON CONVERSION COEFFICIENTS REPORTED IN ICRP-74

The conversion coefficients reported in ICRP-74 and ICRU-57 are based on the compilation of data from different sources. The data of various researchers, generated using different phantom models, computer codes, and cross-section data sets for the radiation transport simulations were compiled and averaged to derive the tabulated coefficients. The phantom models, codes, and nuclear data used for the values reported in ICRP-74 (Ref. 9) and ICRU-57 (Ref. 13) can be summarized as:

- **Phantom model:** Calculations were performed either using a hermaphrodite MIRD-5 phantom or modified MIRD-based, gender-specific phantoms (ADAM and EVA). Not only were the phantom models different, but the number of organs also varied from 20 to 40, depending on the model.

- **Computer codes:** For neutron source calculations, the MCNP, SAM-CE, MORSE-CG, and HL-PH codes were used. For photon source calculations, the reported data is based primarily on the calculations performed using the JEUNESSE and GSF codes.

- **Nuclear data:** Neutron source calculations were performed using ENDF/B-IV, ENDF/B-V, and JENDL-3 nuclear data. For photons, the computations were performed using ENDF/B-V for the GSF code and Hubbell for the JEUNESSE code.

- **Number of energy points:** For neutrons, the number of energy points varied from 14 to 33, while the energy range varied from thermal to 20 MeV. For photon-source calculations, the number of energy points was 12 for JEUNESSE calculations and 17 for GSF calculations. For the photon source, two additional conversion sets were used; however, the number of energy points for these two evaluations was only three.

To derive the conversion coefficients reported in ICRP-74, the values from these different investigators were plotted and the best fit to the data was adopted. The variability in the compiled values was reported to be significant for neutrons for some of the organs, especially for some of the geometries. A few examples, taken from the ICRP-74, are included in the following figures.

For example, Fig. 10 shows the data (identified by institution) and evaluated data (in solid lines) corresponding to the liver for the PA geometry. As shown in the figure, in general, there is a good agreement between the computed values for this organ. However, a much greater spread in the data for the thyroid is evident in Fig. 11. Similarly, for the colon, there is relatively better agreement between the data for LLAT geometry, as shown in Fig. 12; however, for RLAT geometry, there is a wide spread in the computed organ dose values for the same organ, as shown in Fig. 13. Although it is not discussed in detail, the reasons behind these discrepancies and the scatter in the data for some of the organs, especially for some of the irradiation geometries, were attributed to the differences in the phantom models, nuclear codes, and data used by different institutes.

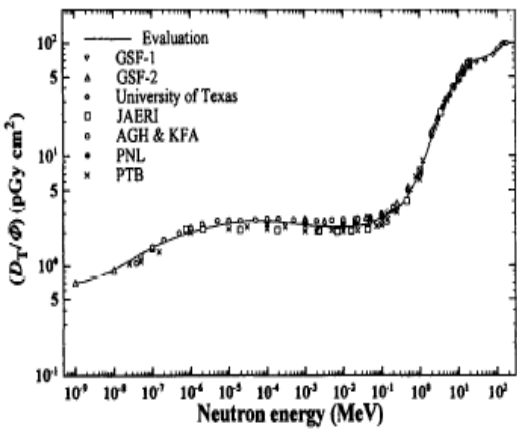

Fig. 10. Evaluated and original data for the mean absorbed dose to the liver in PA geometry.[9]

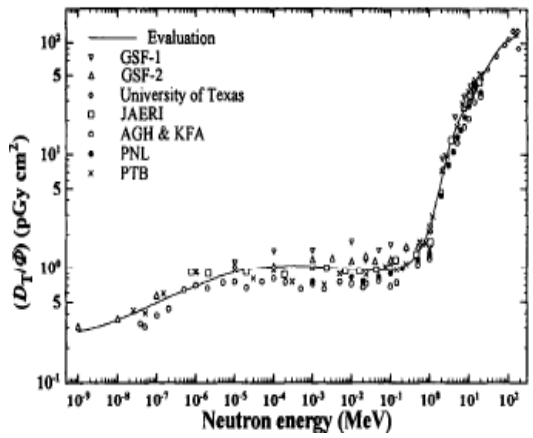

Fig. 11. Evaluated and original data for the mean absorbed dose to the thyroid in PA geometry.[9]

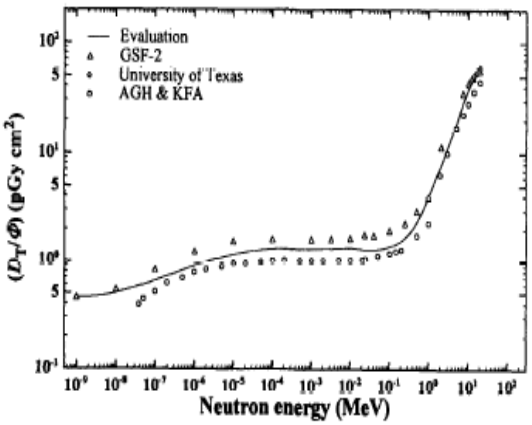

Fig. 12. Evaluated and original data for the mean absorbed dose to the colon in LLAT geometry.[9]

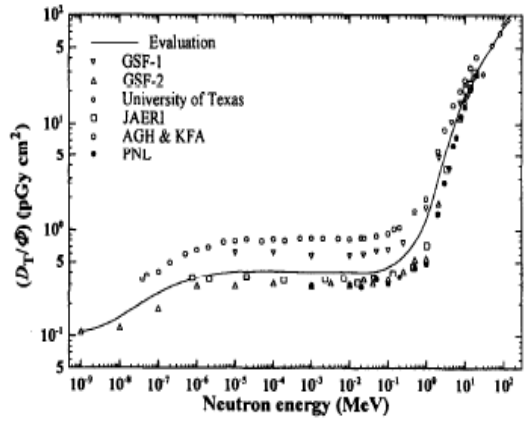

Fig. 13. Evaluated and original data for the mean absorbed dose to the colon in RLAT geometry.[9]

3.3 MCNP COMPUTATIONS

To compare the organ dose values calculated with the ORNL-UF phantom model with the values tabulated in ICRP-74, a series of Monte Carlo computations, using MCNP5 (Ref. 14), was performed. The computational results were benchmarked against the values reported in ICRP-74 and ICRU-57. The ICRP-74 values were downloaded from the radiation toolbox[15] since the values were readily available in electronic form.

The computations were performed for both the ORNL-UF and MIRD-5 phantom models to determine the impact of changes and also to benchmark both phantoms using the same Monte Carlo code and nuclear data. The computations were performed for neutron and photon sources for the five irradiation geometries described in the previous section. The neutron and photon sources were monoenergetic. For the neutron source, the energy range varied from 10^{-9} to 20 MeV. For the photon source, the energy range was between 30 keV and 10 MeV. Computations were performed for selected neutron and photon energies that correspond to a subset of the energies reported in ICRP-74.

The benchmark computations were performed using the ENDF/B-VI.6 neutron data. Sensitivity computations were performed to determine the impact of neutron data on the computed results, and these will be presented in the next section. The organ dose values were computed using the F6 tally. For the photon source, the problem mode was photon; for the neutron source, the coupled neutron and photon mode was used to account for the secondary particles, photons, generated via neutron reactions.

The computations were performed on a Linux cluster using 20 million particles at each energy. To reduce the statistical uncertainty at lower energies, the number of particles was increased to 100 million. The computational benchmark results for some of the organs are presented in the following sections.

3.3.1 Benchmark Calculation Results for Photon Source

The computed organ dose values for the photon source, extracted from MCNP output, were normalized to the air kerma values given in ICRP-74. The organ dose values were compared with the reported ICRP-74 dose values. The ratio of computed values, using the ORNL-UF phantom model, and the values reported in ICRP-74 are shown for comparison purposes.

The absorbed dose per air kerma for the ***gonads*** (since the phantom is hermaphrodite, the average of the testes and ovaries dose represents the gonads dose) in the ORNL-UF model and as reported in ICRP-74 is shown in Fig. 14 (left). The solid lines show the computed values; dashed lines represent the evaluated data of ICRP-74. The ratio of computed-to-reported values is also shown in Fig. 14 (right). The computed and reported values for this organ are within ±10 percent agreement, which is within the reported uncertainty in ICRP-74.

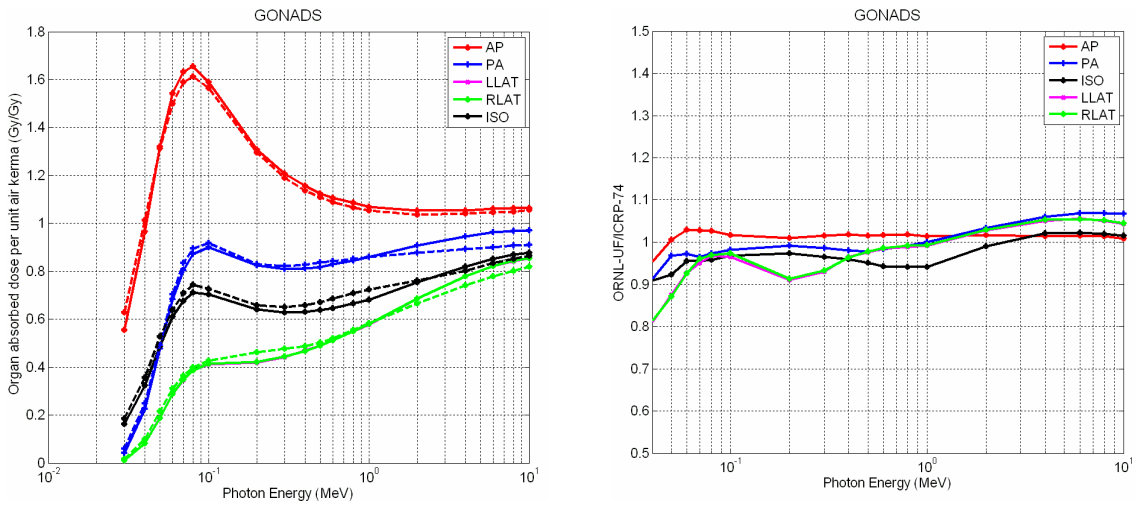

Fig. 14. The absorbed dose per air kerma for the ORNL-UF model (solid) and ICRP-74 values (dashed) to the gonads (left). The ratio of computed to ICRP-74 is shown on the right.

The absorbed dose per air kerma to the ***breast*** for the ORNL-UF model and the data reported in ICRP-74 are shown in Fig. 15 (left). In this figure, solid lines show the computed values and dashed lines represent the evaluated data reported in ICRP-74. The ratio of computed-to-reported values is shown on the right. At higher photon energies (greater than 0.2 MeV), the computed and reported values for this organ are within ±10 percent agreement, which is within the reported uncertainty. However, at lower energies (less than 0.1 MeV), the computed values are lower compared to the reported values.

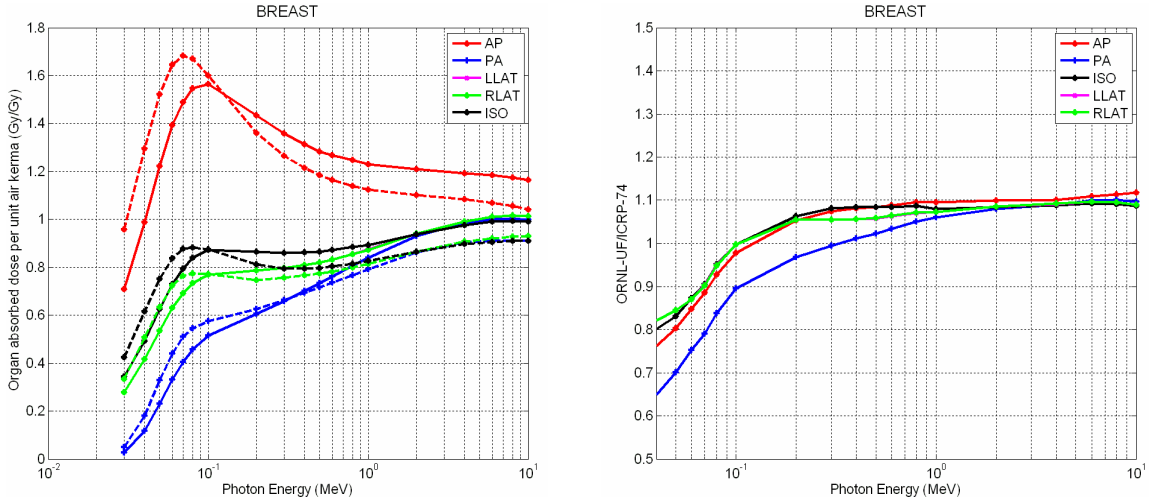

Fig. 15. The absorbed dose per air kerma for the ORNL-UF model (solid) and ICRP-74 values (dashed) to the breast. The ratio of computed to ICRP-74 is shown on the right.

The reasons behind the lower values at lower energies for breast were investigated. First, the computational results for the MIRD-5 phantom model were compared to the values reported for this organ. The comparison is shown in Fig. 16. As shown in the figure, the agreement between the computed and reported values is much better for the MIRD-5 phantom model. The reason is that the ICRP-74 computations were performed using three tissue compositions; therefore, the soft tissue composition was used to describe the breast. However, in the ORNL-UF phantom model, the breast composition has changed significantly, as it was presented in Table 2 of Sect. 2.1.

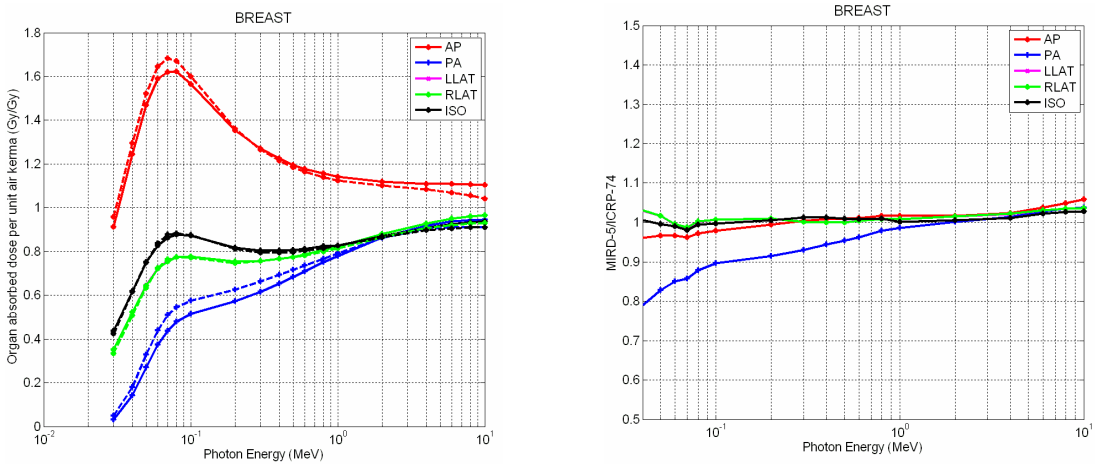

Fig. 16. The absorbed dose per air kerma for MIRD-5 phantom model (solid) and ICRP-74 values (dashed) to the breast. The ratio of computed to ICRP-74 is shown on the right.

The computations for the ORNL-UF model were repeated assuming that three compositions (lung, bone, soft tissue) were used to describe all the organs. This will be discussed in further detail in the following section. For completeness, the results with 23 compositions vs. 3 compositions for the ORNL-UF model are shown in Fig. 17 (left). As shown in the figure, the composition effect is more clearly observed for the breast at energies less than 0.2 MeV. The computed values are sensitive to the composition of the breast tissue since this organ is at the exterior of the phantom. The ratio of the computed organ dose for the breast using the ORNL-UF and the MIRD-5 phantom model shows the same behavior (MIRD-5 phantom model assumes three compositions for the descriptions of the organs' tissues) as shown in Fig. 17 (right).

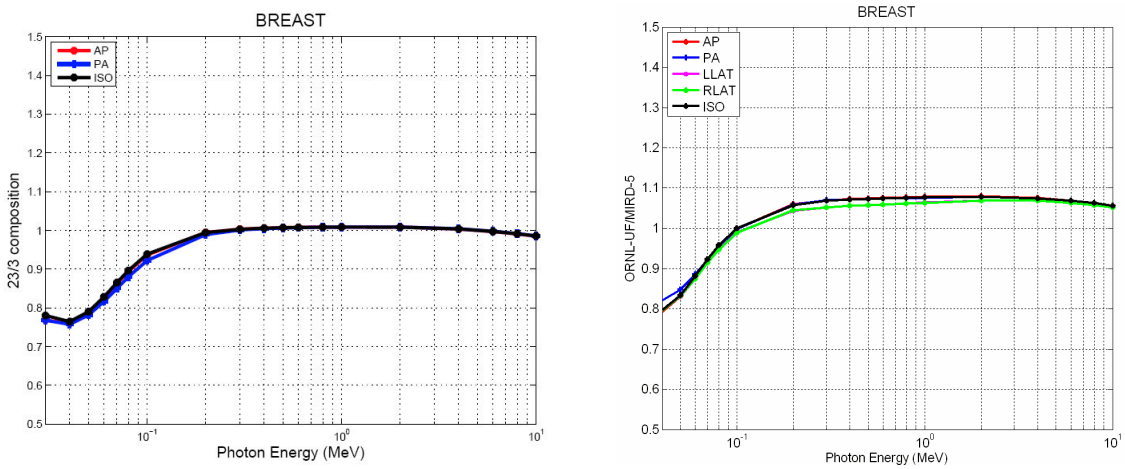

Fig. 17. The ratios of the computed organ dose values for the ORNL-UF model using 23 compositions vs. 3 compositions for the description of tissues (left) for breast. The ratio of the computed organ doses using the ORNL-UF and MIRD-5 phantom models (right).

The absorbed dose per air kerma to the ***esophagus*** for the ORNL-UF model and the data reported in ICRP-74 are shown in Fig. 18 (left). The solid lines show the computed values; dashed lines represent the evaluated data reported in ICRP-74. The ratio of computed-to-reported values is shown on the right. Except at lower energies, the computed and reported values for this organ are generally within ±10 percent agreement.

It is important to note that the esophagus is now considered to be one of the important organs for radiation dose assessment (tissue-weighting factor for esophagus is 0.05, which is equal to the tissue-weighting factor for thyroid); it was not included in the MIRD-5 phantom model. Similarly, some of the phantom models used in the ICRP-74 compilation were lacking this organ. For the data that includes this organ, there is a wide spread in the compiled values as discussed in ICRP-74 report.[8] Therefore, the discrepancies between the computed values and tabulated values in ICRP-74, especially at low energies, can be explained by the differences in models and the spread in the compiled data.

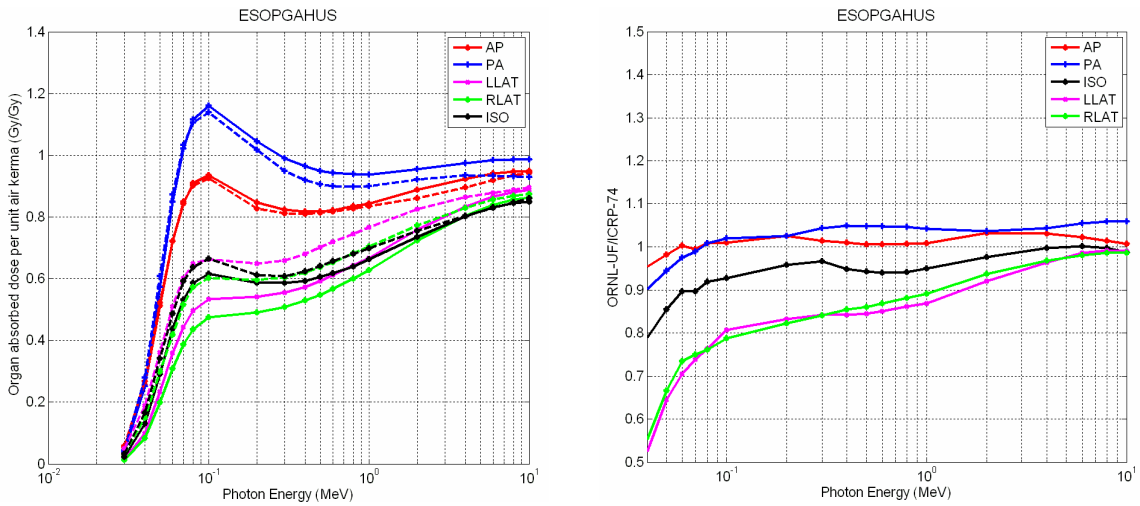

Fig. 18. The absorbed dose per air kerma for the ORNL-UF model (solid) and ICRP-74 values (dashed) to the esophagus. The ratio of computed to ICRP-74 is shown on the right.

The absorbed dose per air kerma for the ***thyroid*** in the ORNL-UF model and as tabulated in ICRP-74 is shown in Fig. 19 (left). Solid lines show the computed values and dashed lines represent the evaluated data reported in ICRP-74. The ratio of computed-to-reported values is shown on the right. The computed and reported values for this organ differ from each other significantly, especially for the PA source geometry.

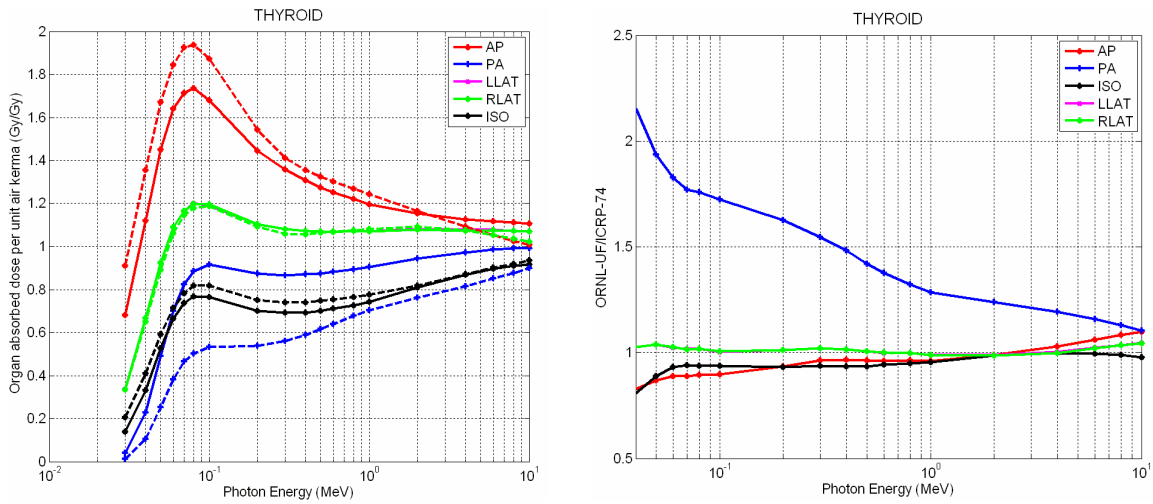

Fig. 19. The absorbed dose per air kerma for the ORNL-UF model (solid) and ICRP-74 values (dashed) to the thyroid. The ratio of computed to ICRP-74 is shown on the right.

The reasons behind this significant discrepancy have been investigated, especially since the thyroid is an important organ in radiation protection. First, the computational results for the MIRD-5 phantom model were compared to the values reported for this organ. The comparison is shown in Fig. 20. As can be seen from the figure, the coefficients based on the MIRD-5 phantom model are lower than the coefficients reported in ICRP-74 for the PA geometry. However, the coefficients based on the ORNL-UF model were greater than the coefficients reported in ICRP-74 (see Fig. 19).

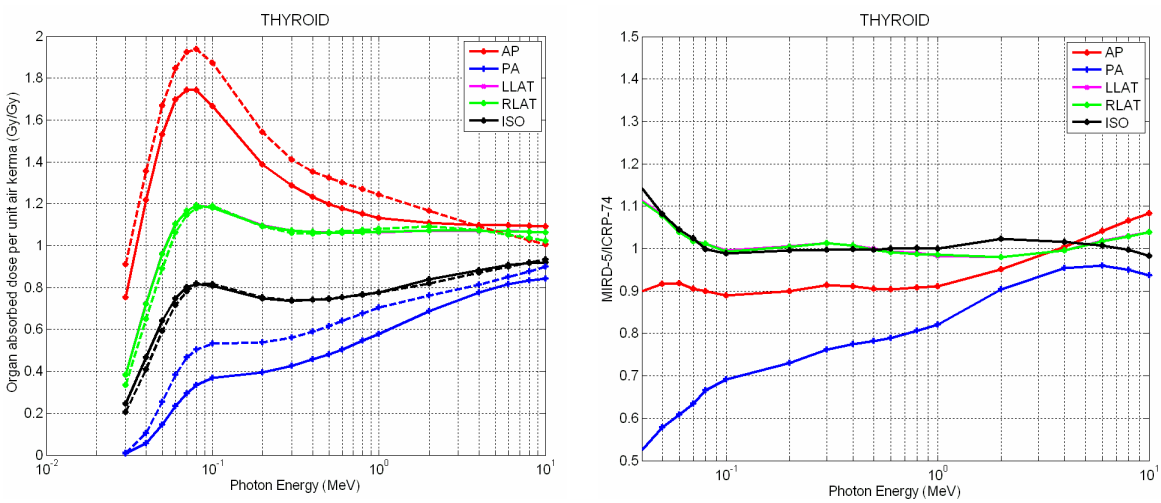

Fig. 20. The absorbed dose per air kerma for the MIRD-5 phantom model (solid) and ICRP-74 values (dashed) to the thyroid. The ratio of computed to ICRP-74 is shown on the right.

The ratio of the computed organ dose values using the MIRD-5 and ORNL-UF phantom models is shown in Fig. 21. As can be seen more clearly from this figure, the main difference is observed for the PA irradiation geometry.

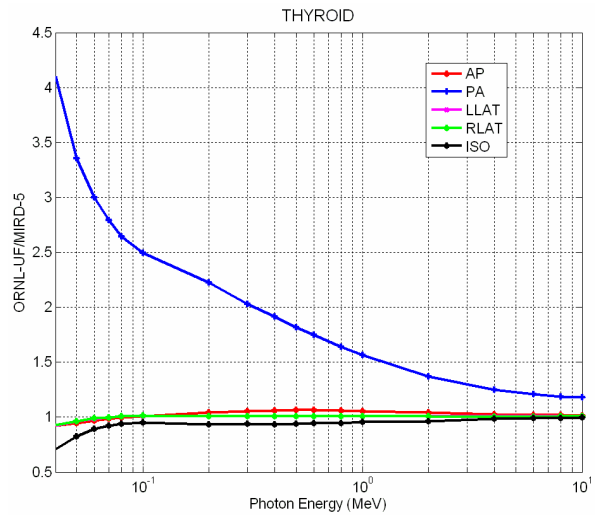

Fig. 21. The ratio of the computed absorbed dose values to the thyroid using the MIRD-5 and ORNL-UF phantom models.

Although the elemental composition of the thyroid in the ORNL-UF model differs slightly from the soft tissue composition of MIRD-5, the sensitivity computations showed that the reason for the discrepancy cannot be explained with the composition change. As Fig. 22 shows, the ratio is almost constant for both compositions.[§]

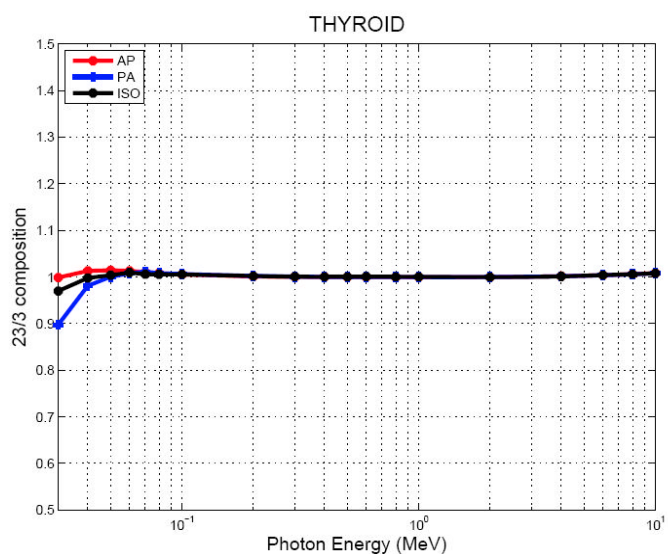

Fig. 22. The ratio of the thyroid dose for the ORNL-UF phantom model with 23 compositions vs. 3 compositions.

[§] The elemental compositions of all organs were changed. The phrase "23 compositions" refers to the ORNL-UF model with the compositions specified for each organ, and "3 compositions" refers to the ORNL-UF model assuming the three compositions (lung, soft tissue, and bone).

Further analysis showed that the discrepancy between the values tabulated in ICRP-74 and the values computed using both the ORNL-UF and the MIRD-5 phantom models for the PA geometry is mainly due to the differences in the thyroid locations relative to the body surface. Furthermore, as shown in Fig. 11, there is a considerable spread in the reported values for this organ. Although the details of the phantoms used for ICRP-74 computations are unclear, it is stated in the ICRP-74 report[9] that not all the phantoms included the neck model. This distinction is very important since the presence of the neck changes the depth of the thyroid in the phantom model. To illustrate this, the front, side, and top views of the ORNL-UF and the MIRD-5 phantom models are shown in Fig. 23 and 24, respectively. As shown in these figures, when there is no neck (as is the case for the MIRD-5 phantom model), for the PA geometry, the scattering and attenuation medium for the radiation source is increased; hence, the absorbed dose in the thyroid is decreased. This effect is more dominant at low energies for the PA geometry.

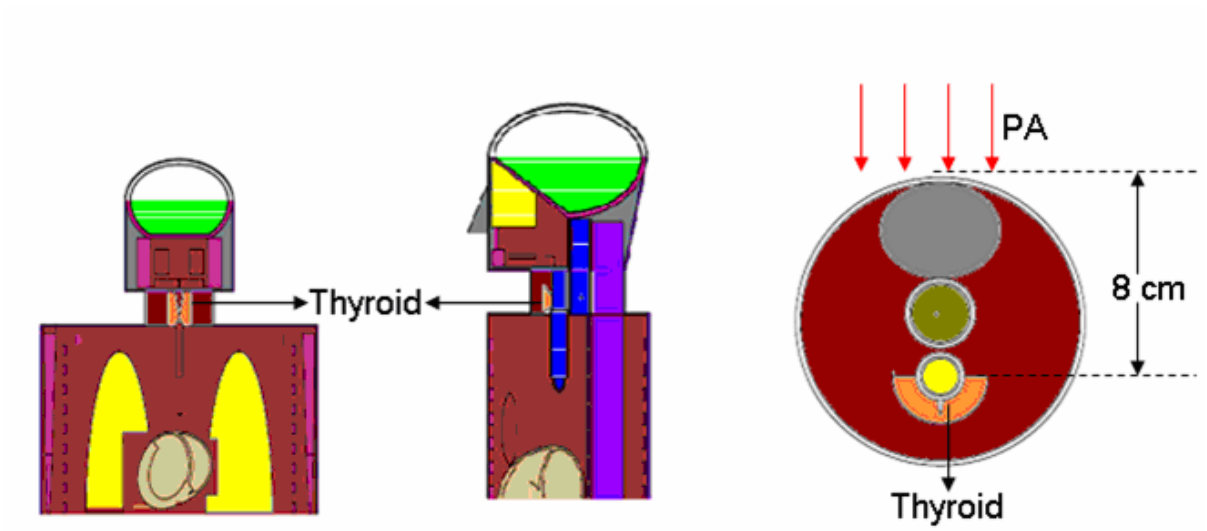

Fig. 23. The front (left), side (middle), and top (right) view of the location of the thyroid in the ORNL-UF phantom model.

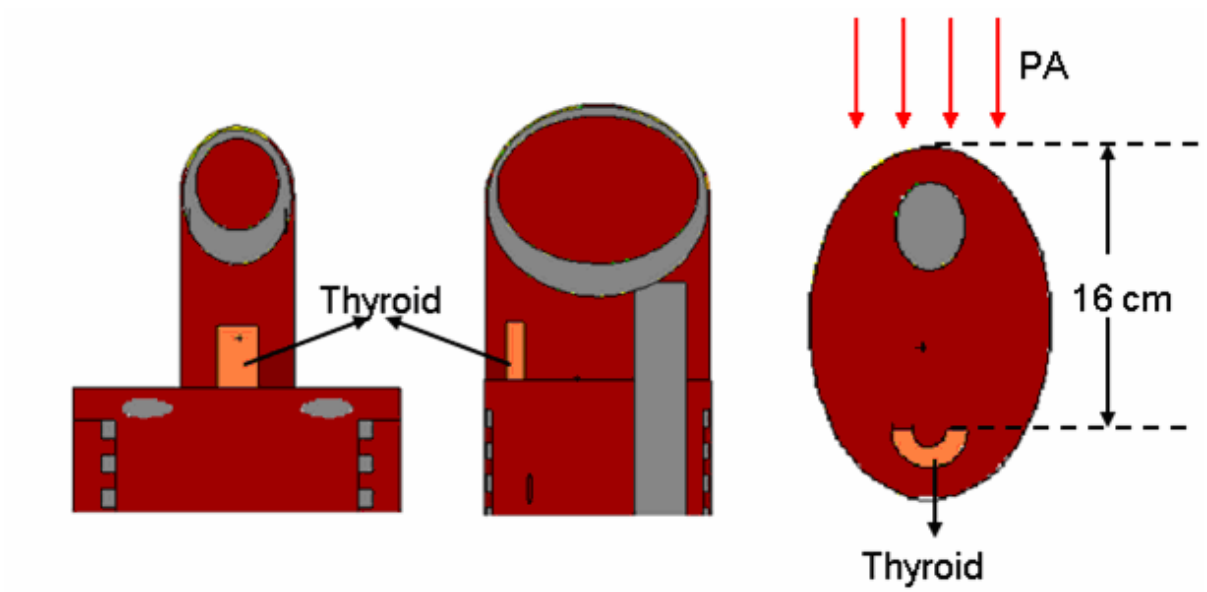

Fig. 24. The front (left), side (middle), and top (right) view of the location of the thyroid in the MIRD-5 phantom model.

The absorbed dose per air kerma to the ***colon*** for the ORNL-UF model and the values tabulated in ICRP-74 are shown in Fig. 25 (left). Solid lines show the computed values and dashed lines represent the evaluated data reported in ICRP-74. The ratio of computed-to-reported values is shown on the right. The computed and reported values for this organ are within ±10 percent agreement, which is within the reported uncertainty in ICRP-74.

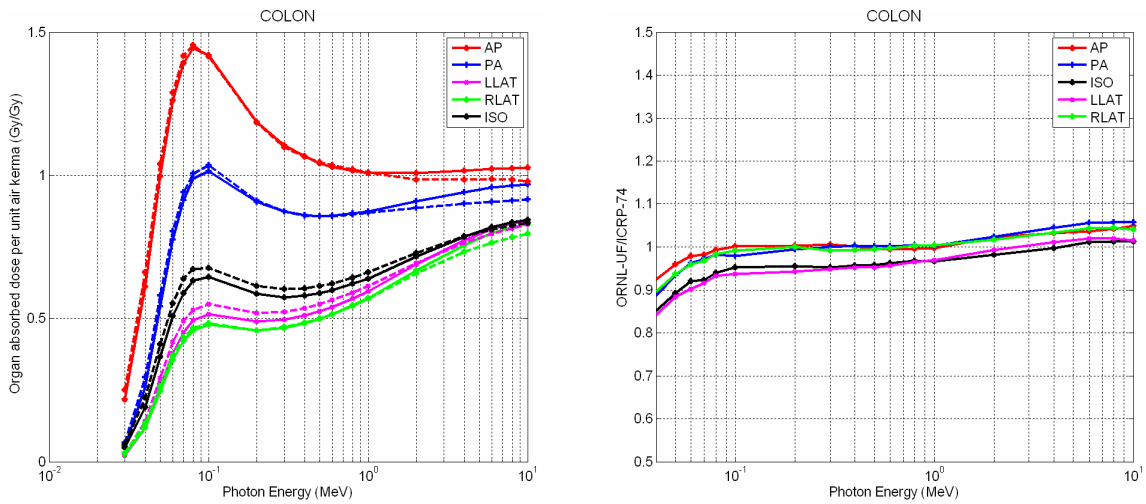

Fig. 25. The absorbed dose per air kerma for the ORNL-UF model (solid) and ICRP-74 values (dashed) to the colon. The ratio of computed to ICRP-74 is shown on the right.

The absorbed dose per air kerma to the ***liver*** for the ORNL-UF model and the values reported in ICRP-74 are shown in Fig. 26 (left). Solid lines show the computed values and dashed lines represent the evaluated data reported in ICRP-74. The ratio of computed-to-reported values is shown on the right. The computed and reported values for this organ are within ±10 percent agreement, except for the LLAT geometry at low energies, which is within the reported uncertainty. For the LLAT geometry, below 0.1 MeV, the computed values are lower than those reported in ICRP-74. This is mainly due to the composition change in the ORNL-UF model. Since the liver is on the right side of the body and the source is on the left, the change in the elemental composition did cause a change in the self-shielding and attenuation effect.

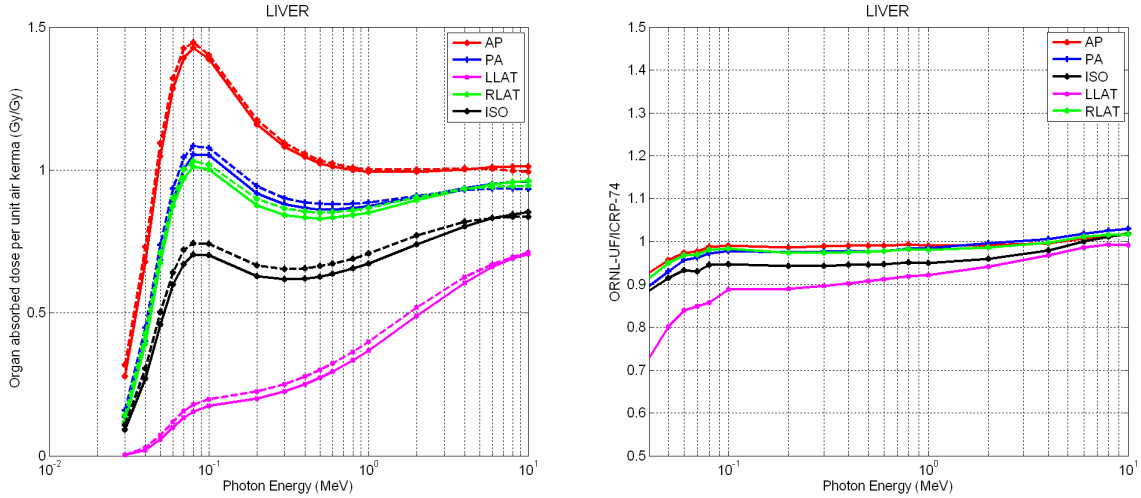

Fig. 26. The absorbed dose per kerma for the ORNL-UF model (solid) and ICRP-74 values (dashed) to the liver. The ratio of computed to ICRP-74 is shown on the right.

The absorbed dose per air kerma to the ***lung*** for the ORNL-UF model and the values tabulated in ICRP-74 are shown in Fig. 27 (left). Solid lines show the computed values and dashed lines represent the evaluated data reported in ICRP-74. The ratio of computed-to-reported values is shown on the right. The computed and reported values for this organ are within ±10 percent agreement, which is within the reported uncertainty.

The lung absorbed dose values for RLAT and LLAT geometry are different since the mass and volume for the right and left lung are different in the ORNL-UF phantom model. In the MIRD-5 model, it was assumed that the mass and volume of both lungs are the same.

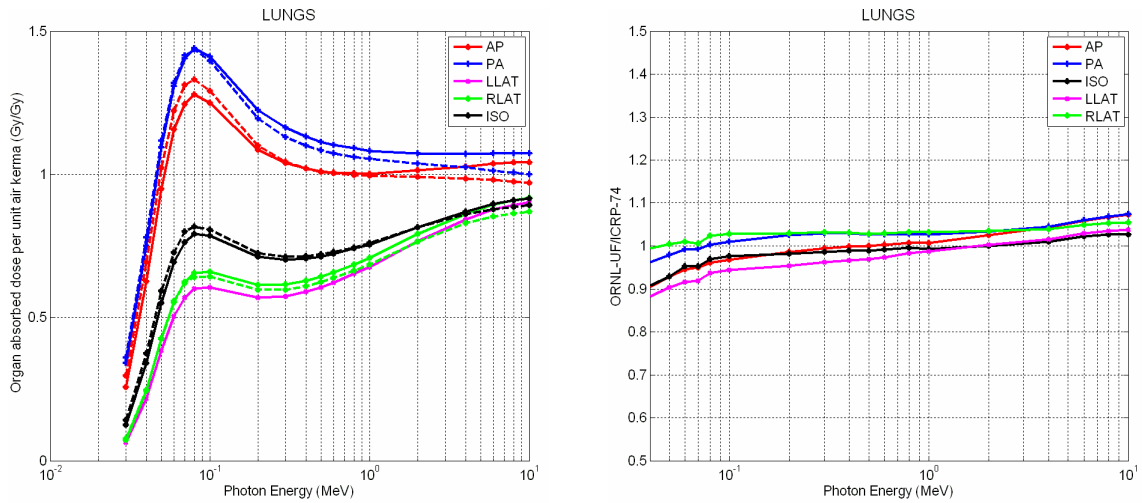

Fig. 27. The absorbed dose per air kerma for the ORNL-UF model (solid) and ICRP-74 values (dashed) to the lungs. The ratio of computed to ICRP-74 is shown on the right.

The absorbed dose per air kerma to the ***stomach*** for the ORNL-UF model and the values as tabulated in ICRP-74 are shown in Fig. 28 (left). Solid lines show the computed values and dashed lines represent the evaluated data reported in ICRP-74. The ratio of computed-to-reported values is shown on the right. As the figure shows, higher coefficients are obtained using the ORNL-UF model than that tabulated in ICRP-74.

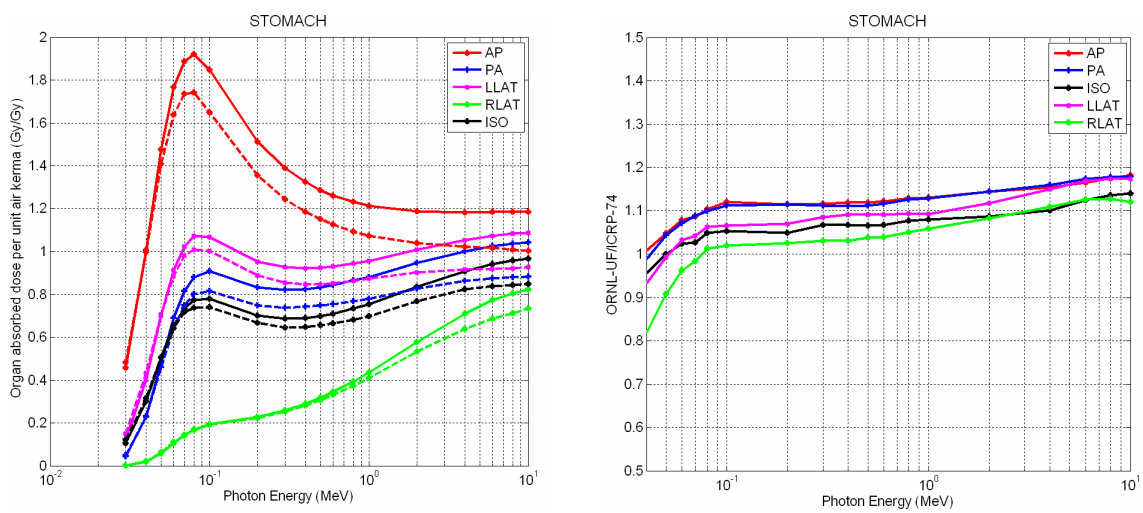

Fig. 28. The absorbed dose per air kerma for the ORNL-UF model (solid) and ICRP-74 values (dashed) to the stomach. The ratio of computed to ICRP-74 is shown on the right.

The absorbed dose per air kerma to the ***bladder*** for the ORNL-UF model and the values as tabulated in ICRP-74 are shown in Fig. 29 (left). Solid lines show the computed values and dashed lines represent the evaluated data reported in ICRP-74. The ratio of computed-to-reported values is shown on the right. The computed and reported values for this organ are within ±10 percent agreement, which is within the reported uncertainty.

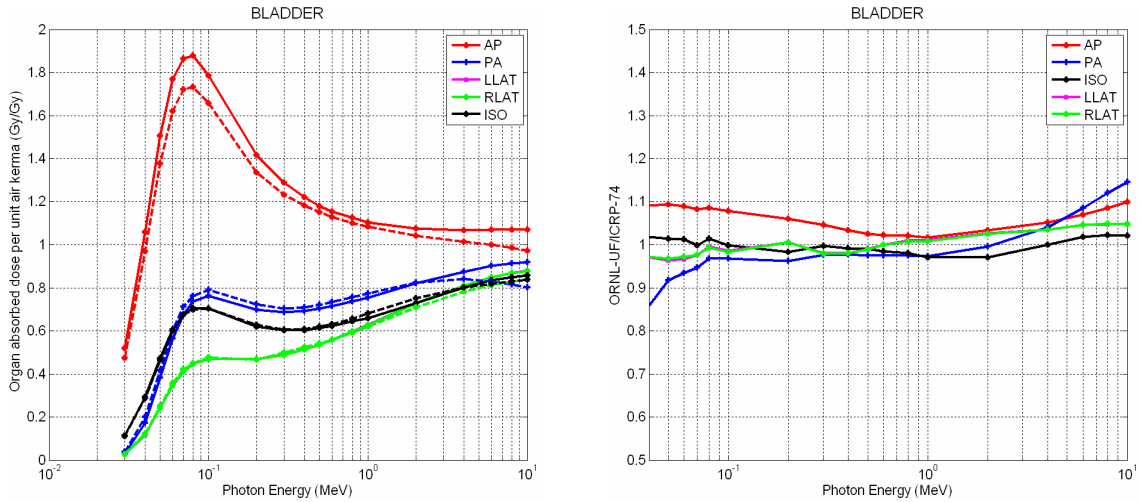

Fig. 29. The absorbed dose per air kerma for the ORNL-UF model (solid) and ICRP-74 values (dashed) to the bladder. The ratio of computed to ICRP-74 is shown on the right.

3.3.2 Benchmark Calculation Results for Neutron Source

In this section, the computed organ dose values are compared against the values reported in ICRP-74 for the neutron sources. The ratios of the computed values using the ORNL-UF phantom model and the values reported in ICRP-74 are also plotted and shown for comparison purposes.

As discussed in Section 3.2, the values tabulated in ICRP-74 were based on the compilation of the values published by researchers using different phantom models, nuclear codes, and data. The computational results included in ICRP-74 were based on ENDF/B-IV and ENDF/B-V nuclear data. The computational results reported in this section are based on ENDF/VI.6. The current version of the MCNP no longer includes the ENDF/B-IV data. However, some sensitivity computations using different data sets for neutrons were performed and are presented in the next section.

The absorbed dose per unit neutron fluence to the ***gonads*** for the ORNL-UF model and the values tabulated in ICRP-74 are shown in Fig. 30 (left). Solid lines show the computed values and dashed lines represent the evaluated data reported in ICRP-74. The ratio of computed-to-reported values is also shown in Fig. 30 (right). The computed values and the values reported in ICRP-74 are within ±20 percent agreement for this organ.

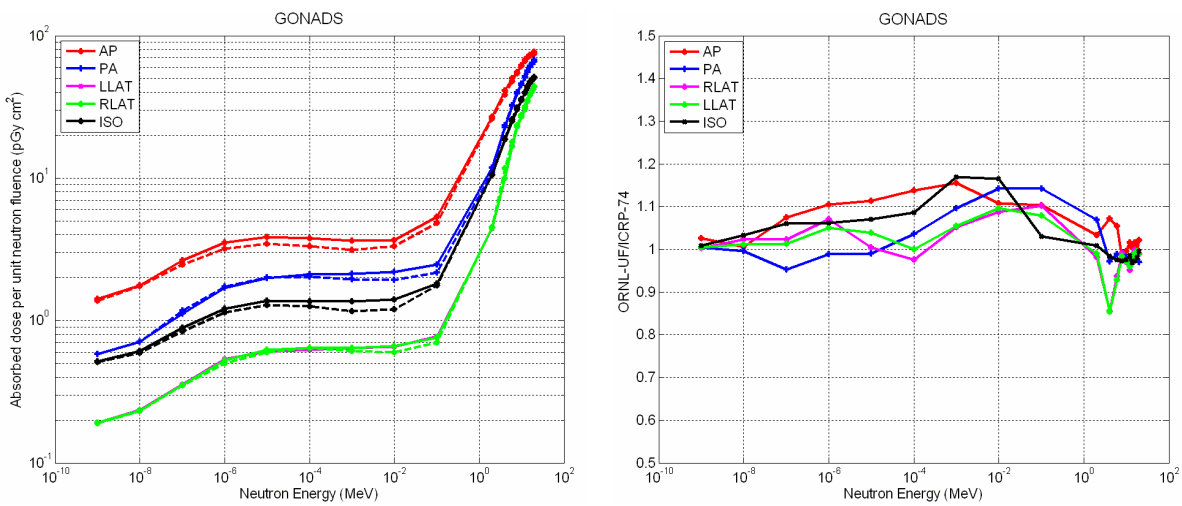

Fig. 30. Gonad absorbed dose per unit neutron fluence for the ORNL-UF model (solid) and ICRP-74 values (dashed). The ratio of computed to ICRP-74 is shown on the right.

The absorbed dose per unit neutron fluence to the ***breast*** for the ORNL-UF model and the values tabulated in ICRP-74 are shown in Fig. 31 (left). Solid lines show the computed values and dashed lines represent the evaluated data reported in ICRP-74. The ratio of computed-to-reported values is also shown in Fig. 31 (right). The computed and reported values for this organ are within ±20 percent agreement for source energies less than 1 MeV. However, above 1 MeV, for RLAT and LLAT source geometries, the discrepancy is up to 50 percent. The reason for this large deviation at high energies is unclear.

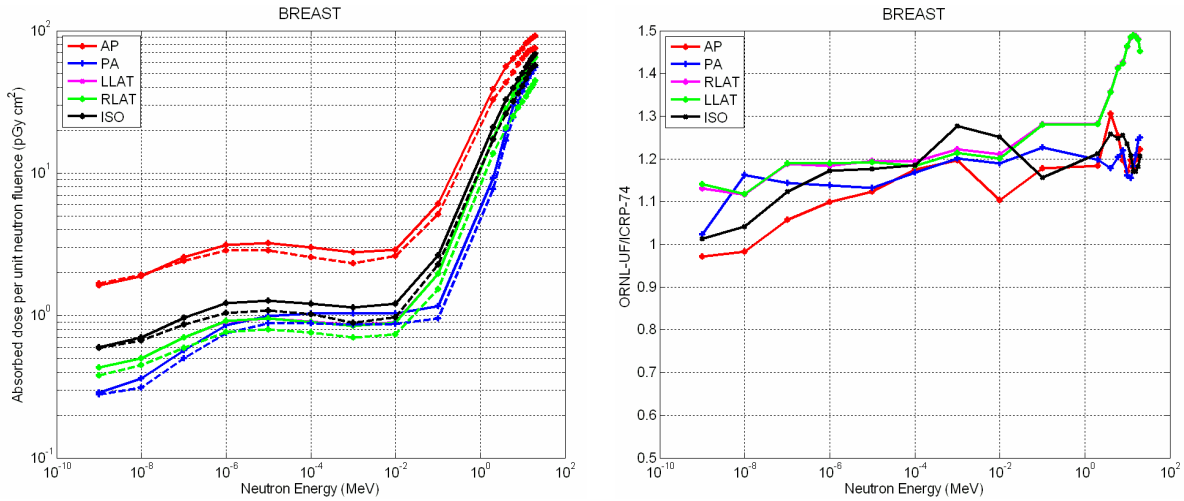

Fig. 31. Breast absorbed dose per unit neutron fluence for the ORNL-UF model (solid) and ICRP-74 values (dashed). The ratio of computed to ICRP-74 is shown on the right.

The absorbed dose per unit neutron fluence to the ***esophagus*** for the ORNL-UF model and the values tabulated in ICRP-74 are shown in Fig. 32 (left). Solid lines show the computed values and dashed lines represent the evaluated data reported in ICRP-74. The ratio of computed-to-reported values is also shown in Fig. 32 (right). The computed and reported values for this organ are within ±20 percent agreement for source energies less than 1 MeV. However, above 1 MeV, for AP and PA source geometries, the discrepancy is up to 40 percent. As discussed before, some of the phantom models included in ICRP-74 did not include an esophagus—this is also the case for the MIRD-5 phantom model. For models with an esophagus, a large spread in the computed values (due to the positioning of the esophagus) was reported. Since the differences are more clearly observed for AP and PA geometries, it seems that the depth of this organ in the ORNL-UF model is different from that assumed in ICRP-74.

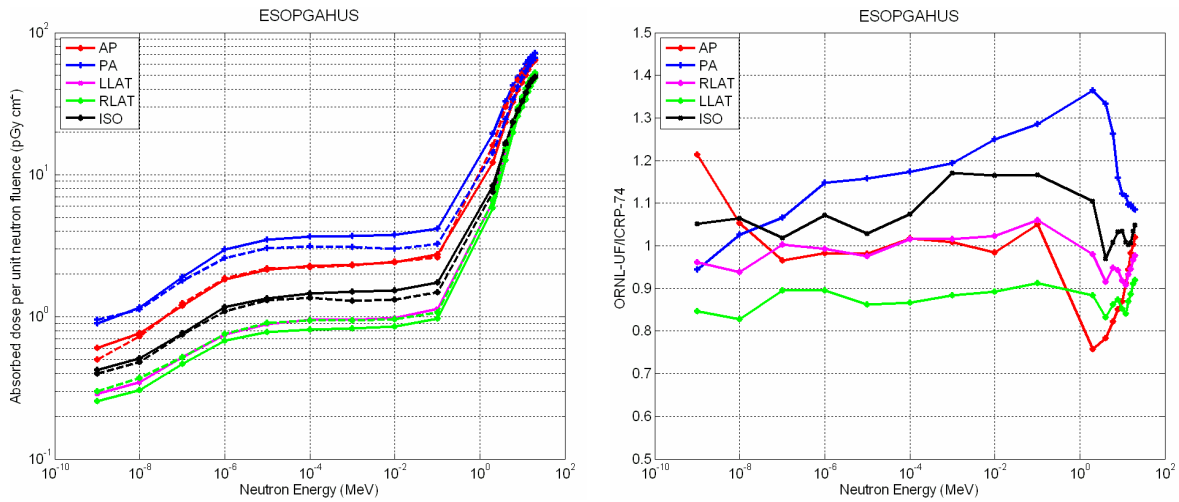

Fig. 32. Esophagus absorbed dose per unit neutron fluence for the ORNL-UF model (solid) and ICRP-74 values (dashed). The ratio of computed to ICRP-74 is shown on the right.

The absorbed dose per unit neutron fluence to the ***thyroid*** for the ORNL-UF model and the values tabulated in ICRP-74 are shown in Fig. 33 (left). Solid lines show the computed values and dashed lines represent the evaluated data reported in ICRP-74. The ratio of computed-to-reported values is also shown in Fig. 33 (right). These values show significant discrepancies, especially for the PA geometry. As discussed in detail in the previous section, the reason for these discrepancies, especially for the PA geometry is due to the location (depth) of this organ in the phantom model, which is dependent upon whether or not the phantom model included the neck.

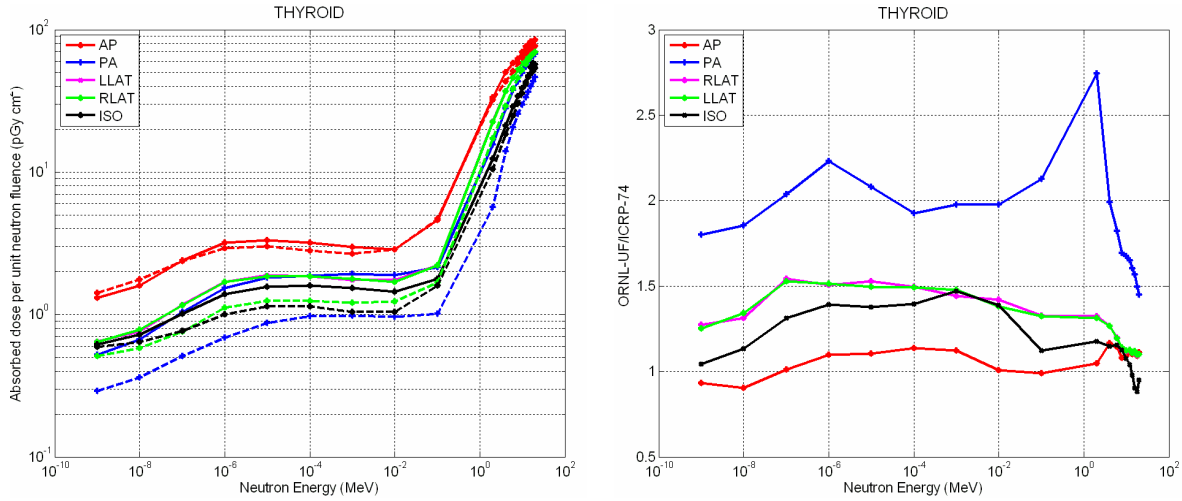

Fig. 33. Thyroid absorbed dose per unit neutron fluence for the ORNL-UF model (solid) and ICRP-74 values (dashed). The ratio of computed to ICRP-74 is shown on the right.

The absorbed dose per unit neutron fluence to the ***colon*** for the ORNL-UF model and the values tabulated in ICRP-74 are shown in Fig. 34 (left). Solid lines show the computed values and dashed lines represent the evaluated data reported in ICRP-74. The ratio of computed-to-reported values is also shown in Fig. 34 (right). The computed and reported values for this organ show significant discrepancies, especially for RLAT and LLAT geometry. The wide spread in the compiled data for this organ for LLAT and RLAT is shown in Fig. 12 and Fig. 13, respectively. The most probable reason for the significant variations, especially for these two source geometries, is the difference in the positioning of the colon in phantom models and possibly the difference in the definition of the colon in each model.

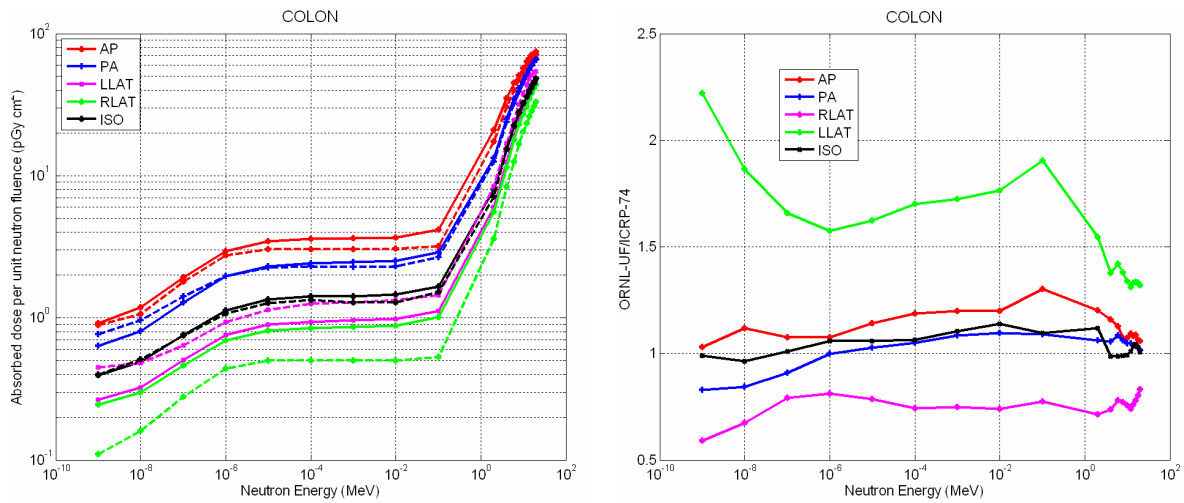

Fig. 34. Colon absorbed dose per unit neutron fluence for the ORNL-UF model (solid) and ICRP-74 values (dashed). The ratio of computed to ICRP-74 is shown on the right.

The absorbed dose per unit neutron fluence to the ***liver*** for the ORNL-UF model and the values tabulated in ICRP-74 are shown in Fig. 35 (left). Solid lines show the computed values and dashed lines represent the evaluated data reported in ICRP-74. The ratio of computed-to-reported values is also shown in Fig. 35 (right). The computed and reported values for this organ are in general within ±20 percent agreement for all source geometries.

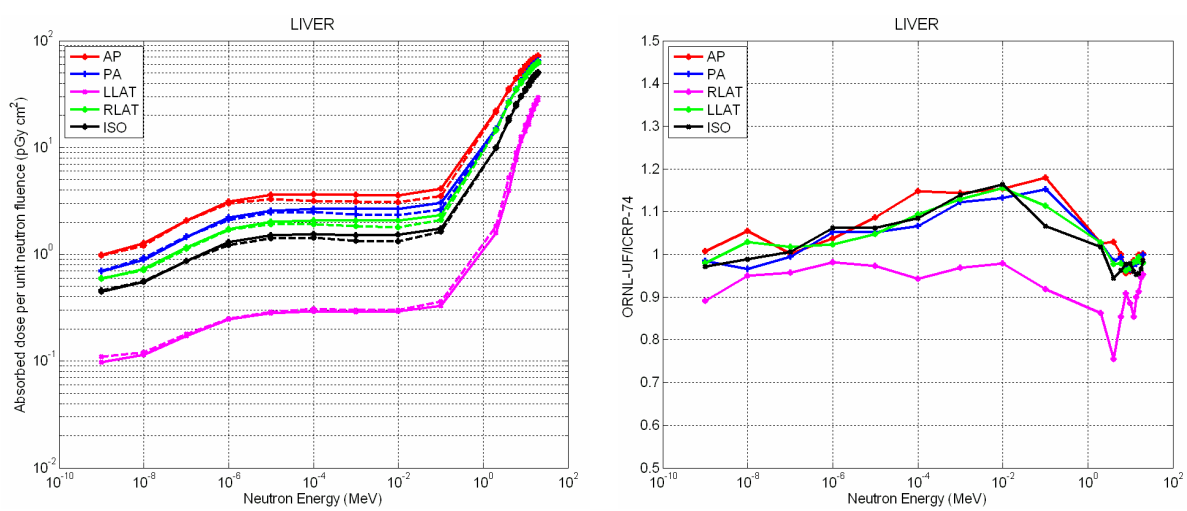

Fig. 35. Liver absorbed dose per unit neutron fluence for the ORNL-UF model (solid) and ICRP-74 values (dashed). The ratio of computed to ICRP-74 is shown on the right.

The absorbed dose per unit neutron fluence to the ***lungs*** for the ORNL-UF model and the values tabulated in ICRP-74 are shown in Fig. 36 (left). Solid lines show the computed values and dashed lines represent the evaluated data reported in ICRP-74. The ratio of computed-to-reported values is also shown in Fig. 36 (right). The computed and reported values for this organ are within ±20 percent agreement for all source geometries.

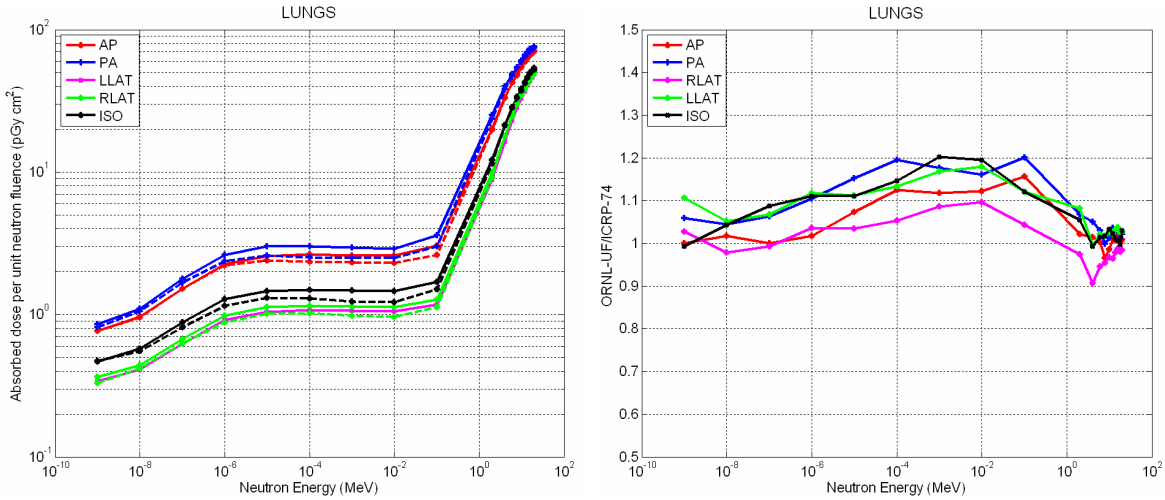

Fig. 36. Lung absorbed dose per unit neutron fluence for the ORNL-UF model (solid) and ICRP-74 values (dashed). The ratio of computed to ICRP-74 is shown on the right.

The absorbed dose per unit neutron fluence to the ***stomach*** for the ORNL-UF model and the values tabulated in ICRP-74 are shown in Fig. 37 (left). Solid lines show the computed values and dashed lines represent the evaluated data reported in ICRP-74. The ratio of computed-to-reported values is also shown in Fig. 37 (right). The computed and reported values for this organ show larger deviations, especially for the RLAT and LLAT geometries. This is most likely due to the differences in the organ location and definition.

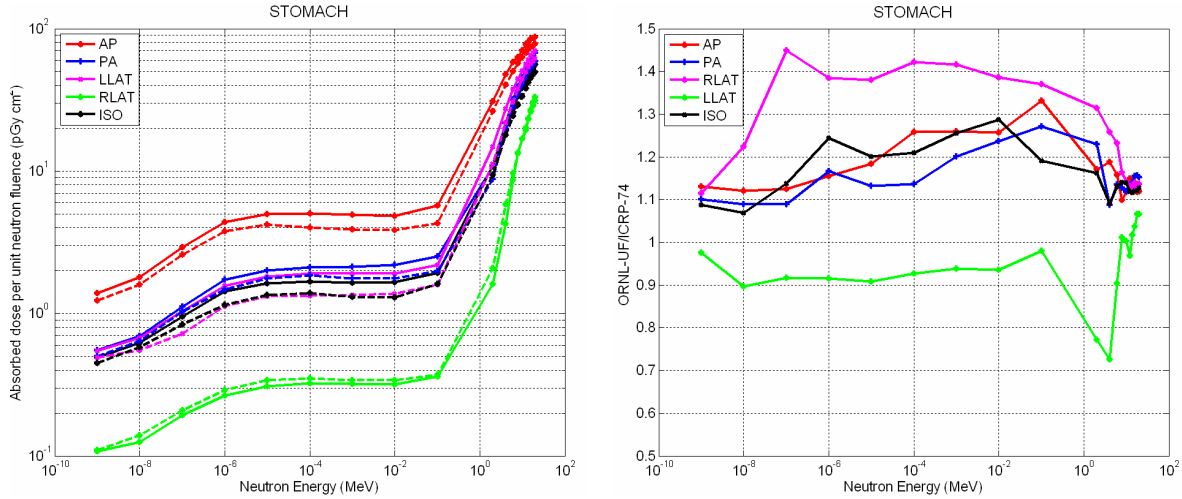

Fig. 37. Stomach absorbed dose per unit neutron fluence for the ORNL-UF model (solid) and ICRP-74 values (dashed). The ratio of computed to ICRP-74 is shown on the right.

The absorbed dose per unit neutron fluence to the ***bladder*** for the ORNL-UF model and the values tabulated in ICRP-74 are shown in Fig. 38 (left). Solid lines show the computed values and dashed lines represent the evaluated data reported in ICRP-74. The ratio of computed-to-reported values is also shown in Fig. 38 (right). The computed and reported values for this organ are generally within ±20 percent agreement for all source geometries.

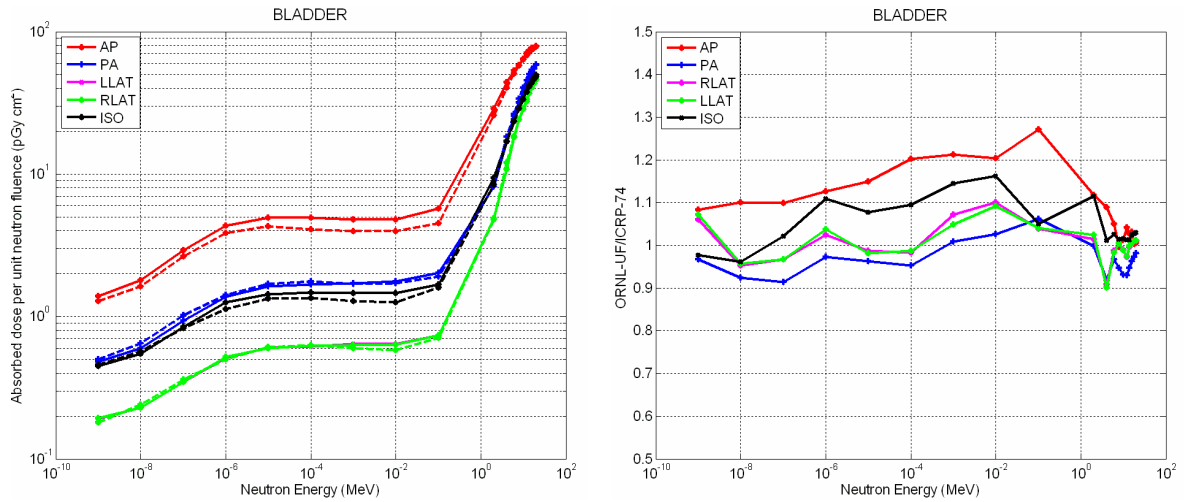

Fig. 38. Bladder absorbed dose per unit neutron fluence for the ORNL-UF model (solid) and ICRP-74 values (dashed). The ratio of computed to ICRP-74 is shown on the right.

3.3.3 Comparison of the Computed Organ Dose Values Using the ORNL-UF and MIRD-5 Phantom Models for Photon Source

As discussed previously, since the values tabulated in ICRP-74 were based on the computational results using different phantom models, nuclear codes, and data, there is a wide spread in the compiled data, especially for some of the organs such as the thyroid and the colon. Since there was a large variety of factors that must be considered in the generation of reported ICRP-74 data (phantom models, codes, and data), a series of benchmark computations using the ORNL-UF and MIRD-5 phantom models was performed using the same radiation transport code, the same nuclear data, and the same computers. These computations were performed to determine the impact of the phantom model change on the computed organ doses. Although both phantom models are hermaphrodites, the organ locations and compositions are different. In these calculations, compared to the tabulated values in ICRP-74, the additional uncertainties due to the nuclear codes and data are eliminated. Therefore, the differences (shown in the following figures) are mainly due to the organ definitions, locations, and compositions.

The ratios of the computed organ dose values for thyroid were shown earlier in Fig. 22, and it was discussed that the reasons behind the large deviations for the PA geometry were due to the differences in the location of the thyroid in these models. The ratios of the computed organ dose values for breast were presented earlier in Fig. 17; it was discussed that the differences in the computed organ dose values are primarily due to the composition change.

The ratios of the computed organ dose values for the ***gonads*** (left) and the ***bone surface*** (right) using the ORNL-UF and MIRD-5 phantom models are shown in Fig. 39. For source energies higher than 0.1 MeV, the computed organ dose values using both phantoms are essentially the same. At lower energies, there are small deviations, both due to the statistical uncertainties and small composition changes in the other organs.

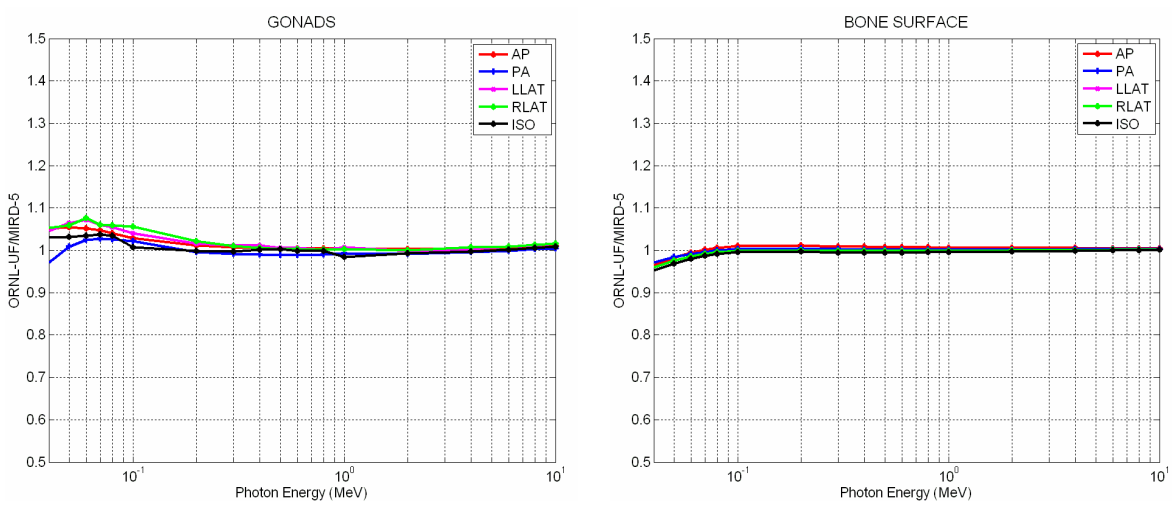

Fig. 39. The ratio of the computed organ dose values to the gonads (left) and bone surface (right) using the ORNL-UF and MIRD-5 phantom models.

The ratios of the computed organ dose values for the ***liver*** (left) and the ***lung*** (right) using the ORNL-UF and MIRD-5 phantom models are shown in Fig. 40. The computed organ dose values to the liver using both phantoms are the same. For lungs, however, there are some discrepancies for RLAT and LLAT geometry. As discussed earlier, this is due to the changes in the lung model in the ORNL-UF phantom model. The MIRD-5 phantom model assumes that the right and left lung are the same, while the ORNL-UF model treats them differently.

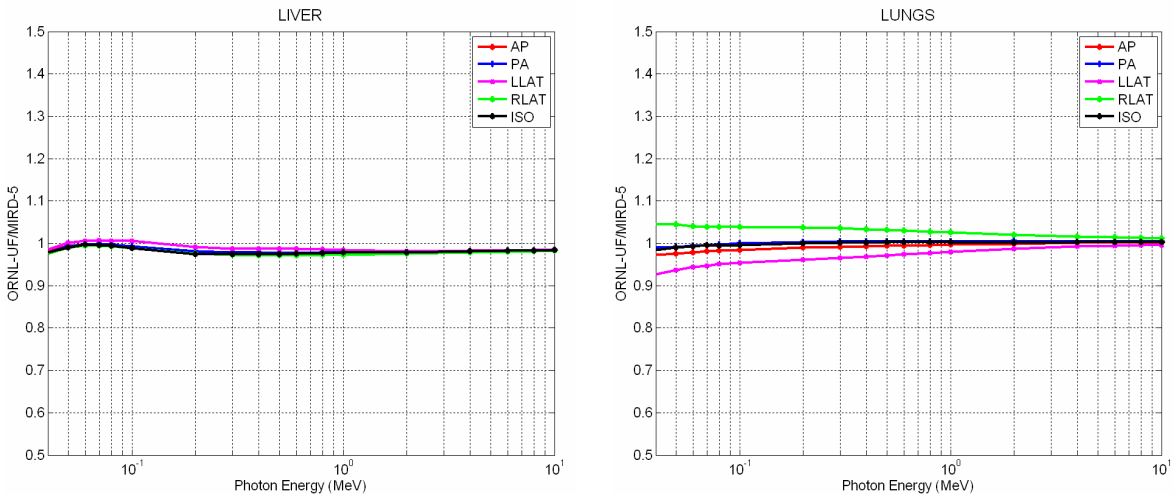

Fig. 40. The ratio of the computed organ dose values to the liver (left) and lungs (right) using the ORNL-UF and MIRD-5 phantom models.

The ratios of the computed organ dose values for the ***stomach*** (left) and the ***colon*** (right) using the ORNL-UF and MIRD-5 phantom models are shown in Fig. 41. The computed organ dose values to the stomach for the ORNL-UF phantom model are 10 percent higher than the MIRD-5 phantom model. For the colon, the computed organ dose values agree with each other except for the RLAT and LLAT geometries, which indicate the locations are different.

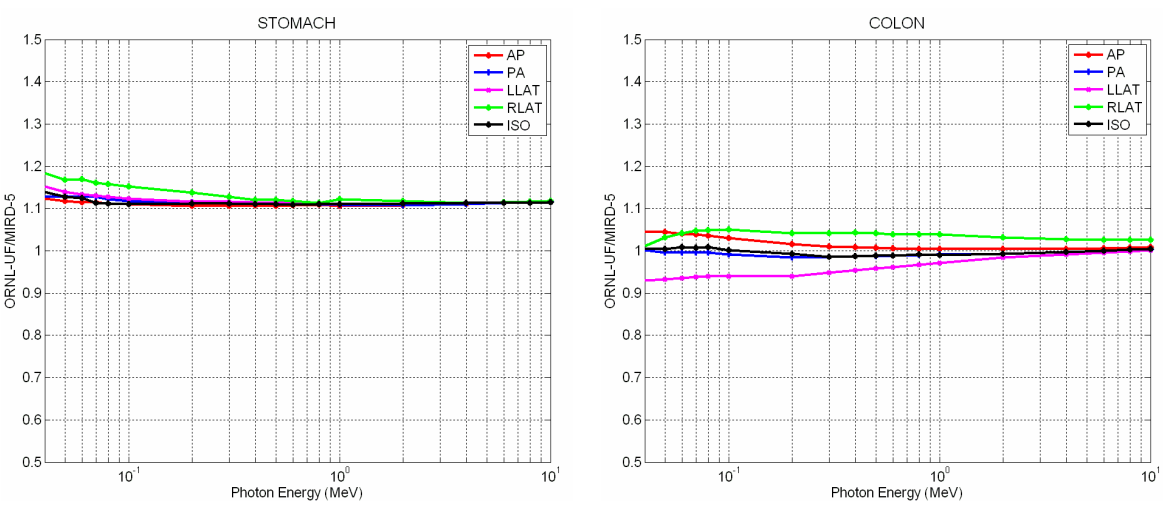

Fig. 41. The ratio of the computed organ dose values to the stomach (left) and colon (right) using the ORNL-UF and MIRD-5 phantom models.

3.3.4 Comparison of the Computed Organ Dose Values Using the ORNL-UF and MIRD-5 Phantom Models for Neutron Source

The ratios of the computed organ dose values for the ***gonads*** (left) and the ***breast*** (right) using the ORNL-UF and MIRD-5 phantom models are shown in Fig. 42. The computed organ dose values to the gonads using both phantom models agree within a few percent for AP, PA, and ISO geometries and within 10 percent for RLAT and LLAT geometries. However, for the breast, there is a more significant difference; as discussed earlier these differences are primarily due to the composition change for this organ in the ORNL-UF model.

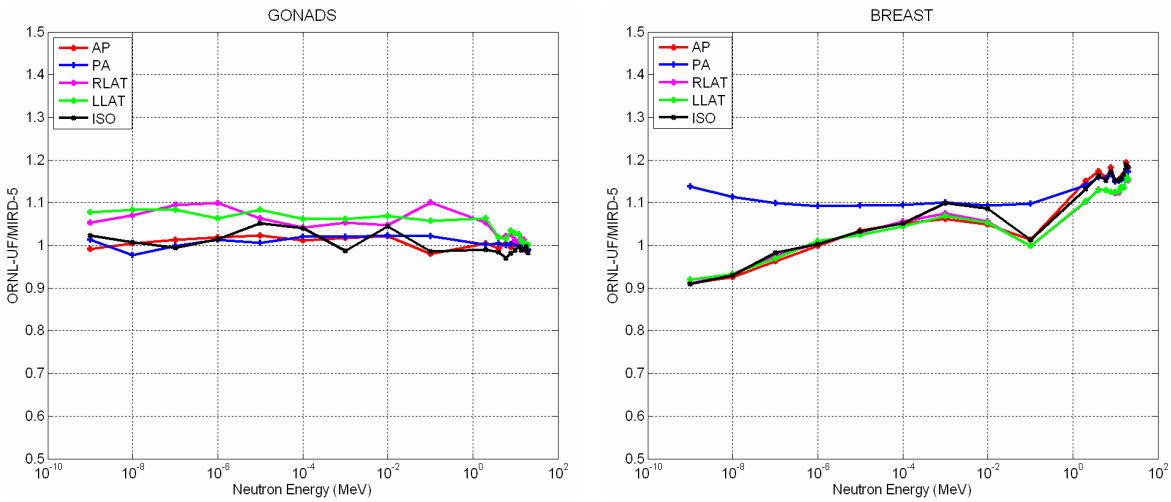

Fig. 42. The ratio of the computed organ dose values to the gonads (left) and breast (right) using the ORNL-UF and MIRD-5 phantom models.

The ratios of the computed organ dose values for the ***bone surface*** (left) and the ***colon*** (right) using the ORNL-UF and MIRD-5 phantom models are shown in Fig. 43. The computed organ dose values to the bone surface are essentially the same using both phantoms. However, for the colon, there are some differences in the computed values, as shown in Fig. 43 (right). These differences are primarily caused by the change in the colon's location and depth in the ORNL-UF model.

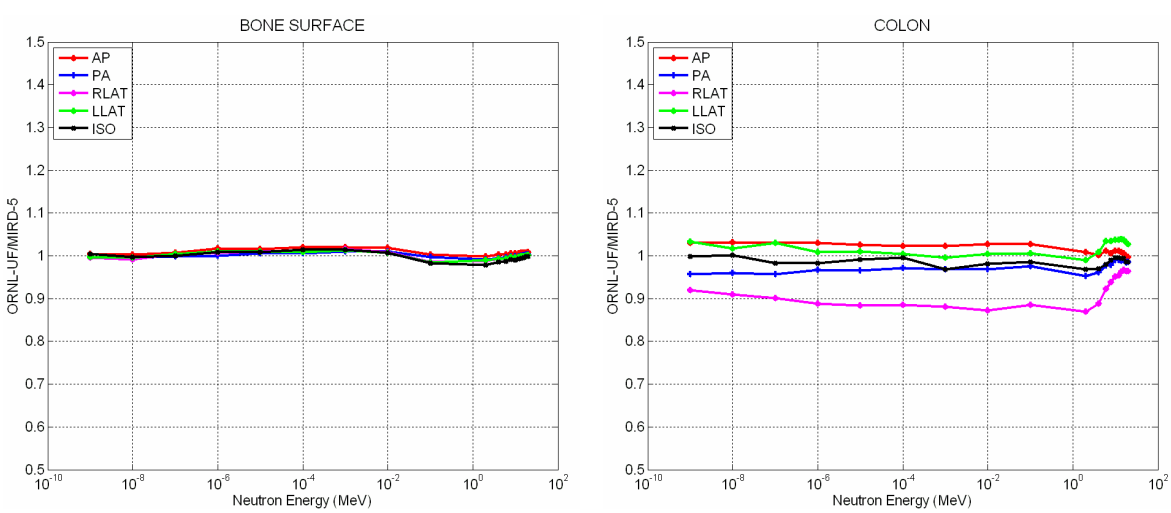

Fig. 43. The ratio of the computed organ dose values to the bone surface (left) and colon (right) using the ORNL-UF and MIRD-5 phantom models.

The ratios of the computed organ dose values for ***liver*** (left) and ***lungs*** (right) using the ORNL-UF and MIRD-5 phantom models are shown in Fig. 44. The organ dose for the liver is almost the same using both phantom models. However, for lungs, there is some difference in the computed values, especially for RLAT and LLAT geometry. As discussed earlier, this is primarily because in the ORNL-UF phantom model, the left lung and right lung have different mass and volume. The MIRD-5 phantom model assumed that the mass and volume of both lungs are identical.

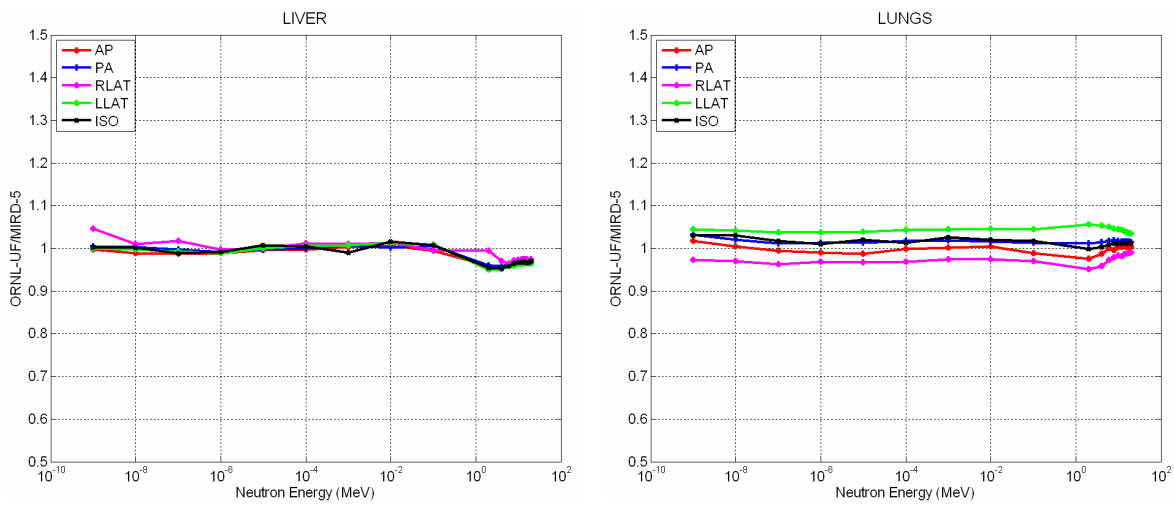

Fig. 44. The ratio of the computed organ dose values to the liver (left) and lungs (right) using the ORNL-UF and MIRD-5 phantom models.

The ratios of the computed organ dose values for ***thyroid*** (left) and ***stomach*** (right) using the ORNL-UF and MIRD-5 phantom models are shown in Fig. 45. As discussed previously, because the ORNL-UF phantom model has a neck, its thyroid location relative to the body surface differs significantly from that of the MIRD-5 phantom, which has no neck. This effect is more clearly observed for the PA geometry as shown in Fig. 45 (left). The absorbed dose to the stomach is 10–15 percent higher using the ORNL-UF model for all source geometries. Similarly, higher dose values with the ORNL-UF model were observed for the photon source, as shown in Fig. 41, in the previous section.

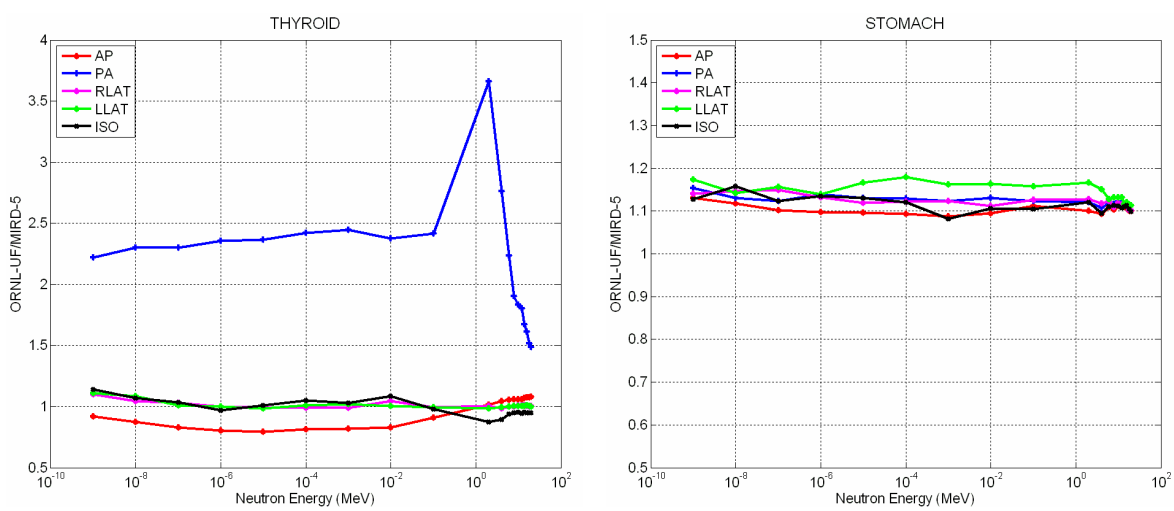

Fig. 45. The ratio of the computed organ dose values to the thyroid (left) and stomach (right) using the ORNL-UF and MIRD-5 phantom models.

3.4 SUMMARY OF THE BENCHMARK CALCULATIONS

A series of Monte Carlo computations was performed for the ORNL-UF model using the standard ICRP irradiation geometries for monoenergetic neutron and photon sources. The computations were performed for 20 neutron energies, ranging from 10^{-9} to 20 MeV, and for 5 different source geometries. Similarly, for the photon source, the computations were performed for 20 source energies, varying from 30 keV to 10 MeV, and for the same 5 source geometries. Therefore, 400 simulations were performed using the ORNL-UF and MIRD-5 models. The source energy values are a subset of the values tabulated in ICRP-74.

It was discussed that the values reported in ICRP-74 were based on the compiled results from previously published values, which were generated using different phantom models, radiation transport codes, and cross-section data. The best fit to these compiled data was tabulated as conversion coefficients. The wide spread in the original data for some of the organs, especially the thyroid and colon, was illustrated using the figures taken directly from the ICRP-74.

Nevertheless, the computational results were benchmarked against the tabulated data in ICRP-74 for both neutron and photon sources. In general, the computed results were within ±10 percent agreement for the photon source and within ±20 percent agreement for the neutron source, except for some of the organs like the thyroid and colon. A wider spread in the computed dose values for neutron sources was observed, primarily because the cross-section sets have significant differences in the neutron data. The ENDF nuclear data have been revised several times in the past decade to improve accuracy.

To determine the impact of the revisions on the computed organ values compared to the MIRD-5 phantom model, a series of calculations (using the same code and nuclear data) for this model was also performed. The computations were performed for the same energies and source irradiation geometries. Hence, 200 more simulations were carried out for this part of the benchmark. The comparison could not be made for organs like the esophagus since the MIRD-5 phantom lacks this organ. The computed organ dose values using the two phantoms are in excellent agreement for some of the organs (e.g., liver and bone surface). However, for some of the organs (e.g., thyroid) the organ dose values differ significantly from each other. Changes in the organ locations were the main reason for these discrepancies.

4. SENSITIVITY ANALYSIS

A series of computations was performed to determine the sensitivity of the computed organ doses to the composition of the organs and to the nuclear data sets (for neutron source). In a sense, the sensitivities to the organ locations and elemental composition were performed in the previous section by comparing results from the MIRD-5 and ORNL-UF phantom models using the same nuclear code and cross-section sets. In this section, the sensitivity to composition and cross sections using the same phantom (ORNL-UF model) will be presented.

4.1 SENSITIVITY TO COMPOSITION

Traditionally, three compositions (lung, bone, and soft tissue) were used to describe all the organs in the mathematical phantoms. Recently, the elemental compositions of the organs were updated according to ICRP-89 standards. Table 2 presents the elemental compositions of the major organs. A series of computations, using the ORNL-UF model, was performed to determine the impact of this composition change on the computed organ dose values, at least for exposure to external radiation. Instead of the previously defined 23 compositions, the ORNL-UF model was modified; the material number for all organs changed to the soft tissue material number, except for bone and lung. The results from this three-composition model are compared in this section to the results using 23 compositions that were presented in the previous section. The computations were performed for the same neutron and photon source energies used in the previous section but only for three of the source geometries (AP, PA, and ISO).

4.1.1 Sensitivity to Composition for Photon Source

The ratios of the computed organ dose to the ***gonads*** (left) and ***bladder*** (right) are shown in Fig. 46. As shown in the figure, above 0.2 MeV, the computed organ dose values are essentially the same. However, at lower energies, the absorbed dose values for both organs are higher (up to 10 percent) when 23 compositions are used.

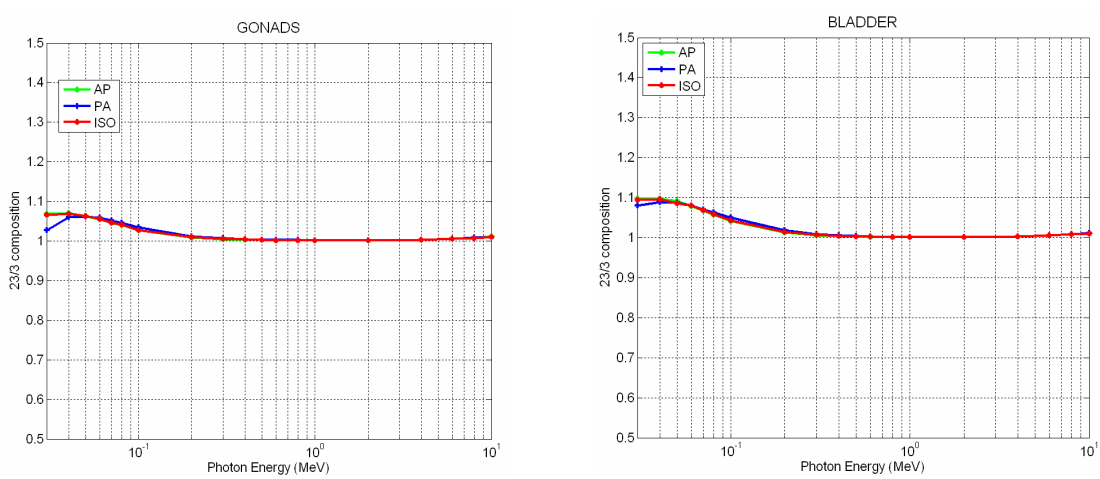

Fig. 46. The ratio of the computed organ doses using 23 and 3 compositions for gonads (left) and bladder (right).

The ratios of the computed organ dose to the ***liver*** (left) and ***colon*** (right) are shown in Fig. 47. Similar to the gonads and bladder, for the liver and colon above 0.2 MeV, the computed organ dose values are the same. However, at low energies, the absorbed dose values for both organs are higher by a small percentage when 23 compositions are used.

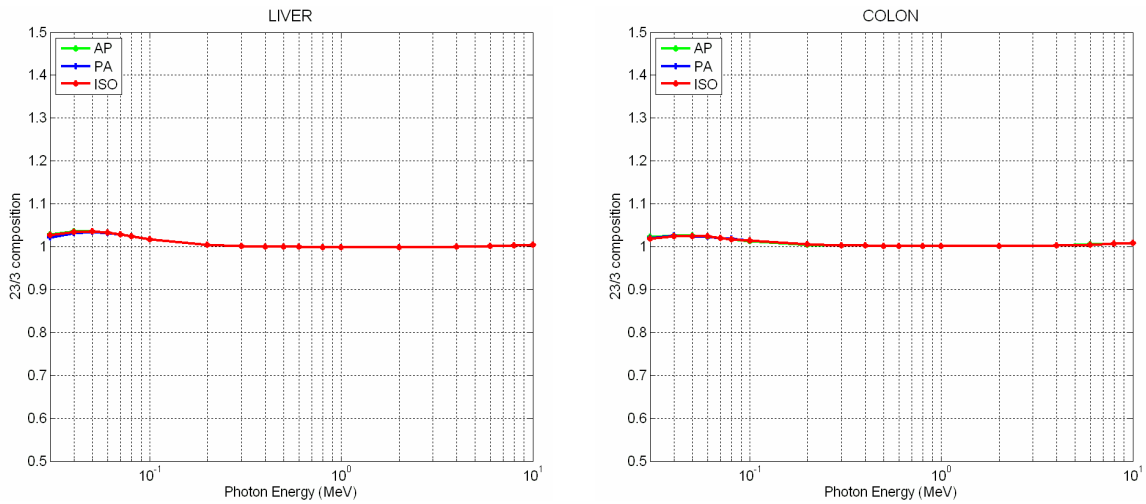

Fig. 47. The ratio of the computed organ doses using 23 and 3 compositions for liver (left) and colon (right).

The ratios of the computed organ dose to the ***stomach*** (left) and ***bone surface*** (right) are shown in Fig. 48. The stomach exhibits behavior similar to the liver and colon. At low energies, the absorbed dose values are higher by only a small percentage when 23 compositions are used. The computed organ dose values for bone surface at low energies (below 50 keV) using 23 compositions are lower; however, this decrease in the computed organ dose is very small. For both organs, above 0.1 MeV, the computed organ dose values are the same for both sets of elemental compositions.

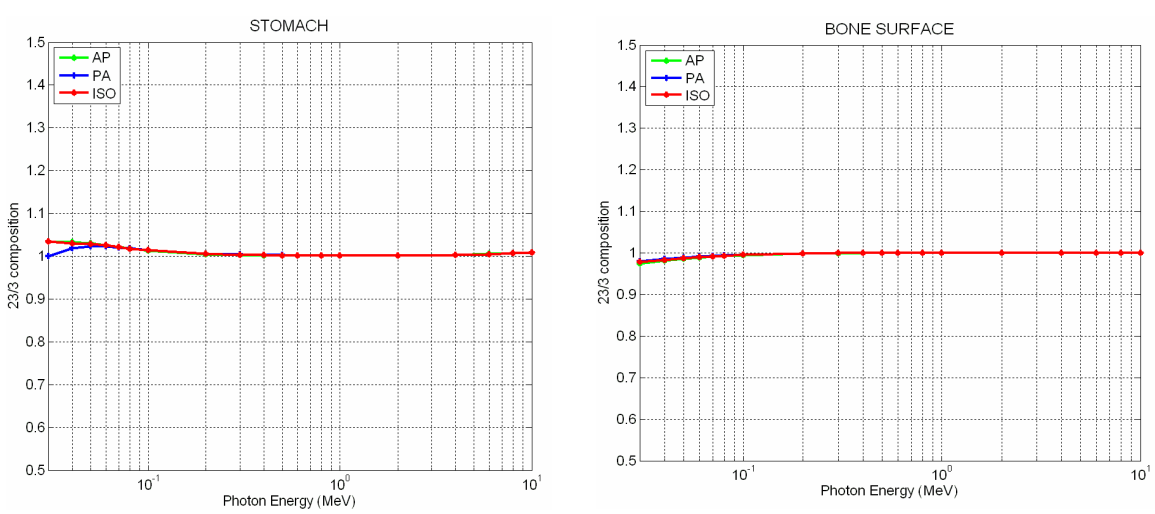

Fig. 48. The ratio of the computed organ doses using 23 and 3 compositions for stomach (left) and bone surface (right).

The ratios of the computed organ dose to the ***esophagus*** (left) and ***thyroid*** (right) are shown in Fig. 49. Except for the thyroid at very low energy (30 keV), there is no statistically significant change in the computed organ dose values for these two organs.

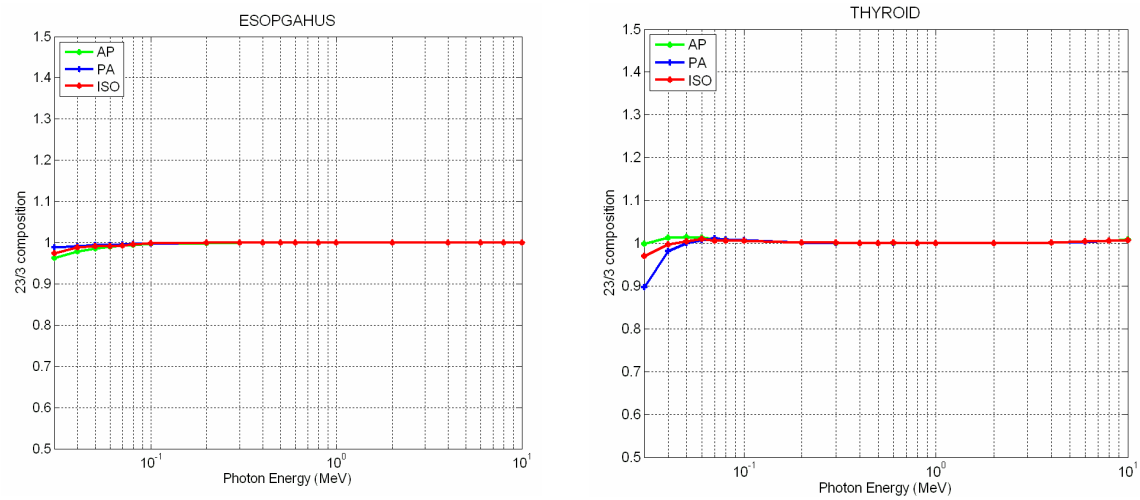

Fig. 49. The ratio of the computed organ doses using 23 and 3 compositions for esophagus (left) and thyroid (right).

The ratios of the computed organ dose to the ***lungs*** (left) and ***skin*** (right) are shown in Fig. 50. As can be seen from the figure, there is no statistically significant change in the computed organ dose values for these two organs, even at low energies.

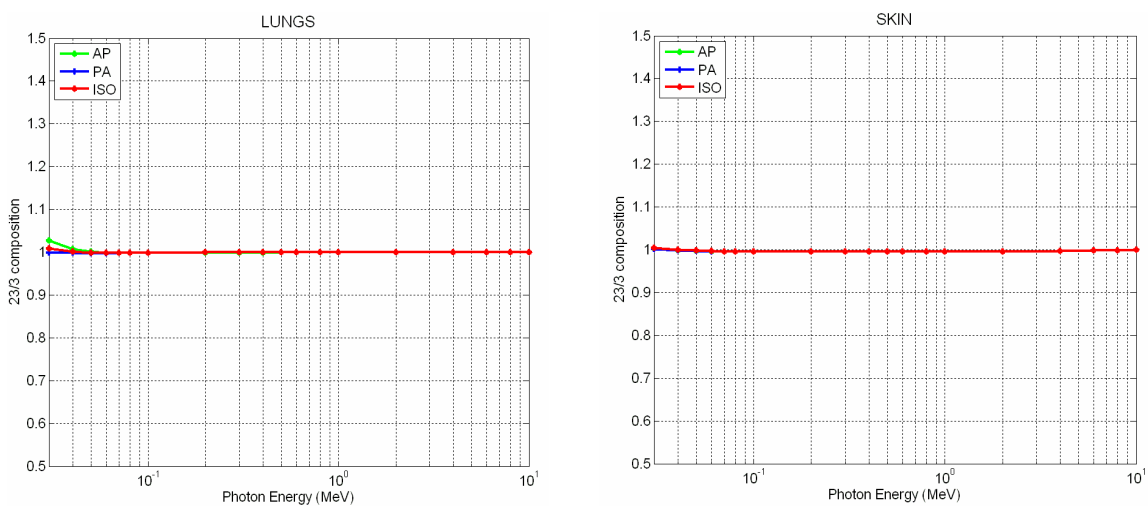

Fig. 50. The ratio of the computed organ doses using 23 and 3 compositions for lungs (left) and skin (right).

The ratio of the computed organ dose to the ***breast*** is shown in Fig. 51. Above 0.2 MeV, there is no statistically significant change in the computed organ dose for the breast. However, at lower energies, for the photon source, the breast showed the maximum sensitivity to the composition. The computed organ dose values are lower with 23 compositions. This is primarily because the largest change in composition, as compared to soft tissue, is for the breast (see Table 2).

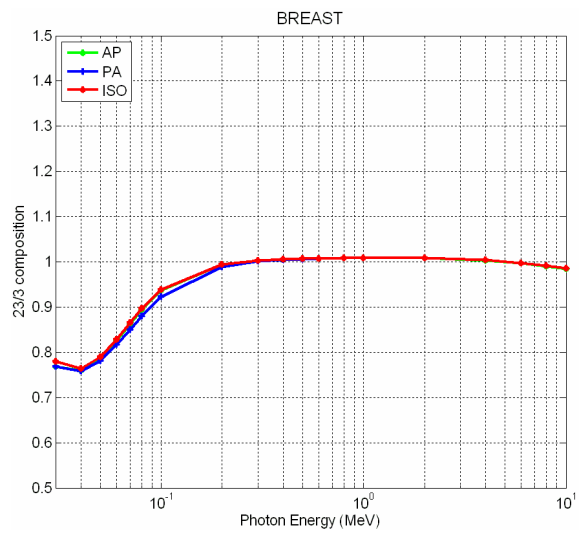

Fig. 51. The ratio of the computed organ doses using 23 and 3 compositions for breast.

4.1.2 Sensitivity to Composition for Neutron Source

The sensitivity analysis results for gonads are included in this section. The analysis was carried out for all organs and similar behavior was observed. The gonad results are included here because they have the highest tissue-weighting factor (0.2). The only two exceptions to this behavior, no effect on total organ dose, were the breast and skin. The results for the breast are discussed separately below. The breast and skin show similar behavior.

Since the source is neutrons, the total dose includes the dose due to neutrons and contributions from photons generated via neutron interactions. In this analysis, in addition to total dose, the neutron and photon dose values were tallied separately to determine the impact of composition on these doses independently.

The ratio of the computed organ dose to the ***gonads*** using 23 and 3 compositions is shown in Fig. 52. In this figure, the ratio of the total (neutron and photon) dose is shown on the left, the dose due to neutrons only is shown in the middle, and the photon dose is shown on the right. There is no statistically significant change in the total dose to the gonads with elemental composition change. However, the neutron dose is affected by the composition change, especially below 1 MeV. The change in organ dose due to neutrons is up to 25 percent for AP and ISO source geometries. Above 1 MeV, there is no statistically significant change in the organ dose values. The change in the photon dose is negligible.

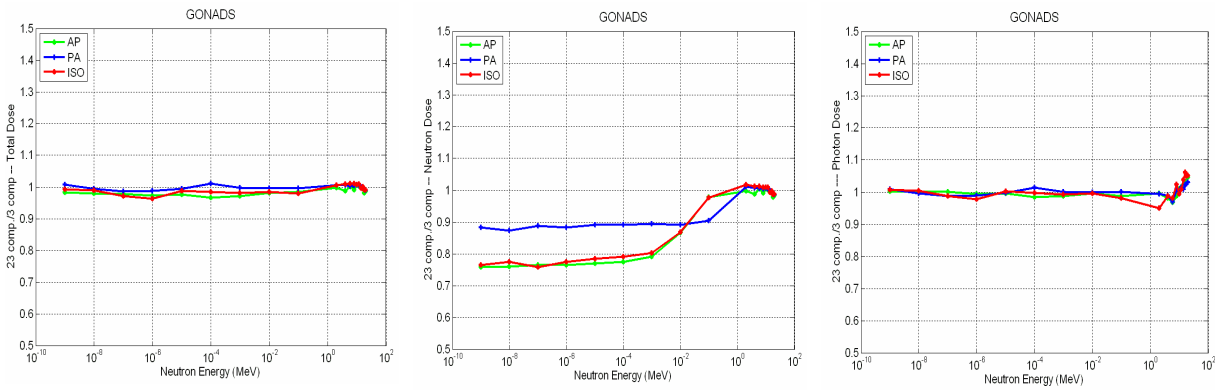

Fig. 52. The ratio of the total (left), neutron (middle), and photon (right) computed organ doses using 23 and 3 compositions for gonads.

While there is significant change in the neutron dose, this change is not apparent in the total dose. The reason for this can be understood when the neutron-to-total and photon-to-total dose ratios are taken into account. At low energies, mainly capture reactions occur, which results in the emission of gammas [largely the H(n,γ) reaction yields a 2.2246 MeV photon]. The neutron-to-total (left) and photon-to-total (right) absorbed dose contributions are shown in Fig. 53. As shown in the figure, at low energies, photons are the primary contributor to the absorbed dose; greater than 90 percent. Therefore, the changes in the neutron dose at low energies are negligible compared to the total dose. At higher energies, when the contribution from photon dose is reduced, there is no change in the computed organ dose due to neutrons.

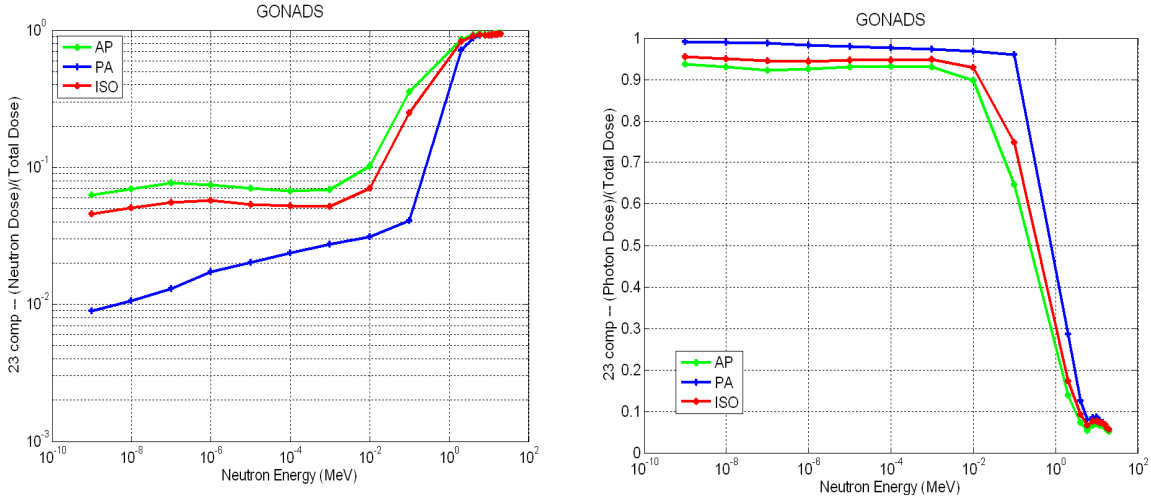

Fig. 53. The ratio of the neutron (left) and photon (right) dose to the total (neutron and photon) dose for gonads.

The ratios of the total (left), neutron (middle), and photon (right) organ dose to the breast using 23 and 3 compositions are shown in Fig. 54. In this figure, the ratio of the total (neutron and photon) dose is shown on the left, the dose due to neutrons only is shown in the middle, and the photon dose is shown on the right. For the breast, the total dose is sensitive to the composition change, especially for AP and ISO geometries. Below 0.1 MeV, the total dose is lower (up to 12 percent) for AP and ISO geometry when 23 compositions are used. For PA geometry, at lower energies, there is no statistically significant change. For energies above 1 MeV, the total dose is consistently 10 percent higher for all geometries. As shown in the figure, the neutron dose changes significantly at lower energies, whereas the photon dose remains the same.

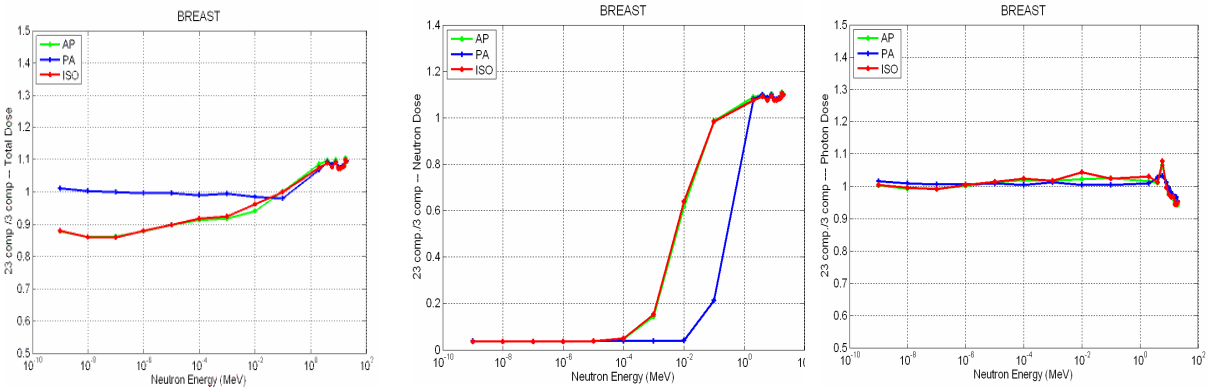

Fig. 54. The ratio of the total (left), neutron (middle), and photon (right) computed organ doses using 23 and 3 compositions for breast.

The neutron-to-total (left) and photon-to-total (right) absorbed dose contributions are shown in Fig. 55. This significant change in the neutron dose impacts the total dose even though the neutron-to-total dose values are still relatively low, as shown in Fig. 55 on the left. Although below 1 MeV, the contribution to the total dose is mainly from photons, above 1 MeV, there is significant reduction in photon-to-total dose ratio.

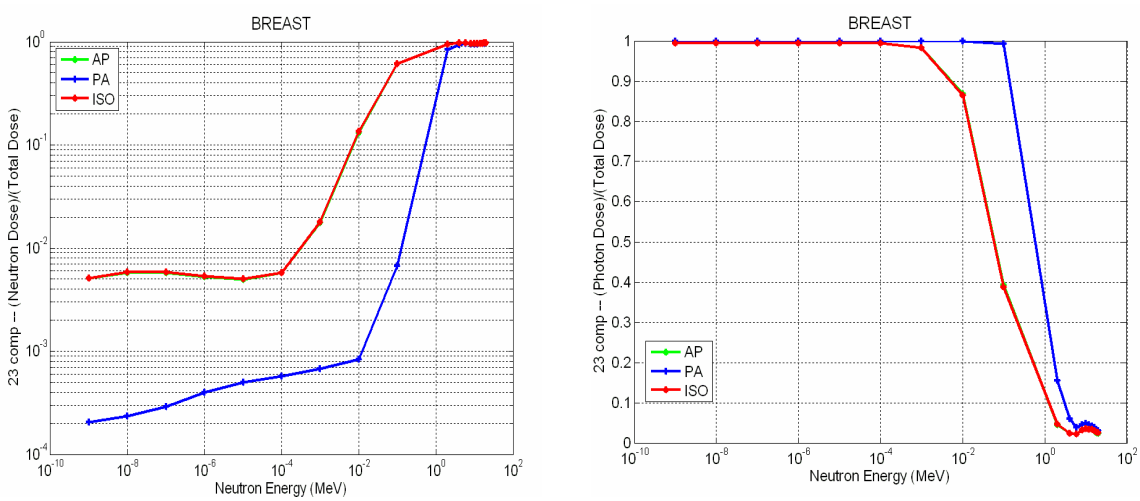

Fig. 55. The ratio of the neutron (left) and photon (right) dose to the total (neutron and photon) dose for breast.

4.2 SENSITIVITY TO CROSS SECTIONS

As discussed in the previous section, the tabulated values in ICRP-74 were based on the compilation of data from different institutes using different phantom models, radiation transport codes, and nuclear data. The agreement between the computed data using the ORNL-UF phantom model, using the MCNP5 with ENDF/B-VI.6 data, and the tabulated ICRP-74 data for neutron sources was generally within 20 percent. The computational results using the ORNL-UF model were benchmarked against the MIRD-5 phantom model using the same code and cross sections. The sensitivity to composition was investigated, and the analysis showed that the tissue elemental composition has a negligible effect on the computed organ doses except for the breast and skin. Therefore, the differences in the computed organ values between the ORNL-UF model and the MIRD-5 phantom model (less than 10 percent, except for thyroid) can be attributed to the differences in the phantom models (organ locations and definitions).

The reasons behind the larger discrepancies between the tabulated ICRP-74 data and the computed values using the ORNL-UF model were investigated further. Since the publication of ICRP-74 in 1996, the neutron cross sections have been updated several times to improve the accuracy. Therefore, a series of benchmark computations using different cross-section sets with the same phantom model has been performed. The tabulated data in ICRP-74 was mainly based on the computations performed using ENDF/B-IV and ENDF/B-V. Since the ENDF/B-IV data is no longer distributed with MCNP, the sensitivity computations were performed using ENDF/B-V and ENDF/B-VI.0 nuclear data sets. The computational results reported in the previous sections were based on the ENDF/B-VI.6 nuclear data set. Therefore, the computed organ doses for these three different nuclear data sets are compared and the results are presented in this section.

The ratios of the computed organ dose values for the ***gonads*** (left) and ***colon*** (right) using the three different data sets for three irradiation geometries (AP, PA, and ISO) are shown in Fig. 56. The ratios of the ENDF/B-V to ENDF/B-VI.6 ratios are shown with solid lines, while the ENDF/B-VI.0 to ENDF/B-VI.6 ratios are shown with dashed lines. As shown in the figure, there is no statistically significant difference between the computed organ dose values using the ENDF/B-VI.0 and ENDF/B-VI.6. However, there is up to 10 percent difference in the computed organ dose values using the ENDF/B-V nuclear data set, as compared to ENDF/B-VI.6 or ENDF/B-VI.0, for both organs below 1 MeV. The differences in organ dose values between the data sets vary with the source energy and geometry. For energies above 1 MeV, the differences in the computed values using all three sets are very small.

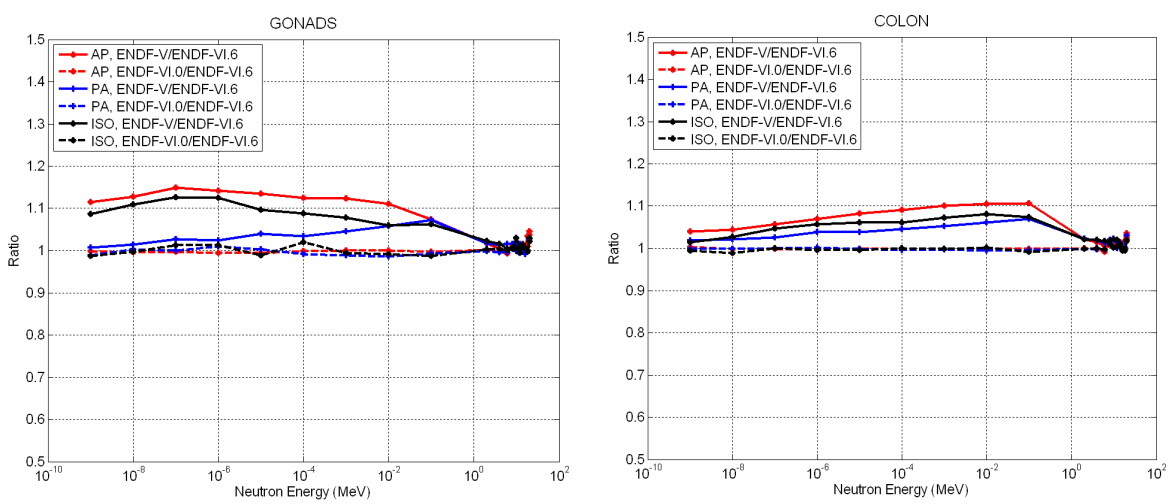

Fig. 56. The ratio of the computed organ dose values using ENDF/B-V, ENDF/B-VI.0, and ENDF/B-VI.6 nuclear data sets for gonads (left) and colon (right).

The ratios of the computed organ dose values for the ***thyroid*** (left) and ***esophagus*** (right) using the three different data sets are shown in Fig. 57. The ENDF/B-V to ENDF/B-VI.6 ratios are shown with solid lines, while the ENDF/B-VI.0 to ENDF/B-VI.6 ratios are shown with dashed lines. As can be seen from the figure, there is no statistically significant difference in the organ dose values computed with the ENDF/B-VI.0 and ENDF/B-VI.6. However, as clear from the figure, the differences in the computed organ values using the ENDF/B-V nuclear data set, as compared to ENDF/B-VI.6 or ENDF/B-VI.0, are up to 20 percent for the thyroid and up to 10 percent for the esophagus below 1 MeV. The differences in organ dose values between the data sets vary with the source energy and geometry. For energies above 1 MeV, the differences in the computed values using all three sets are small.

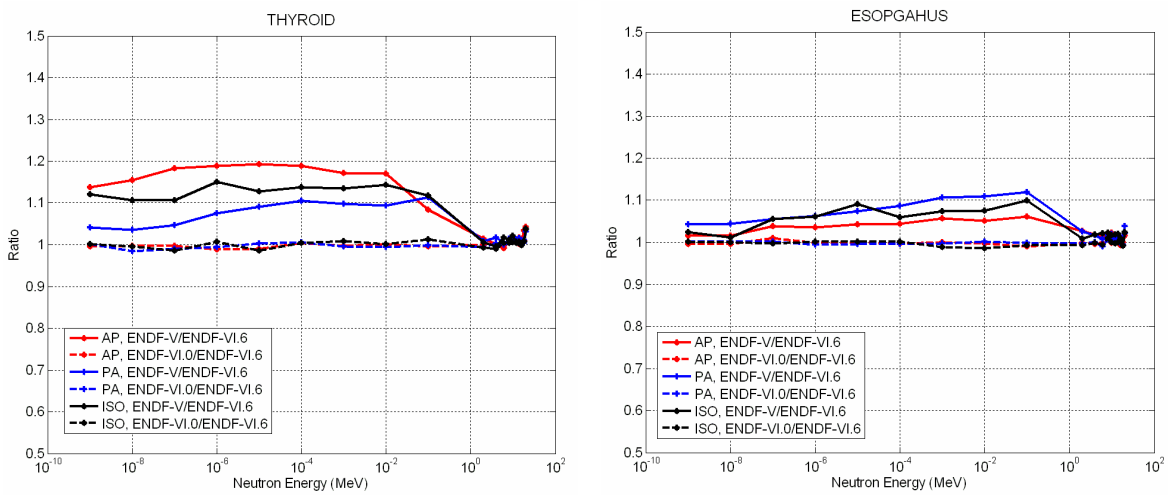

Fig. 57. The ratio of the computed organ dose values using ENDF/B-V, ENDF/B-VI.0, and ENDF/B-VI.6 nuclear data sets for thyroid (left) and esophagus (right).

The ratios of the computed organ dose values for the ***liver*** (left) and ***stomach*** (right) using the three different data sets are shown in Fig. 58. The ENDF/B-V to ENDF/B-VI.6 ratios are shown with solid lines, while the ENDF/B-VI.0 to ENDF/B-VI.6 ratios are shown with dashed lines. There is no statistically significant difference in the computed organ dose values using ENDF/B-VI.0 or ENDF/B-VI.6 for these organs as well. However, as clear from the figure, the differences in the computed organ values using the ENDF/B-V nuclear data set, as compared to ENDF/B-VI.6 or ENDF/B-VI.0, are up to 12 percent for the liver and up to 15 percent for the stomach below 1 MeV. For energies above 1 MeV, the differences in the computed values using all three sets are small, as shown in Fig. 58.

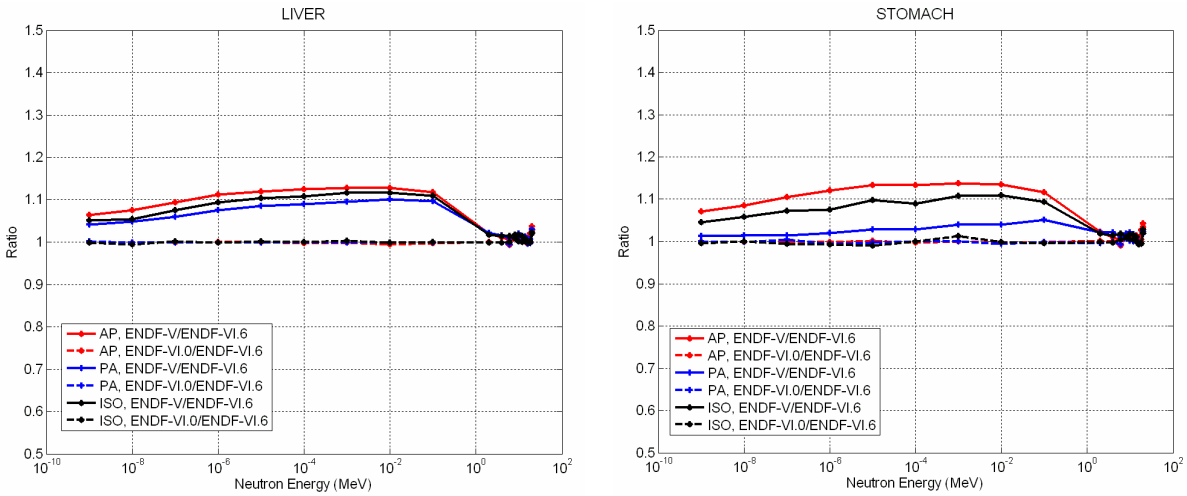

Fig. 58. The ratio of the computed organ dose values using ENDF/B-V, ENDF/B-VI.0, and ENDF/B-VI.6 nuclear data sets for liver (left) and stomach (right).

The ratios of the computed organ dose values for the ***bladder*** (left) and ***bone surface*** (right) using the three different data sets are shown in Fig. 59. The ENDF/B-V to ENDF/B-VI.6 ratios are shown with solid lines, while the ENDF/B-VI.0 to ENDF/B-VI.6 ratios are shown with dashed lines. There is no statistically significant difference in the computed organ dose values using ENDF/B-VI.0 or ENDF/B-VI.6 for these organs. However, as the figure shows, the differences in the computed organ values using the ENDF/B-V nuclear data set, as compared to ENDF/B-VI.6 or ENDF/B-VI.0, are up to 20 percent for the bladder and up to 10 percent for the bone surface below 1 MeV. For energies above 1 MeV, the differences in the computed values using all three sets are small. The differences in organ dose values between the data sets vary with the source energy and geometry for the bladder. However, for bone surface, the organ dose values show the same behavior, independent of the source geometry, since bones are distributed symmetrically in the phantom model.

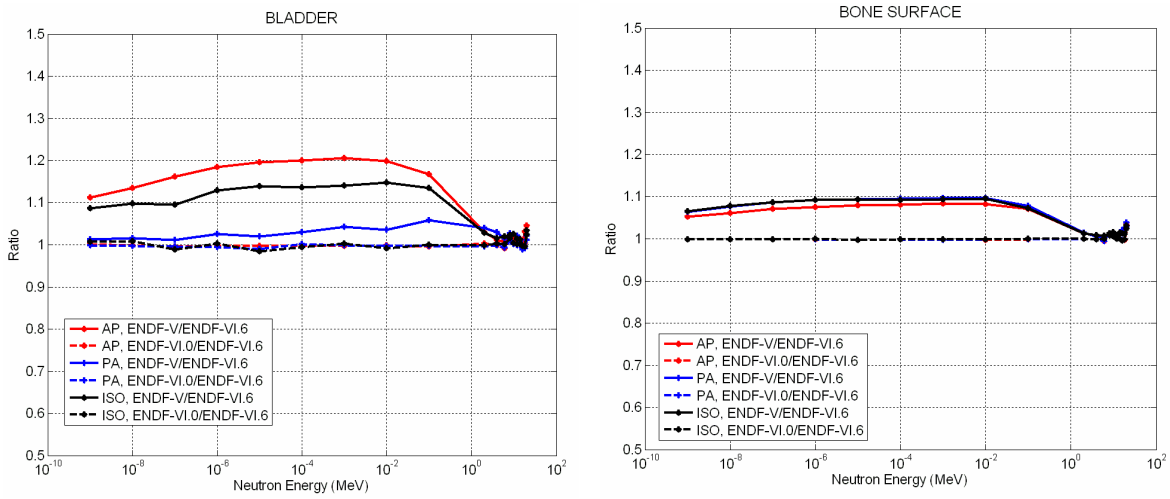

Fig. 59. The ratio of the computed organ dose values using ENDF/B-V, ENDF/B-VI.0, and ENDF/B-VI.6 nuclear data sets for bladder (left) and bone surface (right).

4.3 SUMMARY OF THE SENSITIVITY CALCULATIONS

In this section, additional benchmark computational results are presented. These benchmark computations were performed to understand the reasons behind the discrepancies with the tabulated ICRP-74 values. Furthermore, the computations were performed to determine the sensitivity of the computed organ dose values to composition and nuclear data. The calculations performed in this section represent a benchmark in a truer sense because the same phantom model and the same radiation transport code were used to estimate the organ doses while changing only one set of parameters.

As discussed before, the number of elemental compositions increased to 23 in the ORNL-UF phantom model. Since traditionally only three compositions were used to describe all the organs/tissues in the phantom model, the impact of varying compositions on the computed organ doses was evaluated by repeating the same computations for the ORNL-UF phantom model using only three compositions.

For photon sources, there was no statistically significant change in the computed organ dose values for source energies higher than 0.2 MeV. The computed organ dose values were the same whether 23 or 3 compositions were used to describe the tissues. For source energies lower than 0.2 MeV, for some of the organs—bone surface, lungs, skin, esophagus, thyroid—again there was no statistically significant effect on the computed organ dose values. For other organs—gonad, bladder, liver, colon, stomach—at lower energies, the differences in the computed organ dose values varied from 2 to 10 percent.

For neutron sources, there was no statistically significant change at all in the computed total organ dose values for all organs, except for the breast and skin. Since the source is neutron, in addition to the neutron dose, the dose due to the photons generated via neutron interactions was taken into account. The total dose represents the dose due to both neutrons and photons. When the neutron and photon dose values were analyzed separately, there was a 10 to 25 percent change in the dose due to neutrons at lower neutron energies. However, at these energies, the dose due to photons was significantly larger than the dose due to neutrons. Therefore, the changes in the total dose were unaffected by the changes in the neutron dose alone. For the breast, the change in neutron dose was more clear, up to 90 percent; subsequently, there was an approximately 20 percent change in the total dose for energies lower than 1 MeV.

The sensitivity to neutron cross-section data was investigated using the ORNL-UF phantom model. The computational benchmark results presented in the previous section were performed using the ENDF/B-VI.6 nuclear data set. In this section, the computational results using ENDF/B-V and ENDF/B-VI.0 were compared to the results with ENDF/B-VI.6. The computational results with ENDF/B-VI.0 and ENDF/B-VI.6 were the same. However, the computational results with ENDF/B-V showed up to a 10 to 20 percent change in the organ dose values. Since the tabulated data reported in ICRP-74 is based on the computations using ENDF/B-IV and ENDF/B-V, some of the discrepancies in the benchmark results can be attributed to the differences in the nuclear data set.

5. PIMAL: PHANTOM WITH MOVING ARMS AND LEGS

Although the computational phantom models have been revised constantly over the past two decades, the revisions were mostly done for the internal organs (in terms of number, organ size and location, and elemental composition). The exterior shape of the mathematical phantom (i.e., arms and legs) has remained the same with a few exceptions, which will be discussed below. Furthermore, the computational phantoms have almost always been in the vertical-upright position, with arms attached to the torso as well as rigid arm and leg structure, which does not allow movement or bending. In some cases, especially in occupational exposure, different positioning of the arms and legs is needed for the assessment of the organ doses.

In a few instances, computational phantoms for posture other than vertical-upright have been used to assess radiation dose. For example, to evaluate the organ doses for the A-bomb survivors, a phantom in a sitting position was used.[10] Similarly, for the evaluation of organ doses for a worker seated in a chair, the leg model was revised.[11] The shape of the phantom's upper trunk was modified in simulating thyroid counters.[16] In these cases, the arms were still part of the torso. For the evaluation of the JCO criticality accident, arms and legs were separated.[12] To our knowledge, in all the previous work, the phantom was revised specifically for the case at hand; freely moving arms and legs were not among the options for the phantom.

To model different exposure geometries more easily, a computational phantom with moving arms and legs, based on the ORNL-UF phantom,[3,7] has been developed. The revised phantom model is called **PIMAL**: **P**hantom w**I**th **M**oving **A**rms and **L**egs.[17,18] In this section, the PIMAL model will be presented.

5.1 DESCRIPTION OF PIMAL

Starting with the ORNL-UF phantom model, the arms were separated from the torso and divided into parts that are connected at the shoulder and elbow. Similarly, the legs were reshaped and divided into parts that are connected at the hip and knee. Therefore, in PIMAL, the arms can bend from the shoulder and elbow; legs can bend at the hip and knee.

Currently, there is no capability for the torso to bend with a repositioning of the internal organs. However, for the torso, the assessment of organ doses in different postures can be done by changing or rotating the source location relative to the torso.

The ORNL-UF phantom (left) and PIMAL (right) are shown in Fig. 60. For the arm and leg modeling, the macrobodies feature of the MCNP was used. The arms and legs were separated into parts, modeled using cones; spheres were used for the joints. During the phantom's modification, the original volumes and masses of the arms and legs were retained.

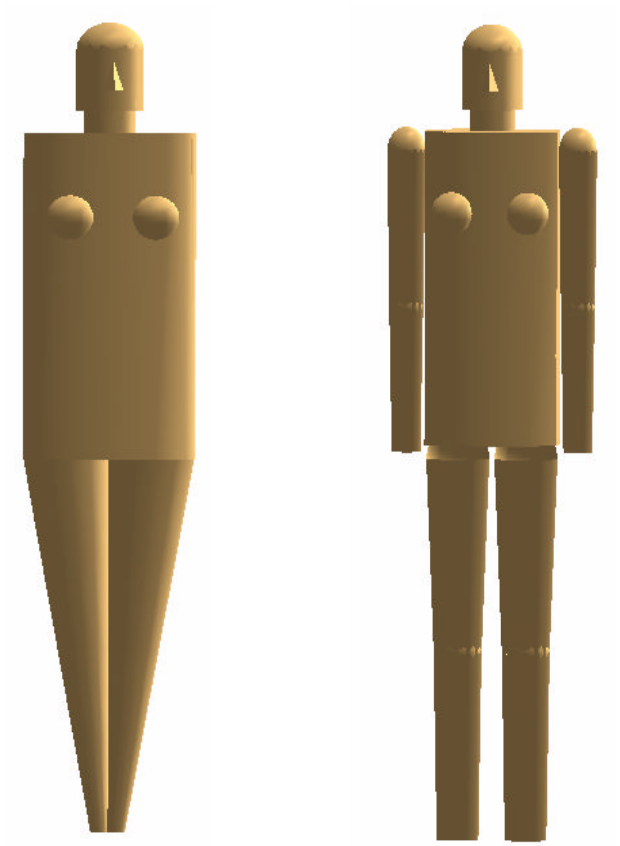

Fig. 60. The ORNL-UF phantom model in the vertical-upright position with arms attached to torso and rigid legs (left) and PIMAL (right).

The internal organs, after skin and soft tissue are removed, for the ORNL-UF phantom (left) and the PIMAL (right) are shown in Fig. 61. Similarly, the arm and leg bones were separated into parts, modeled using cones; joints were modeled with spheres.

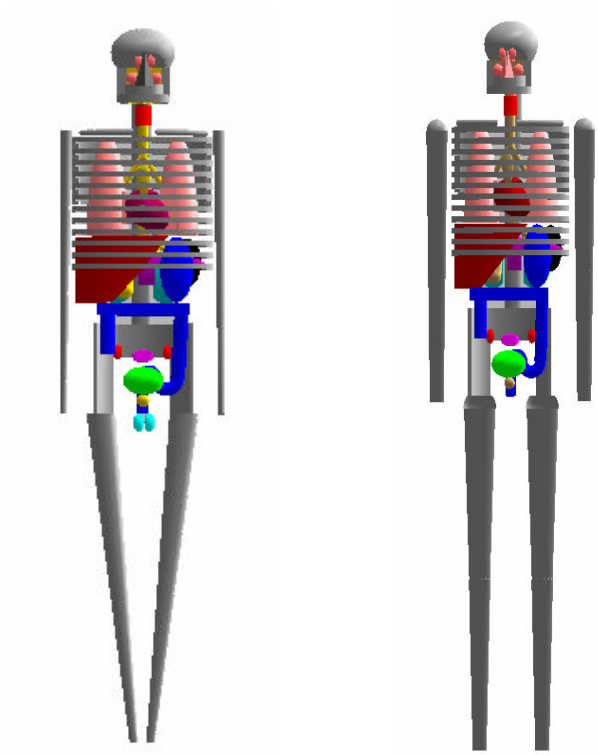

Fig. 61. Interior shape, after skin and soft tissue are removed, of the ORNL-UF (left) and PIMAL (right) models.

To generate a model with the desired arm and leg position, the surface cards in the MCNP were recalculated for the given angles using trigonometric functions. Two illustrative postures generated using this approach are shown in Fig. 62. In the first configuration, the phantom is walking with one of the arms in the front (left). In the second configuration, it is assumed that the phantom is seated in a chair and the arms are on the armrests (right).

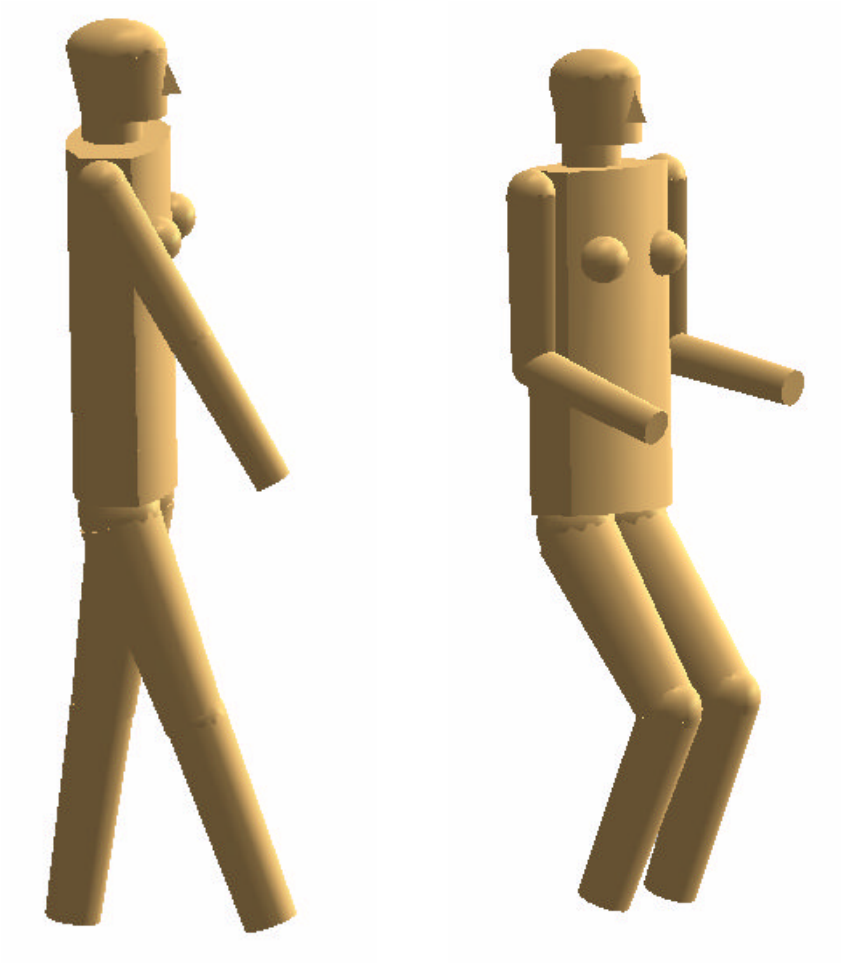

Fig. 62. The phantom is walking with one of the arms in the front (left) and sitting on a chair with the arms on armrest (right).

The phantom model could have been revised further to make the shapes of the arms and legs more realistic; however, the objective of this study was to ensure there was no statistically significant change in the computed organ dose values using the PIMAL compared to the ORNL-UF phantom model for the same vertical-upright position.

5.2 BENCHMARK COMPUTATIONS

To ensure there is no statistically significant change in the computed organ dose values for PIMAL, as compared to computed organ dose values for the ORNL-UF phantom model, a series of benchmark calculations was performed. These benchmark computations were performed for the ORNL-UF phantom model and PIMAL for the same vertical-upright position. The computational results for some of the major organs are presented below.

The ratios of the computed organ dose to the ***gonads*** (left) and ***breast*** (right) using the ORNL-UF phantom model and PIMAL are shown in Fig. 63. It is important to note that ***in all the figures presented in the previous sections, the range for the y axis was from 0.5 to 1.5 with few exceptions (in which the range of the y axis needed to be increased, up to 4 for the thyroid). In this figure, the range for the y axis is from 0.9 to 1.1***. As shown in the figure, the differences in the computed organ dose values are within ±2 percent for both the gonads and breast.

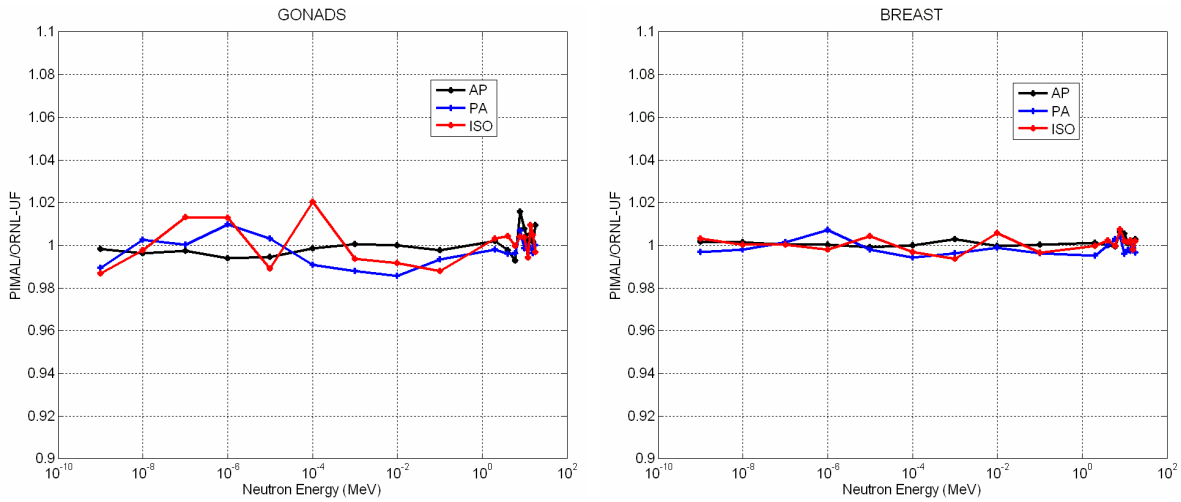

Fig. 63. The ratio of the computed organ doses using ORNL-UF and PIMAL models for gonads (left) and breast (right).

The ratios of the computed organ dose values to the ***lungs*** (left) and ***thyroid*** (right) using the ORNL-UF and PIMAL models are shown in Fig. 64. As shown in the figure, the differences in the computed organ dose values are within ±2 percent for both the lungs and the thyroid.

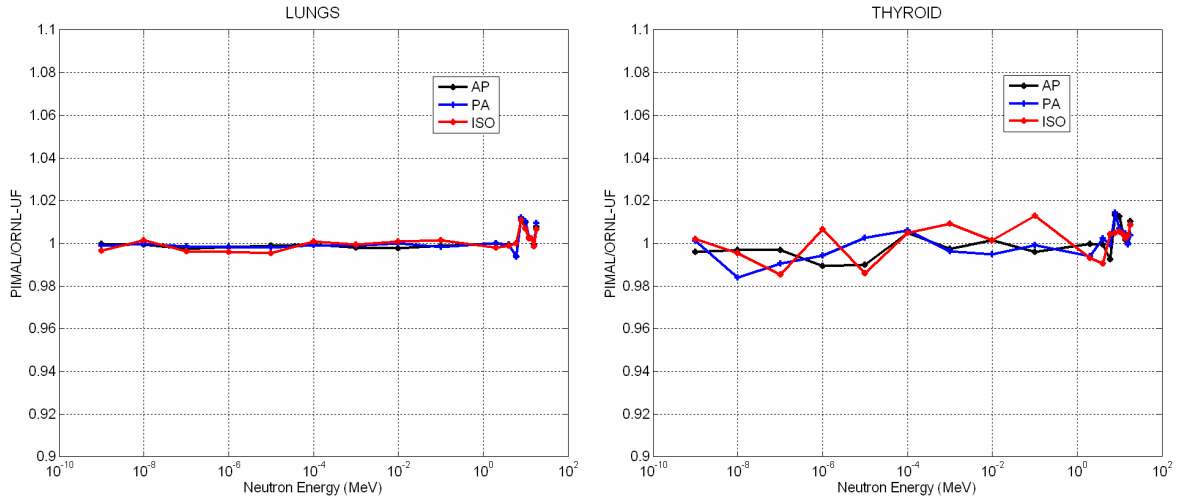

Fig. 64. The ratio of the computed organ doses using the ORNL-UF and PIMAL models for lungs (left) and thyroid (right).

Although the results are not presented here, since they all show a similar behavior, the analysis was carried out for all the organs. Based on the computational results, the ratio of the computed organ dose values varies by only a small percentage for all organs using PIMAL compared to the ORNL-UF phantom model, and these differences are not statistically significant.

6. GRAPHICAL USER INTERFACE FOR PIMAL

In the previous section, PIMAL was described. While the user can recalculate the surface cards for any specified movement using the corresponding angles and enter these values in the input file, a basic interface with a visualization tool can simplify the process and reduce the time it takes to generate the input file for the desired arm and leg positions. This time can be further reduced by a tool that performs the necessary computations—extracts and displays the relevant data from the output file (organ dose values for the assessment of radiation dose). For this purpose, a graphical user interface (GUI) for PIMAL has been developed.[19] The main features of the GUI are described in the following sections.

6.1 DESCRIPTION OF THE GUI

The GUI is written in Java[20] using Java3d features.[21-22] To run the GUI, three programs are needed: (1) Java3d routines (java3d version 1.5 and above), which can be downloaded from the world wide web; (2) Java Run time environment; and (3) MCNP5 code for the radiation transport simulations. MCNP5 can be obtained from the Radiation Safety Information Computational Center (RSICC). If changes to the GUI are desired, then a build system, such as Ant, is needed. Ant can be downloaded free from the world wide web as well.

Since the GUI is coded in Java, it is operating-system independent and can, therefore, be run on Windows, Linux, UNIX, and other platforms. For a Windows environment, an installation program (setup.exe) is included. The installation program includes the executable file (pimal.jar), the required java3d routines, and the Ant build system, which can be used for the compilation when needed. The self-extracting, installation program will create a folder named "Pimal" on the hard disk and will create a shortcut on the desktop with the PIMAL icon. For other operating systems, the user needs to download and install the Java Run time environment and Java3d (both are free) from the world wide web and modify the path accordingly.

6.1.1 GUI Layout and Moving Arms and Legs

The layout of the GUI is shown in Fig. 65. The phantom is on the left and sliding bars are on the right. There are two slider bars for each direction of rotation, movement along sides (θ), and movement from front to back (ϕ). With these sliders, the user can rotate the arms and legs while visualizing the movement.** As described in the previous section, the arms can bend at the shoulder and elbow, and legs bend at the hips and knee. The phantom can be rotated for viewing from different directions. The phantom can be returned to the default position (vertical-upright) by the "**Reset**" button.

The eyes are placed on the phantom to distinguish the front and back of the phantom. The torso of the phantom in the GUI is described by an elliptic cylinder, the arms and legs by cones with spheres at the joints, the neck by a cylinder, and the head by a cylinder capped with a half ellipse. The exterior dimensions of the phantom in the GUI are similar to the dimensions of the phantom used in the MCNP input file. This feature is useful to avoid any surface crossings, hence to avoid geometry errors (i.e., there is no restriction on the movements; however, if the arms or legs cross the torso in the GUI, then this would cause geometry errors in the generated MCNP input file, and the simulation will be terminated due to geometry errors). While the phantom model in the GUI display is only its exterior surface, the phantom model in the MCNP input file contains all the internal organs.

**This interface is based on the simple tool found in Ref. 20. This model has been revised and improved to allow the addition of the desired features. The initial revisions were made by Aaron Fleckenstein while a summer intern at ORNL. The coding was further modified and completed by Dorothea Wiarda of ORNL.

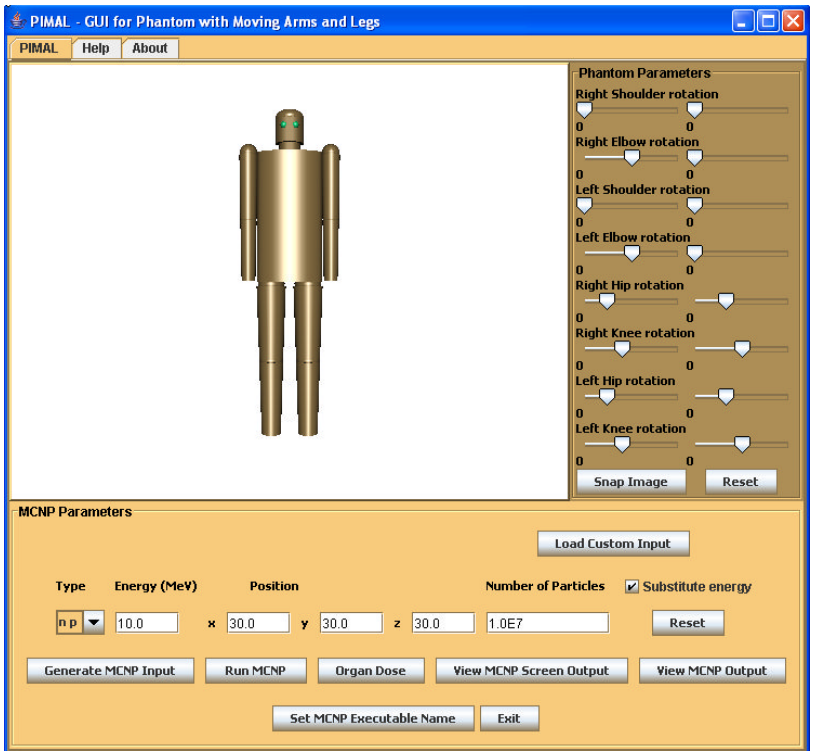

Fig. 65. The layout of the GUI for PIMAL.

6.1.2 Snap Image

The user can save an image of the phantom, along with the angles defining the position of the arms and legs, using the "**Snap Image**" button as shown in Fig. 65. This image can be saved as a JPEG file. A snapshot of an image generated with the GUI is shown in Fig. 66 on the left. This feature is useful especially when the user wants to compare the posture separately using the generated MCNP input file with a visualization tool (e.g., VISED[23] or MORITZ[24]) to ensure they are the same. The generated MCNP input file for the configuration shown in this figure was plotted using MORITZ, and the image is shown on the right.

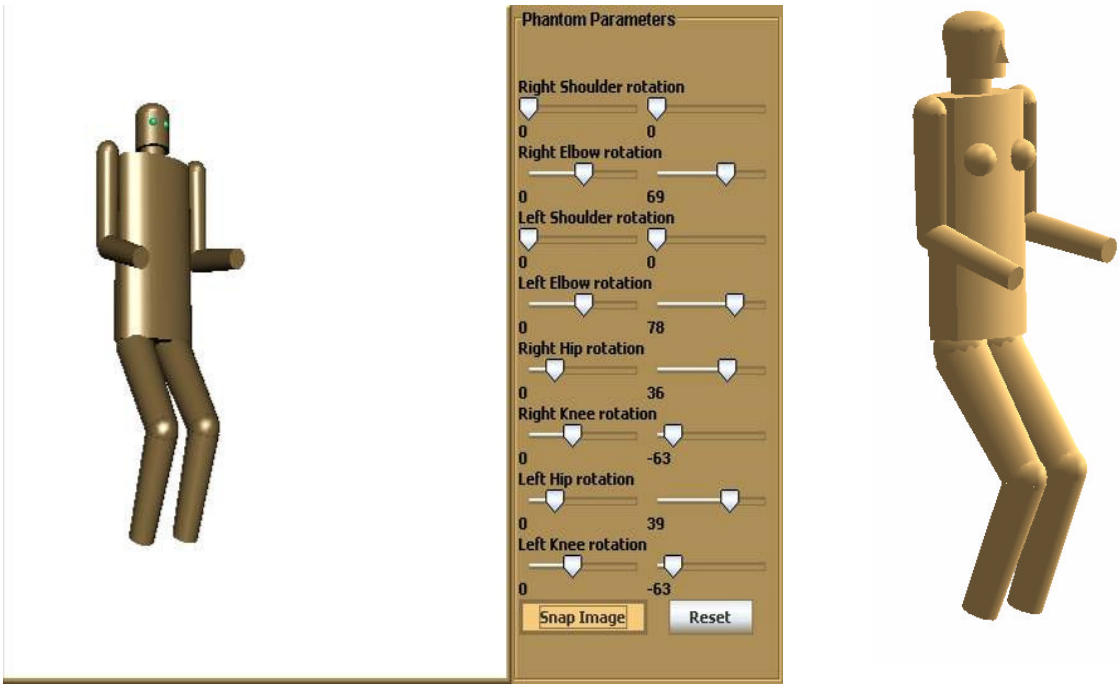

Fig. 66. The image of the phantom generated with the "Snap Image" button of the GUI (left) and the generated figure for this configuration using MORITZ (right).

6.1.3 Generate MCNP Input

The "**Generate MCNP Input**" button displays the generated input file as shown in Fig. 67. The angles for the arms and legs, taken from the slider bar values, are also printed in the input file as shown in Fig. 67. The input file can be saved to a working directory using the "**Save Input**" button. The last directory used to save the input file will be in the memory.

The user can run MCNP using the "**Run MCNP**" button in either the window shown in Fig. 67 or in the main GUI window shown in Fig. 65. However, there is one distinction between the "**Run MCNP**" buttons in these two windows. If the user makes any changes (e.g., source energy) to the generated input file using the input file window shown in Fig. 67 and uses the "**Run MCNP**" button in this window, these changes will be effective while running the code. However, the "**Run MCNP**" button shown in Fig. 65 will discard any changes that are made in the input file window.

While the code is running, the "**Run MCNP**" button will change to "**Stop MCNP**" so the user can terminate the simulation if desired.

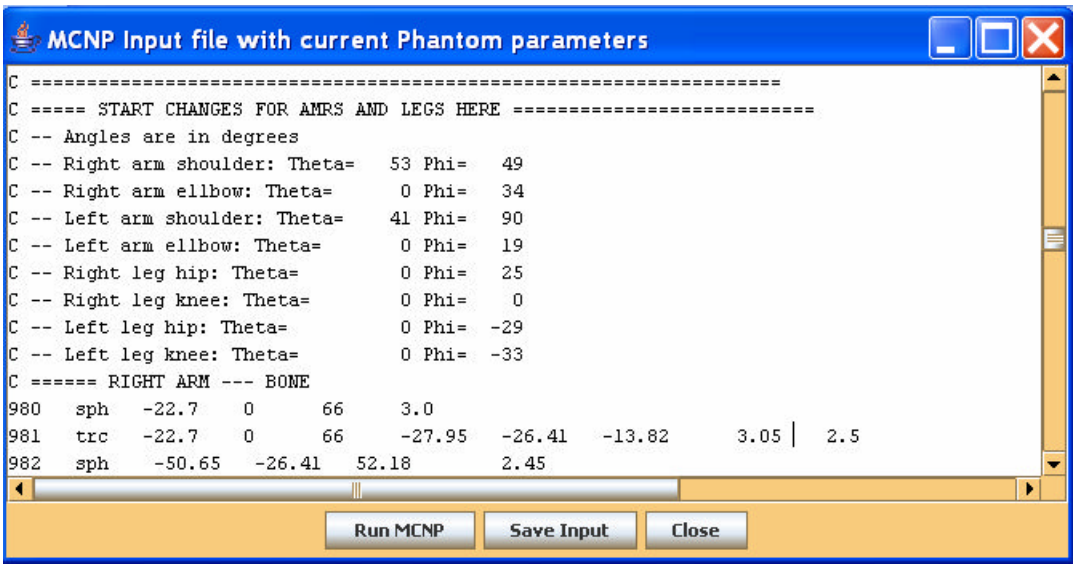

Fig. 67. The MCNP Input file window.

6.1.4 Load Custom Input and Substitute Energy

A default MCNP input file, in which the phantom is within a vacuum, is included in the executable jar file. However, the user can load a custom phantom input file (e.g., phantom model in a room, using different cross-section sets, or a complex source description) using the "**Load Custom Input**" button shown in Fig. 65. Once the custom file is loaded, the arm and leg modifications for the phantom are done using this custom input file. It is important to note that while it is possible to add new cells and surfaces, the phantom specification part should not be changed. More clearly, the phantom model for the custom file structure needs to be similar to the reference input file. For the arms and legs to change, the custom file needs to have the line

C ===== START CHANGES FOR ARMS AND LEGS HERE ==========

for the search and change of the corresponding surface cards. If the custom input file does not contain the above line, an error message stating "*Failed to set custom input file: The file is not a valid PIMAL MCNP input file*" will appear.

Once a custom file is loaded, the name of the file will appear in the window as "**Using Custom file,**" followed with the name of the file as shown in Fig. 68. From this point forward, the "**Load Custom Input**" button will be replaced with "**Reset Input,**" and the user can return to using the default input file at any time using this button.

In addition to the position of the arms and legs, the user can specify the MCNP problem mode (either photon only or as a coupled neutron and photon problem), source energy, and position. At this time, the source specification options using the GUI are very limited—only monoenergetic, point sources can be defined using the interface. If desired, however, the user can disable this feature by leaving the "**Substitute Energy**" box unchecked. For example, if a custom input file is loaded, then the source values included in that input file can be kept by disabling the option of entering source values. When this box is not checked, the source energy and position boxes are disabled (i.e., the user will not be able to enter any value) and these boxes are dimmed, as shown in Fig. 68.

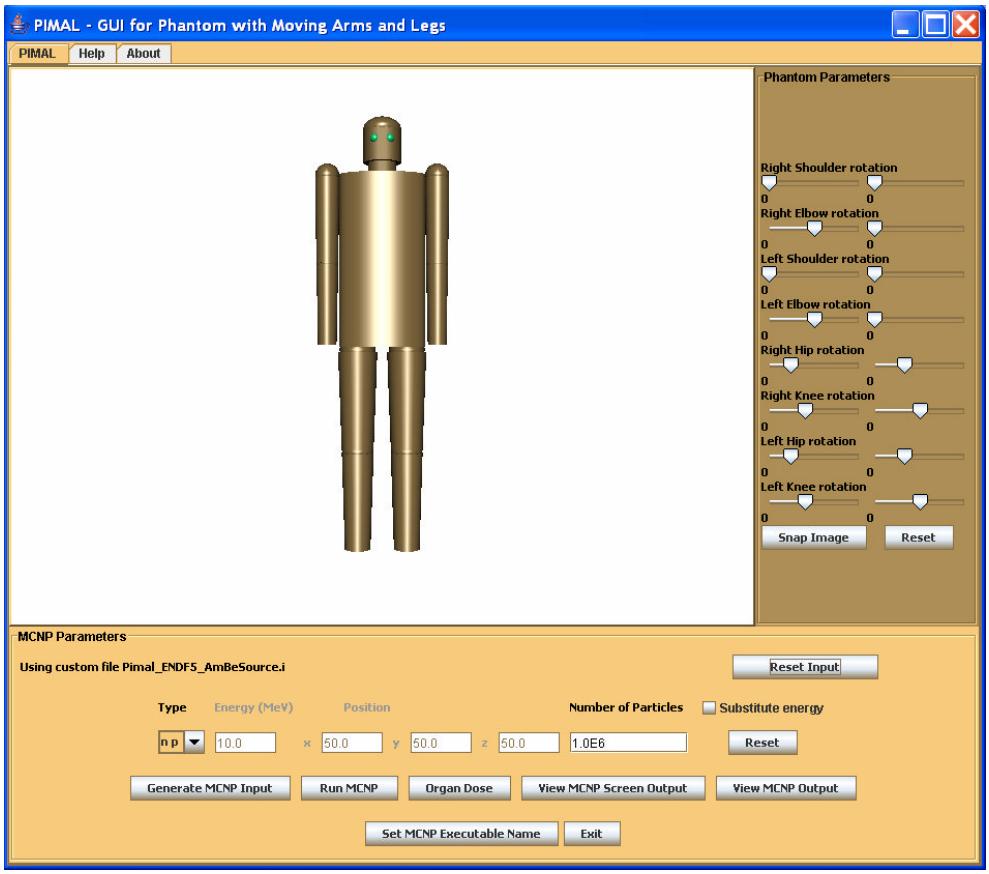

Fig. 68. The layout of the GUI when a custom input file is used. The option for entering source parameters using the GUI will be inactive when the "Substitute Energy" box is not checked.

6.1.5 MCNP Outputs and Executable Name

The user can view the messages generated by MCNP during the simulation using the "**View MCNP Screen Output**" button. If the simulation is terminated due to any "fatal" or "geometry" errors, this error message will be available in this output. Further, the type of the error will be extracted from this output and displayed as a warning message.

Additionally, full MCNP output file can be displayed using the GUI with the "**View MCNP Output**" button. The snapshots of the screen output (left) and full MCNP output (right) are shown in Fig. 69.

The MCNP output files can be saved in ASCII format and the last directory will be saved in the memory.

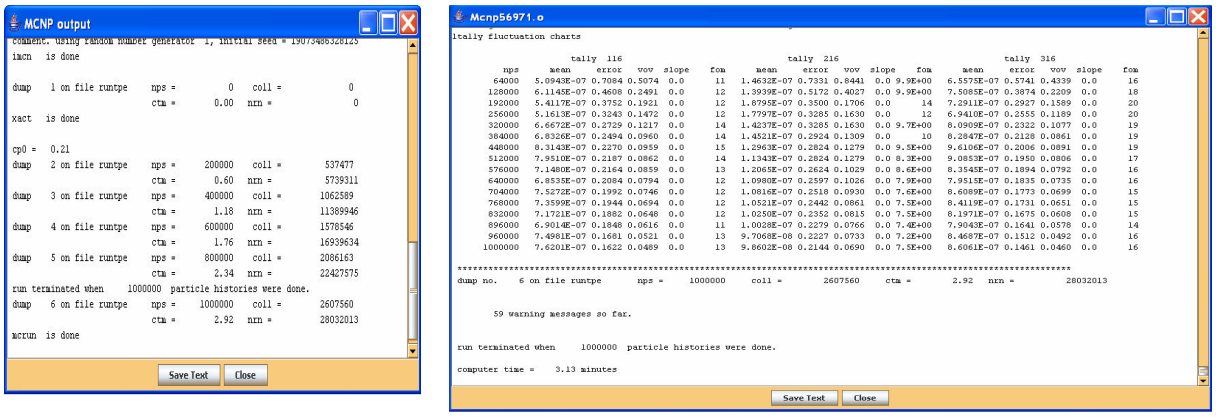

Fig. 69. The "View Screen MCNP Output" and "View MCNP Output" buttons will display the screen messages while running the code (left) and the full MCNP output (right), respectively.

In order to use the GUI, it is assumed that a version of MCNP is installed on the user's computer (i.e., the GUI does not include the MCNP executable) and included in the path. In the GUI, MCNP5 is the default radiation transport code used for the simulations. However, this could easily be changed at any time (i.e., to MCNPX or to past or future versions of the code when released) using the "**Set MCNP Executable Name**" button. The user can type the name of the executable in the dialog box. However, for the change to be effective, the GUI needs to be restarted.

6.1.6 Organ Dose Values

The layout for the tabulation of the organ dose values is illustrated in Fig. 70. For photon mode problems, the dose due to photons is displayed. For coupled neutron and photon calculations, the dose due to neutrons, photons, and total absorbed dose are listed separately. The uncertainties in the computed values are tabulated, as shown in Fig. 70. The number of particles in the simulation is shown in the title. If desired, the organ dose values can be saved in a directory in ASCII format, which may be opened with a text editor such as Microsoft Notepad® and also by Microsoft Excel®. The working directory is again kept in the memory. Further, the user can load multiple output files (i.e., previous simulations) for display, as needed. It is not necessary to run the code using the GUI. The user can create input file(s), run MCNP in a different environment (i.e., parallel Linux clusters), and then process the output file(s) using the GUI.

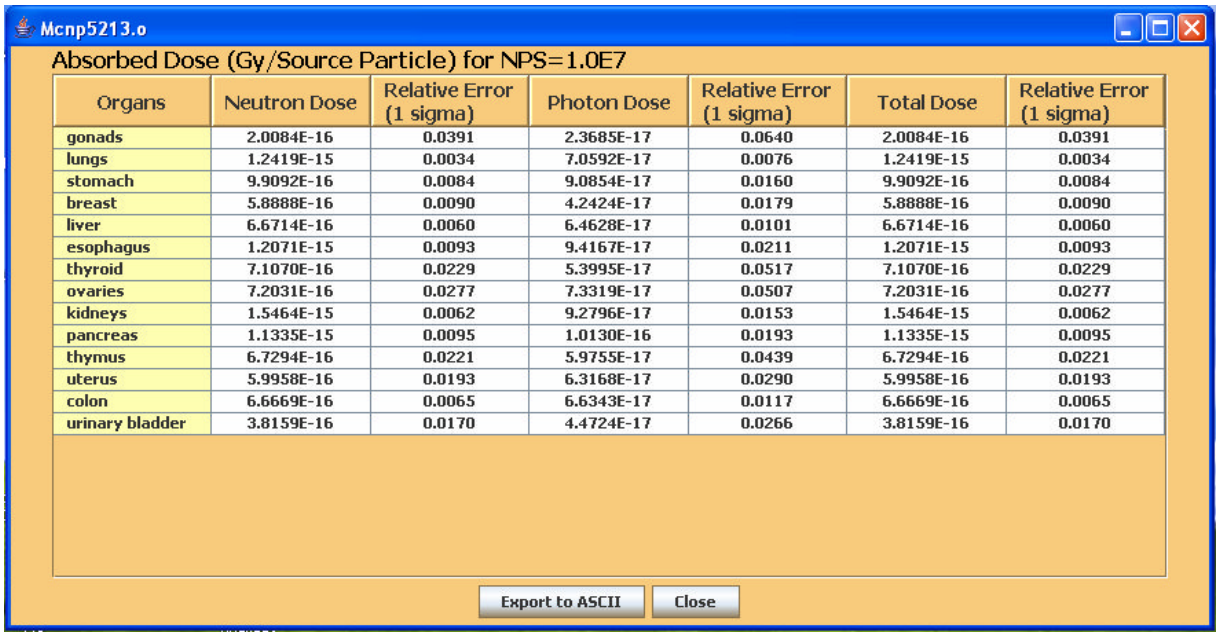

Mcnp5213.o

Absorbed Dose (Gy/Source Particle) for NPS=1.0E7

Organs	Neutron Dose	Relative Error (1 sigma)	Photon Dose	Relative Error (1 sigma)	Total Dose	Relative Error (1 sigma)
gonads	2.0084E-16	0.0391	2.3685E-17	0.0640	2.0084E-16	0.0391
lungs	1.2419E-15	0.0034	7.0592E-17	0.0076	1.2419E-15	0.0034
stomach	9.9092E-16	0.0084	9.0854E-17	0.0160	9.9092E-16	0.0084
breast	5.8888E-16	0.0090	4.2424E-17	0.0179	5.8888E-16	0.0090
liver	6.6714E-16	0.0060	6.4628E-17	0.0101	6.6714E-16	0.0060
esophagus	1.2071E-15	0.0093	9.4167E-17	0.0211	1.2071E-15	0.0093
thyroid	7.1070E-16	0.0229	5.3995E-17	0.0517	7.1070E-16	0.0229
ovaries	7.2031E-16	0.0277	7.3319E-17	0.0507	7.2031E-16	0.0277
kidneys	1.5464E-15	0.0062	9.2796E-17	0.0153	1.5464E-15	0.0062
pancreas	1.1335E-15	0.0095	1.0130E-16	0.0193	1.1335E-15	0.0095
thymus	6.7294E-16	0.0221	5.9755E-17	0.0439	6.7294E-16	0.0221
uterus	5.9958E-16	0.0193	6.3168E-17	0.0290	5.9958E-16	0.0193
colon	6.6669E-16	0.0065	6.6343E-17	0.0117	6.6669E-16	0.0065
urinary bladder	3.8159E-16	0.0170	4.4724E-17	0.0266	3.8159E-16	0.0170

Export to ASCII Close

Fig. 70. The layout of the organ dose display.

Additionally, the user can change the number of organs in the output file by changing the reference input file and load it as a custom input file. While processing the MCNP output file, the GUI searches for the line "**C ENDORGAN**" as a keyword, indicating the completed search for organs and corresponding tallies. The names and the corresponding dose values for any organ before this keyword will be displayed in the organ dose window. In the current structure, tally 116 is dedicated to neutron dose, tally 216 to photon dose, and tally 316 for total dose (neutron plus photon). For photon-only problems (mode p), only the results from tally 216 are displayed. In future versions, other particle types (e.g., electrons) can be included. If the user wants to change the tally type (i.e., from F6 to F4 or F8), then the user can make the necessary changes in the corresponding java files by changing the search criteria and recompiling the code. In future versions, tally options could be made more flexible using a preference dialog box.

Further, in future versions of the GUI, the source description (model) could be improved significantly to describe internal and external sources with more options (e.g., select the internal organ as source or describe external source as a parallel beam in which the user can specify the source-to-phantom distance, beam height, and energy, etc.) in a pull-down menu. Additionally, in the current version, only absorbed dose values are tabulated. In future versions, equivalent dose values could be computed and displayed.

7. SUMMARY AND FUTURE WORK

The objectives of this work were to: (1) update the MIRD-5 mathematical phantom model that is currently used by the NRC staff to improve the assessment of dose for realistic exposure configurations, (2) perform benchmark computations against ICRP-74 values and investigate the reasons behind the discrepancies, if any, and (3) develop an interface to assist the user (or analyst) in using the updated phantom model in dose assessment activities thus reducing staff time.

The phantom model currently used by the NRC staff is based on the MIRD-5 phantom model, which was published in 1974. Therefore, it does not include any of the updates within the past three decades (i.e., those of Ref. 3). More importantly, a number of important organs (i.e., neck, esophagus) are not included, and the location of some of the organs was inappropriate (e.g., thyroid). A review of updates in the mathematical phantom models was performed, and a recently revised phantom model from the UF, in conjunction with ORNL, was obtained as the starting point for this work. This revised phantom model, referred to as the ORNL-UF phantom model, includes updated internal organs and elemental compositions.

First, a series of Monte Carlo computations, using MCNP5, was performed for the standard ICRP irradiation geometries and energies using the ORNL-UF phantom model. The computational results were benchmarked against the tabulated values in ICRP-74. For photon sources, the agreement between the computed values and the tabulated data in ICRP-74 was in general within ±10 percent for all major organs except the thyroid. For neutron sources, the agreement between the ICRP-74 values and the ORNL-UF model was within ±20 percent for all major organs except for the thyroid and colon. The reasons behind the discrepancies were investigated. Further analysis showed that the discrepancies are partially because the data tabulated in ICRP-74 are based on the compiled results of previously published studies, in which different phantom models, nuclear codes, and cross-section sets are used. Therefore, there was a wide spread in the original data for some of the organs, and a few examples that were taken from the ICRP-74 report are included in this report.

In order to determine the impact of the changes on the computed organ values, a series of computations was performed for the MIRD-5 phantom model using the same code, nuclear data, and computers. The computational results were benchmarked against the results obtained using the ORNL-UF phantom model. There was a significant difference, especially for the thyroid, between the computed dose using the ORNL-UF and MIRD-5 phantom models. The main reason for this discrepancy was due to the location of the thyroid (because of lack of neck) in the MIRD-5 phantom model.

To improve the understanding behind the discrepancies and to determine the impact of certain parameters—composition and cross-section data—on the computed organ doses, further calculations were performed. This time, the same phantom model, the ORNL-UF model, was used to perform the computations. The sensitivity to composition was investigated by performing the computations using the traditional three compositions (soft tissue, bone, and lung) instead of the 23 compositions in the ORNL-UF model. The photon source results showed small sensitivity to composition change (2-10 percent) for energies less than 0.2 MeV. Above this energy, there was no sensitivity at all. The neutron source results showed no sensitivity at all for the total dose, except for breast and skin. The dose due to neutrons was affected; however, when the total dose due to both neutrons and photons is considered, there was no effect.

Sensitivity to cross-section data for neutron source computations were performed using ENDF/B-V and ENDF/B-VI.0. The initial benchmark computations were performed using ENDF/B-VI.6. Therefore, the computed organ dose values using three different sets of the cross-section were benchmarked. The computational results showed that there is no difference in the computed organ dose values using the

ENDF/B-VI.0 an ENDF/B-VI.6. However, there is up to a 20 percent change in the computed organ dose values when ENDF/B-V is used.

In summary, the reasons behind the discrepancies between the tabulated ICRP-74 data and the ORNL-UF model are: (1) the differences in the phantom models, hence the change in organ locations (i.e., thyroid with the presence of neck), and (2) the differences in the nuclear data sets. The computational results were benchmarked against the ICRP-74 values since the coefficients reported in this publication are considered "standard." However, the analyses in this work showed the need for updated benchmarks and perhaps even some measurement data.

Traditionally, the phantom models have been in the vertical-upright position, which is not always the case for occupational exposure to radiation. Therefore, the ORNL-UF computational phantom has been revised to add moving capabilities for the arms and legs. The revised phantom is called PIMAL—**P**hantom w**I**th **M**oving **A**rms and **L**egs. In this phantom model, the arms have the capability of bending at the shoulder and elbow and the legs have the capability of bending at the hip and knee. A series of benchmark calculations using PIMAL has been performed to ensure that the revisions did not cause any statistically significant change in the computed organ dose values. There is very good agreement between the computed organ dose values using the ORNL-UF phantom model and phantom with moving arms and legs for the same vertical-upright position.

In order to reduce the user's time in the assessment of organ doses, a GUI has been developed. The user can visualize the arm and leg movement and bring the phantom's arms and legs to the desired posture using the slider bars. Furthermore, the user can use the GUI to generate the input file for this position, perform computations, and extract the organ dose values from the computed output.

Therefore, the result of this work is a detailed mathematical phantom model with freely moving arms and legs that could be used for the assessment of the organ doses for realistic exposure configurations and an accompanying GUI to facilitate phantom postures and dose assessment analyses.

The GUI could be further improved by adding more source capabilities; currently, the user can only define a monoenergetic point source. However, even with the current version, the user can load a custom file in which the source definition is complex and the default values in the GUI will be bypassed. Additional tallies could be added to compute the equivalent dose values, and the GUI can be modified to extract and display these values as well.

Recommendations for future development work can be summarized as:

- **Reshaping the upper trunk and rib cage:** To provide a more realistic exterior shape and to fully resolve the issue regarding the thyroid coefficients for the PA/AP irradiation.

- **Development of male and female models**: The current phantom is hermaphrodite (has gender-specific organs for both genders). In order to improve the radiation dose assessment, separate male and female models can be developed. The male model can be developed by simply removing the female organs from the hermaphrodite phantom; however, the female model would require revisions for the adjustment of height and weight. The standard ICRP source geometries do not clearly show the need for separate male and female models; however, for realistic conditions in occupational exposure, these separate models are necessary. The models can be revised to add the capability of moving arms and legs. This model can be included in the GUI in a pull-down menu.

- **Scaling for weight:** Not all the individuals are within the "reference man" description. The capability of adding extra weight around the torso could be added. Unlike the previous work on this subject, the extra weight can be introduced in an unsymmetrical way. For the torso, different parts can have different scaling factors. The GUI can be modified to visualize these extra weight changes for different parts of the body.

- **Age-dependent models:** The ORNL age-dependent (0, 1, 5, 10, 15 years old) models can be revised and added to the GUI. Clearly, for newborns and 1-year-olds, adding moving capabilities for the arms and legs is not necessary; however, for the other models, this can be done and the models can be included in the GUI in a pull-down menu.

- **Pregnant female model:** The pregnant female model can be updated and revised to add moving capabilities, and the model could be included in the GUI.

- **Voxel phantom model:** ICRP's voxel models can be implemented in MCNP and included in the GUI for the analysis when details of the organs are needed. The voxel phantom model could also be used for benchmark purposes. Moving capabilities for the arms and legs will not be added to these voxel models.

- **Hybrid phantom model:** The head and torso regions, which are simplified and approximated in mathematical phantom models, contain the details of radiological concern. However, the arms and legs are relatively simple in shape and can easily be approximated using mathematical equations. The arm and leg shape can be revised to provide even greater realism. A hybrid phantom consisting of the voxel representation of the head and torso plus a mathematical representation of the arms and legs is suggested. The combination of the mathematical and voxel definitions of the body will not only reduce the computational time and memory requirements in the Monte Carlo calculations but also include the capability of moving arms and legs. This model can be developed and included in the GUI.

A package that includes male, female, and age-specific models with scaling capability could be developed. These models can be included in the GUI, in a pull-down menu, such that all the cases could be analyzed easily whenever there is need. The analysts' time can be reduced substantially, while the resources will be increased significantly for the assessment of dose for any case.

8. REFERENCES

1. W. S. Snyder, M. R. Ford, and G. G. Warner, "Estimates of Specific Absorbed Fractions for Monoenergetic Photon Sources Uniformly Distributed in Various Organs of a Heterogeneous Phantom," *Society of Nuclear Medicine; Medical Internal Radiation Dose Committee Pamphlet,* No. 5, Revised, New York, NY, 1978.

2. International Commission on Radiological Protection, "Report of the Task Group on Reference Man," ICRP Publication 23, *Annals of the ICRP*, 1975.

3. M. Cristy and K. F. Eckerman, *Specific Absorbed Fractions of Energy at Various Ages from Internal Photon Sources. I. Methods*, ORNL/TM-8381/VI, Oak Ridge National Laboratory, Oak Ridge, Tenn. (1987).

4. R. Kramer, M. Zankl, G. Williams, and G. Drexler, "The Calculation of Dose from External Photon Exposures Using Reference Human Phantoms and Monte Carlo Calculations. Part I: The male (ADAM) and female (EVA) adult mathematical phantoms," Neuherberg, Germany: GSF-National Research Center for Environment and Health; GSF-Bericht S-885, 1982.

5. K. V. Riper, "BodyBuilder," 2005.

6. E. Han, "Revised Series of Stylized Anthropometric Phantoms for Internal and External Radiation Dose Assessment," Ph.D. Dissertation, University of Florida, 2005.

7. E. Han, W. E. Bolch, and K. F. Eckerman, "Revisions to the ORNL Series of Adult and Pediatric Computational Phantoms for Use with the MIRD Schema," *Health Physics* **90(4)**, 337–356, 2006.

8. International Commission on Radiological Protection, "Basic Anatomical and Physiological Data for use in Radiological Protection: Reference Values," ICRP Publication 89, *Annals of the ICRP*, 2002.

9. International Commission on Radiological Protection, "Conversion Coefficients for Use in Radiological Protection Against External Radiation," ICRP Publication 74, Oxford, UK:Pergamon Press, 1996.

10. D. C. Kaul, S. D. Egbert, M. D. Otis, T. Kuhn, G. D. Kerr, K. F. Eckerman, M. Cristy, T. Maruyama, J. C. Ryman, and J. S. Tang, *Organ Dosimetry, in Reassessment of Atomic Bomb Radiation Dosimetry*, Ed., W.C. Roesch (Hiroshima, Radiation Effects Research Foundation), 1987.

11. R. H. Olsher and K. A. Van Riper, "Application of a Sitting MIRD Phantom for Effective Dose Calculations," *Radiation Protection and Dosimetry* **116**, 392–395, 2005.

12. F. Takahashi, A. Eendo, and Y. Yamaguchi, "Dose Assessment from Activated Sodium within a Body in Critical Accidents," *Radiation Protection and Dosimetry* **106**(3), 197–206, 2003.

13. International Commission on Radiation Units and Measurements, "Conversion Coefficients for Use in Radiological Protection Against External Radiation," ICRU Report 57, Bethesda, MD, ICRU Publications, 1998.

14. X-5 Monte Carlo Team, *MCNP—A General Monte Carlo N-Particle Transport Code, Version 5*, LA-UR-03-1987, 2003.

15. K. F. Eckerman and A. L. Sjoreen, *Radiological Toolbox User's Manual*, ORNL/TM-2004/27, Oak Ridge National Laboratory, Oak Ridge, Tenn. (2004).

16. A. V. Ulanovsky and K. F. Eckerman, "Modifications to the ORNL Phantom Series in Simulation of the Responses of Thyroid Detectors," *Radiation Protection and Dosimetry* **79**, 429–431, 1998.

17. H. Akkurt, K. F. Eckerman, J. C. Wagner, and S. Sherbini, "PIMAL: Phantom with Moving Arms and Legs," submitted to *Trans. Amer. Nucl. Soc*., June 2007.

18. H. Akkurt, K. F. Eckerman, D. Wiarda, J. C. Wagner, and S. Sherbini, "Development of a Computational Phantom with Moving Arms and Legs for Radiation Dose Assessment," submitted for presentation at the Health Physics Society Conference, July 2007.

19. H. Akkurt, D. Wiarda, A. Fleckenstein, and K. F. Eckerman, "A GUI for Computational Phantom with Moving Arms and Legs," submitted to *Trans. Amer. Nucl. Soc*., June 2007.

20. Sun Developer Network, http://java.sun.com.

21. A. E. Walsh and D. Gehringer, "Java3d, API Jump Start," http://web3dbooks.com/java3d/ jumpstart/Java3DExplorer.html.

22. A. Davison, *Killer Game Programming in Java*, O'Reilly, May 2005.

23. R. A. Schwarz, "MCNP Visual Editor," 2005.

24. K. V. Riper, "Moritz," 2005.

INTERNAL DISTRIBUTION

1–3. H. Akkurt
4–6. K. F. Eckerman
7. D. Ilas
8. J. O. Johnson
9. B. L. Kirk
10. R. W. Leggett
11. C. V. Parks
12. J. E. Rushton
13. J. J. Simpson
14. J. C. Wagner
15. D. Wiarda
16. ORNL Office of Technical Information and Classification

EXTERNAL DISTRIBUTION

17. Wesley Bolch, University of Florida, 202 Nuclear Science Bldg., P.O. Box 118300, Gainesville, FL 32611-8300
18. Michael Boyd, Office of Radiation and Indoor Air, U.S. Environmental Protection Agency Headquarters, Ariel Rios Building, 1200 Pennsylvania Avenue, N.W., Mail Code 6608J, Washington, DC 20460
19. Stephanie P. Bush-Goddard, U.S. Nuclear Regulatory Commission, Mail Stop TWFN 9 C24, 11545 Rockville Pike, Rockville, MD 20852-2738
20. Anthony M. Huffert, U.S. Nuclear Regulatory Commission, Mail Stop TWFN 9 C34, 11545 Rockville Pike, Rockville, MD 20852-2738

21–41. Harriet Karagiannis, U.S. Nuclear Regulatory Commission, Mail Stop TWFN 9 C34, 11545 Rockville Pike, Rockville, MD 20852-2738

42. Doris E. Lewis, U.S. Nuclear Regulatory Commission, Mail Stop TWFN 9 C34, 11545 Rockville Pike, Rockville, MD 20852-2738
43. Charles W. Miller, Centers for Disease Control, 1600 Clifton Road, N.E., Atlanta, GA 30333
44. Sami S. Sherbini, U.S. Nuclear Regulatory Commission, Mail Stop TWFN 8 F5, 11545 Rockville Pike, Rockville, MD 20852-2738
45. Steven L. Simon, National Cancer Institute, Executive Plaza South, Room 7100, Bethesda, MD 20892-8322
46. George Xu, Dept. of Mechanical, Aerospace, and Nuclear Engineering, Room 1-11, NES Bldg., Tibbits Ave., Rensselaer Polytechnic Institute, Troy, NY 12180